Author:
Salgado-Ayala, Rodrigo

Title:
Studies of flow and scalar distribution in two large industrial environments.

STUDIES OF FLOW AND SCALAR DISTRIBUTION IN TWO LARGE INDUSTRIAL ENVIRONMENTS

Rodrigo Salgado Ayala

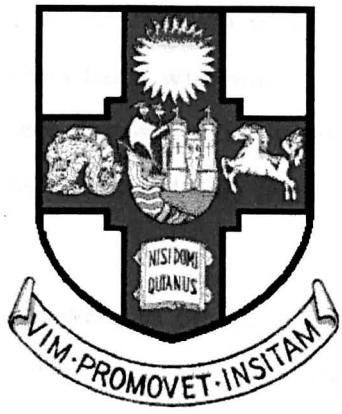

A dissertation submitted to the University of Bristol in accordance with the requirements of the degree of Doctor in Philosophy in the Faculty of Engineering.

Department of Mechanical Engineering.

February 2000

Word Count: 28,179

Abstract

The systems and geometries considered in this work are large-scale enclosures consisting of ventilated workspaces with turbulent behaviour. Two different industrial environments are studied: an aircraft hangar and a large food repository.

The experimental programme for the aircraft hangar was undertaken to estimate the boundary conditions and to aid validation of Computational Fluid Dynamics (CFD) predictions.

The experimental data and the CFD predictions suggest that there is an unstable stratification layer at about 6-8m from the floor of the 35m high hangar. Using recirculation fans would help to destroy this stratification inversion and result in 'better' and more comfortable temperature distribution within the hangar. Also, experimental work was undertaken in a small box filled with water, where stable thermal stratification and a downward pointing jet were imposed. CFD work is reported and the predictions of the code are compared against measured data from a typical environment in a large building and the laboratory.

The aims for the food storeroom were to obtain a better understanding of how flow distributions affect moisture absorption and to identify better possible ways of improving airflow distribution within the room.

Information about the moisture absorption in the room was obtained by undertaking experiments with silica gel placed at various locations within the room. Laboratory experiments were undertaken on the food material to characterise its water vapour absorption properties. Some experimental measurements were also taken within the room of water absorption by the product after having been in the room for finite lengths of time.

Based on the silica gel and the food material characterisation work, a predictive model was constructed within a CFD framework. The predictive model computes flow distributions within the room and moisture absorption of the food material.

Acknowledgements

In the first place I would like to express my deep gratitude to Professor G.L. (Joe) Quarini for his valuable teaching and its generous and constant support thought the development of the present work.

Grateful acknowledgement is made to the National Council of Science and Technology (CONACyT) of México for its economic support, and to the British Council for the award of a studentship during the first year of this work.

I would also like to thank the partners of the industrial projects on which part of this work is based. In particular to Alec Lecat, Barry Richmond (Nestlé-York) and Gary Crisp (British Aerospace), for sharing with me their practical and technical knowledge. Many thank to Mike Darby, his help was invaluable to build my experimental rig.

Finally, I have to thank my friends, family and colleagues for their support during all the development of this work.

Declaration

The accompanying dissertation entitled "Studies of flow and scalar distribution in two large industrial environments" is submitted in support of an application for the degree of Doctor of Philosophy in Engineering at the University of Bristol.

The dissertation is based on independent work by the candidate, except where clearly referenced.

No portion of the work referred to in this dissertation has been submitted in support of an application for another degree or qualification in this, or any other university or other institute of learning.

The views and opinions expressed in this thesis are solely those of the author and not the University of Bristol.

I declare that the above statements are true,

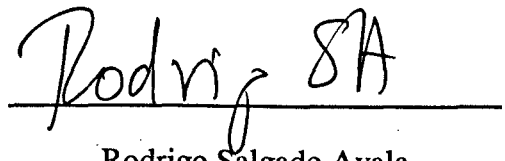

Rodrigo Salgado Ayala

February 2000.

Contents

List of figures

List of tables

Nomenclature

A	Area, m^2
a	Coefficient in numerical method
a_3	Coefficient of skewness
a_4	Coefficient of kurtosis
b	Velocity scale in entrainment model, dimensionless
B_o	Buoyancy flux, $m^4 s^{-3}$
b_T	Temperature scale in entrainment model, dimensionless
C	Constant, dimensionless
C	Concentration, kg m^{-3}
C_B	Experimental moisture absorption, kg m^{-3}
Cf	Correction factor, dimensionless
CoV	Coefficient of variation, dimensionless
c_p	Specific heat at constant pressure, J kg^{-1} K^{-1}
d	Diameter, m
D	Diffusivity, $m^2 s^{-1}$
D_h	Hydraulic diameter, m
D_{ij}	Rate of strain, s^{-1}
f	Friction factor, dimensionless
Fr	Froude number, dimensionless
g	Acceleration due to gravity field of the earth, $9.8ms^{-2}$
G	Rate of production or destruction of turbulence by bouyancy, kg m^{-1} s^{-3}
$\overline{h}_m$	Average mass transfer coefficient, m s^{-1}
H	Height, m
IOVP	Index of ventilation performance, dimensionless
k	Turbulent kinetic energy, $m^2 s^{-2}$
k	Mass transfer coefficient, m s^{-1}
K	Permeability, m^2
M_o	Momentum flux, $m^4 s^{-2}$
Ms	Momentum source, N m^{-3}
N	Buoyancy frequency, s^{-1}
$O[\,]$	Order
p	Pressure, Pa
P	Rate of production of turbulence, kg m^{-1} s^{-3}
Pe	Peclet number, dimensionless
Pr	Prandtl number, dimensionless
Q_o	Volume flux, $m^3 s^{-1}$
r	Radius, m

R	Flow resistance, kg m^3 s^{-1}
Re	Reynolds number, dimensionless
Ri	Richardson number, dimensionless
S	Dimensionless temperature gradient
S	Source or sink term
s	Standard deviation
Sc	Schmidt number, dimensionless
T	Temperature, °C
t	Time, s
t_a	Fluid age, s
T_i	Turbulence intensity, dimensionless
t_m	Mean fluid age, s
t_o	Turn over time, s
u, v, w	Velocity component in the x, y and z direction, m/s
U_0	Source velocity, m/s
V	Volume, m^3
V'	Void volume, m^3
$\dot{V}$	Volumetric flow rate, m^3 s^{-1}
W_c	Moisture uptake, kg
W_o	Mean velocity at inlet, m s^{-1}
$\bar{x}$	Mean
x, y, z	Cartesian coordinates, m
Zpi	Penetration distance, m

Greek letters

β	Volumetric expansion coefficient, K^{-1}
Δ	Increment
α	Entrainment constant, dimensionless
λ	Constant that relates length scales, dimensionless
λ	Thermal conductivity, J (s m K)$^{-1}$
ε	Turbulence dissipation, m^2 s^{-3}
ρ	Density, kg m^{-3}
σ_{ij}	Stress tensor, kg m^{-1} s^{-2}
μ	Viscosity, kg m^{-1} s^{-1}
δ_{ij}	Kroeneker delta
ϕ	Generic scalar
Γ	Diffusion coefficient, m^2 s^{-1}
σ_T	Turbulent Prandtl number, dimensionless

κ	von Karman constant, 0.41 dimensionless
θ	Relative stratification, dimensionless
γ	Volume porosity, dimensionless
κ	Scale factor

Subscripts

c	Centre
.	Ambient, saturation
$0, o$	Value at the inlet or source
h	Heat
T	Turbulent
j	Jet
r	Room
c	Cabinet
w	Wetted surface
a	Air side
B	Bed
T	Top
B	Bottom

1 INTRODUCTION

1.1 Scope of the work

Controlling temperature, humidity and airflow patterns efficiently is an important task in a number of engineering disciplines. These include the building, electronic and food industries. In the building industry for example, it is desirable to design a ventilation system capable of reducing energy consumption, minimising the level of airborne pollutants within a building, and providing comfort to the people inside it. On the other hand, in the food industry, ventilation is important in order to obtain products with high, uniform quality in reduced times and in a hygienic environment.

At the beginning of the decade air movement in a space was predicted from either air jet diffusion data or testing a physical model of the whole enclosure, or both. However, Awbi and Gan (1991) has pointed out that physical modelling scale effects can be very significant, particularly when dealing with buoyant flows.

Computational Fluid Dynamics (CFD) is becoming a vital component in the design of industrial products and processes. CFD has several advantages over experimental-based approaches to fluid system design as mentioned by Versteeg and Malalasekera (1995):

- Substantial reduction of lead times and cost of new designs.
- Ability to study systems where controlled experiments are difficult or impossible to perform (e.g. very large systems).
- Ability to study systems under hazardous conditions at and beyond their normal performance limits.
- Practically unlimited level of detail results.

Originally, due to the lack of powerful and affordable computers, airflow simulation was limited to laminar, one- or two-dimensional, steady, and isothermal situations in simple geometries. Now, airflow simulations include turbulent, three-dimensional, transient, and buoyancy-affected flows in complex geometries of practical application.

Bergstrom (1994) has pointed out that the prediction of airflows in working environments is a complex and difficult tasks. Generally these flows are turbulent, yet they also include regions of little or no turbulence where molecular transport is important. In the context of controlling the room environment, these flows are buoyant; in some cases, buoyancy drives the mean flow motion. The presence of walls creates so-called 'near wall regions', where the turbulent transport is significantly influenced by the solid surface. In practical applications, the obstructions within the room create geometrical complexity. Finally, most airflows are inherently three-dimensional and often unsteady. Given these characteristics, airflows in rooms represent a significant challenge for present numerical codes and turbulence models.

The convective heat transfer area has traditionally been divided into two regimes: forced and free convection. Forced convection is usually caused by circulation of fluid by external agents such as a fan, blower or pump. Free convection arises simply because of a density variation, caused by heat or mass transfer processes, in a body force field, such as that generated by gravitational acceleration.

In ventilation problems, free and forced regimes are usually combined. Very often the convection process can be considered as a predominant forced flow circumstance or as a predominant natural convection one. The Richardson number, Ri, is used as criterion for transition from natural convection to forced convection (Bejan, 1984). However, studying mixed convection in practical systems is difficult. These difficulties arise from the fact that there are numerous variables which can affect the thermalhydraulic performance of the system, including specific geometry, forced or imposed flow rates, driving temperature differences, and heat and mass sources or sinks or both.

The ventilation of large enclosures can give rise to thermal stratification. This situation is common in nature, where the heat input into the atmosphere from various heat sources results in buoyant flows. These flows tend to redistribute air so that the least dense and warmest fluid lies above the denser, colder fluid. Thermal stratification can be advantageous in certain situations, such as solar ponds and chilled water tanks, but troublesome in others such as in most air conditioning tasks.

Natural convection and buoyancy induced flow abound in nature and in our living environment. In the past 20 years CFD in natural convection has made considerable progress. However, there is an inherent resolution of length scale problem that makes it

very difficult to correctly represent all the important flow structures. The smallest scale is that associated with the smallest eddy which can survive before it is destroyed by dissipative viscous action and its mechanical energy converted to heat. This small scale may be a few millimetres or smaller. The physical dimensions of the system set the largest scale, which could be many meters. The mesh now needs to be small enough to resolve the smallest eddies, and yet cover the complete flow field. This immediately implies it needs to have $O[10^3]$ points in each direction, giving a total mesh point size of approximately 10^9. At each mesh point we need to solve and store each of the flow vectors (u, v, w), the pressure, p, the temperature, T, and any other scalar such as humidity or fluid age. Further, the fluid is inherently time dependent, if it is turbulent. This makes it impossible to undertake a full turbulent flow simulation. What is possible is to 'smear' the fine scales by averaging the flow and thus removing the need to resolve the very fine scales. However, to do this, a turbulent model is required which allows the effects of the small scales to be represented within the coarse model. Turbulence modelling is inherently very difficult, and not the major topic of this work. What is important to note is that many of the sophisticated turbulence models and associated boundary conditions were developed for isothermal forced convection. Buoyancy has not been extensively studied in the literature.

The systems and geometries considered in this work are large-scale enclosures consisting of ventilated workspaces with turbulent behaviour. We study two different industrial environments:

- An aircraft hangar where the effect thermal stratification affects the distribution of velocity and temperature.
- A large food repository where the presence of a porous moisture absorbent material affects the distribution velocity and moisture.

In the first case, experimental work is undertaken in a small box filled with water, where stable thermal stratification and a downward pointing jet are imposed. CFD work is reported and the predictions of the code are compared against measured data from a typical environment in a large building and the laboratory.

In the second case, experimental work is carried out to characterise the food properties. Also, measurements in the food repository are reported. Finally, a CFD model is constructed and the results compared with the experimental data available.

The link between these industrial cases is the complexity of the flow in large spaces affected by stratification or porosity. In both cases we are interested in the distribution of scalars: temperature, moisture or fluid age.

The aim of this work is to obtain simple models to predict the distribution of scalars in large industrial spaces affected by imposed resistances, e.g. stratification or porosity.

1.2 Objectives

The present work studies the thermalhydraulic characteristics and ventilation performances of environments typical in the building industry. In this study experimental and CFD work is used. The experimental work has been undertaken in a large building and in the laboratory. A commercial code (CFX 4.2) and simple modifications to the equations used for the code are used to predict the flow, temperature and moisture distribution within the space. The aims of the present work are:

1. To obtain high quality experimental data of temperature and moisture distributions in typical, full size, large scale industrial geometries.
2. To study in the laboratory the effects of Reynolds and Richardson number on the maximum penetration of a buoyant non swirling jet discharged downward in a thermal stratified environment.
3. To develop simple models for stratification problems.
4. To develop simple modifications to a CFD commercial code to predict moisture distribution in a large environment.
5. To undertake CFD calculations to predict the thermalhydraulic performance of large scale industrial geometries.
6. To compare the CFD predictions with the experimental data, and thereby establish the degree of confidence which can be placed in this mathematical tool for modelling large scale geometries affected by an imposed resistance.

1.3 Structure of the thesis

Immediately after this introduction, a survey of relevant literature on ventilation with special reference to stratified environments and buoyant jets is carried out in Chapter 2.

Chapter 3 provides the theoretical basis for our investigation. The equations and boundary conditions that govern the turbulent three-dimensional convective flow will be presented in this chapter. Some approximations and their restrictions are discussed. Related to these approximations are the characteristic velocity and length scales for the different dimensionless numbers used in the experimental work.

Chapter 4 presents a description of the experimental work accomplished and the methods employed. The experimental set-ups with their optical components and data acquisitions systems as well as the adopted measurement procedures are discussed. An assessment of the accuracy of the experimental methods is also given.

The experimental results are presented in Chapter 5. The experiments are used almost without exception for validation of the numerical code. Therefore, in the same chapter, the experimental data is compared with the corresponding three-dimensional numerical results. Comparisons are also made with available experimental data of other investigators.

A brief description of the numerical method that is used by the code to solve the governing equations is given in Chapter 6. Also, the modifications done to the code are explained.

Chapter 7 is devoted to explaining the results of the numerical simulations.

Finally, in Chapter 8 an evaluation of the numerical and experimental work as presented in this thesis will be given and the most important conclusions of the investigation summarised.

2 LITERATURE SURVEY

2.1 Introduction

The object of this chapter is to review the literature relevant to the subject of the present work. The literature is presented in three main sections:

- Experimental work on round buoyant jets.
- Numerical simulation of buoyancy affected flows.
- Numerical simulation of moisture migration in porous spaces.

2.2 Experimental work on buoyant jets

Transport processes in fluids in which the motion is driven simply by the interaction of density differences with the gravity field are common in a wide range of areas including geothermal fields, nuclear waste deposits, chilled-water storage, solar thermal systems, fires in enclosures and atmospheric and oceanic circulation. Furthermore, a common situation in industry is the discharge of heat and material in the ambient air or water through jet flows, which are buoyant due to the temperature or concentration difference between the discharge and the ambient medium, which could be stratified or not.

Stable stratification occurs when the density of the medium decreases with height. However, in many buoyancy induced flows, conditions are often appropriate for the body of the fluid to become unstable to disturbances. When this happen internal waves are generated. Two kinds of instability commonly arise. Thermal instability in a stratified medium results when a denser fluid is introduced above a less dense fluid. Hydrodynamic instability arises in a laminar flow when a balance of buoyancy, pressure, and viscous forces may contribute net energy to a disturbance, causing it to grow as it is convected along (Gebhart, 1973).

Following Turner (1973), models that describes fluid motion in which buoyancy forces play the major role because they are the source of energy for the mean motion itself are classified as 'plumes' and 'thermals'. The former definition is used when buoyancy

remains confined to a limited volume of fluid, which, as it rises, loses its connection with the source, which produce it. Plumes arise when buoyancy is supplied steadily and the environment remains cooler than the plume. When plumes are generated by buoyancy and an extra initial momentum source the plume is termed a buoyant jet. However, when the environment is stratified the jet reaches a terminal height of rise. List (1982) explains that the latter is a direct result of the fact that dense fluid entrained in the lower regions of a buoyant jet, when carried to a less dense environment, will ultimately give rise to a negative buoyancy flux that destroys the upward momentum. The momentum of the jet may in fact, carry dense fluid beyond a level of neutral stability so fallback occurs. A downward negatively buoyant jet is sketched in Figure 2.1. The flow is of a mixed-convection type resulting from the interaction between the buoyancy force and the externally induced momentum input.

Interested in the dynamical behaviour of the tops of cumulus clouds, Turner (1966) investigated the motion of turbulent jets of heavy salt solution injected upwards into a tank of fresh water and compared them with that of initially buoyant plumes. Turner released fluid from a tank and carried out the experiment until the bottom of the tank was filled with a mixture of salt and fresh water, see Figure 2.2. Turner demonstrated that there is an essential difference between the behaviour of jets and plumes. Jets affected by buoyancy reach a steady height and fluctuate randomly and with small amplitude about this height. Plumes are found to have a regular oscillatory behaviour, with large amplitude fluctuations of the height at the top of it. Turner developed equations to obtain the mean penetration distance, Z_{pi}, by considering a fully developed turbulent velocity profile with a uniform velocity across the cylindrical outlet and based on dimensional analysis found that:

$$Z_{pi} = C\pi^{1/4} r_0 \mathrm{Fr}^{1/2} = 2.46 r_0 \mathrm{Fr}^{1/2}, \qquad 2.1$$

where the experimental value of the constant C for jets is 1.85; r_0 is the radius at the source; and Fr is the source Froude number defined as follows:

$$\mathrm{Fr} = \frac{U_0^2}{(r_0 g \beta \Delta T)}, \qquad 2.2$$

where g is the acceleration due to the gravity field of the earth, ΔT is an appropriate temperature difference an β is the volumetric expansion coefficient. The Froude number range covered in this experimental work was approximately from 0.7 to 18.

Seban *et al.* (1978) measured temperatures of a heated air jet flowing downward into an isothermal environment. The experiments were performed for a Froude and Reynolds numbers ranging from $4.4x10^1$ to $2.85x10^3$ and 770 and 1923, respectively. Their analysis was based on the integral method, taking a Gaussian distribution for the shear layer, applying the boundary conditions to the equations of continuity, momentum, and energy. Also, they used the approximation introduced by G. I. Taylor, where the mean flow or entrainment velocity at the edge of the flow, is proportional to the local mean vertical velocity (Jaluria Y. 1980). Using the analysis of Morton (1959), Seban *et al.* obtained an expression for the penetration depth of the jet:

$$\frac{Z_p}{r_0} = \left(\frac{1.454}{2^{3/2}\alpha^{1/2}\lambda}\right)\left(2^{1/4}\right)\left(\frac{2\lambda^2}{1+\lambda^2}\right)^{1/2} \mathrm{Fr}^{1/2}. \qquad 2.3$$

Where the Froude number is evaluated at the source, α is the entrainment constant, and λ is a constant that relates the velocity and buoyancy length scales, b and b_T respectively, as follows:

$$\lambda = \frac{b_T}{b}, \qquad 2.4$$

α and λ are universal constants for forced plumes in which local density variations are small; they must be evaluated experimentally. Equation 2.3 has a similar form to that obtained by Turner (1966), Equation 2.1. Using α = 0.055 and λ = 1.1 in the former equation the value of the constant is 2.48. The penetration depth obtained by Seban *et al.* were in good agreement with that obtained with Turner equation. It should be pointed out that neither Turner (1966) nor Seban *et al.* considered in their analysis the effect of the reverse flow on the externally driven jet flow.

Seban *et al.* got a good fit of the temperature profiles to a Gaussian curve as follows:

$$\Delta T = \Delta T_c \exp -\left(r/b_T\right)^2, \qquad 2.5$$

where $\Delta T_c = T_c - T_{\infty x}$ and T_c, $T_{\infty x}$, are the temperature at the centre of the jet and the ambient temperature at the same axial distance, respectively; b_T is the radial location where the ratio of ΔT_c and ΔT_c takes a value of 0.36 (1/*exp*). This ratio will be 1 at the centre of the jet reducing its value as we depart from the centre. The Gaussian profile was considered to start at a distant of 9 radii based on experimental data. They found no correspondence at all with the b_T of the non-buoyant jet. Finally, they observed that the radial temperature measurements reveal wide profiles that extend significantly into the

region of the upward flow, and it is probable that the width of the downward flow is greater than the theoretical value. This implies a substantial interaction between the downward and upward flow and suggests as a possible coincidence the predictability of the centreline temperature and jet penetration by the simple theory that neglects the outer flow.

Typically a buoyant jet discharged into a uniform temperature ambient behaves like a momentum jet in the region near the discharging nozzle, followed by an intermediate region where the influence of the initial momentum force becomes smaller, and a final region where the buoyancy force completely behaves like a plume (Jaluria Y., 1980). Ogino *et al.* (1980) suggest that both momentum jet and pure plume will attain a self preserving profile at some distances from the discharging nozzle, but with a different similarity profile and different scaling laws for the decay of the flow. Therefore, the experimental data of a buoyant jet cannot be correlated with a single curve from the discharge point where it behaves like a momentum jet to the far field where it behaves like a plume.

Ogino *et al.* carried out a dimensional analysis based on the governing equations and the boundary conditions for the vertical round buoyant jet in a uniform temperature and in a linearly stratified environment. For the latter case they included in the energy equation the term $-Su$, where u is the axial velocity and S_o is a dimensionless temperature gradient of ambient fluid, defined as:

$$S_o = \left[\frac{r_0}{\left(T_0 - T_{0\infty}\right)}\right]\frac{dT_{\infty x}}{dx}, \qquad 2.6$$

where r_0, and T_0, $T_{0\infty}$, are the radius, the temperature of the fluid in the jet and the ambient temperature, respectively, all evaluated at the jet discharge.

In their experiments Ogino *et al.* used filtered city water in a tank 2m long, 1m wide and 1m deep. The arrangement of the experiment was very similar to Turner's set-up. The linear temperature profile was achieved by filling the tank layer by layer with water of different temperatures; the resulting temperature profiles were found to be smoothed out in 2h after the tank was filled with fluid. They measured the centreline velocity and temperature using hot-film probe and type K thermocouples respectively. The zero momentum and zero buoyancy heights were determined as the position where the jet centreline temperature jumped discontinuously and the position where it was equal to

the ambient temperature respectively. They also obtained visual corroboration of the zero momentum and buoyancy heights by adding India ink to the jet fluid and determined the zero momentum height as the terminal height of rise and the position of zero buoyancy was assumed as the level where the jet extended horizontally. The experimental correlation's for zero momentum and buoyancy heights are presented in Table 2.1. Finally, Ogino *et al.* pointed out that a different relation should be applied for values of $S\mathrm{Fr}_0 < 10^{-2}$.

Goldman and Jaluria (1986) studied two-dimensional heated air jets discharged downward in a uniform ambient temperature. They measured the penetration depth, which was quantified by defining it as the vertical distance from the jet inflow to the location where the local temperature excess, $T\text{-}T_{x\infty}$, has dropped to 1% of the inlet excess, $T_0\text{-}T_{0\infty}$. In their experiments they allowed the removal of the air through the top of the tank, so that a steady state condition could be attained. They develop an expression for the penetration depth as follows:

$$\frac{Z_p}{r_0} = 3.959\mathrm{Fr}^{0.440} \qquad 0 \le \mathrm{Fr}^{-1} \le 1.0, \qquad 2.7$$

where Fr is defined as in Eq 2.2 with r_0 as the slot width.

Goldman and Jaluria (1986) also observed that the region where the externally induced flow becomes stationary and the reverse flow takes over is found to be very disturbed due the large changes in the flow occurring at this location, which result in an extensive horizontal widening of the flow and in a substantial amount of ambient-fluid entrainment.

Research done by Baines *et al.* (1993) on turbulent water fountains in a closed chamber found that when a negatively buoyant jet is injected in an environment where exists an outlet at the same level of the jet, a sharp interface forms between the injected and the original fluid. This work is focus on the development of the environment velocity, temperature and density profiles. They report that in a closed container a considerable time is required for the front to reach the opposite surface if the height of the initial jet is less than the height of the container.

Zhang and Baddour (1998) measured the maximum penetration of vertical round dense jets in non-stratified environments (0.6<Fr<1600). The jet was salt water and the tank was filled with fresh water. The set-up of their experiment was similar to that present in

Figure 2.2. They finished their experiment before the dense layer reached the height of the nozzle. Following a dimensional analysis they obtained a linear fit for their experimental results. In particular for Fr>49 they report:

$$\frac{Z_p}{r_0} = 3.06\mathrm{Fr}^{1/2}. \qquad 2.8$$

2.3 Numerical simulation of buoyancy affected flows

Tennekes and Lumley (1972) have characterised turbulence motions in terms of irregularity, diffusivity, large Reynolds numbers, three-dimensional vorticity fluctuations, dissipation, and continuum. Most recently Lesieur (1997) has proposed that a flow must satisfy the following criteria before it can be considered to be turbulent:

- Must be unpredictable, in the sense that a small uncertainty as to its knowledge at a given initial time will amplify so as to render impossible a precise deterministic prediction of its evolution.
- It should be able to mix transported quantities much more rapidly than if only molecular diffusion processes were involved.
- It must involve a wide range of spatial wavelengths.

Airflow within a large structure shows different scales, which makes it difficult to identify whether it is artificially induced turbulent flow, transitional airflow, or fully developed turbulent airflow. The common practice is to consider it as turbulent. Among different approaches to model turbulence in rooms the most used turbulence transport model is the k-ε model.

The standard k–ε model is only suitable for fully turbulent flows. Close to solid walls, and some other interfaces, there are inevitably regions where the local Reynolds number of turbulence is so small that viscous effects predominate over turbulent ones (Launder and Spalding, 1974). In principle it is possible to increase the number of grid cells in the near wall region in order to calculate the mean velocity and temperature profile. However, an additional 20 to 30 grids may be required to model this region (Chen, 1992), which significantly increases the computing cost, especially in 3-D cases. Hence to bridge the whole of the near-wall sublayer, most CFD models use semi-empirical wall functions to represent the flow characteristics for these near-wall regions.

The wall functions are simply formulae which attempt to account, in overall fashion, for the effective conductances, sources and sinks of the region between first computational node and the wall, including all the viscosity affected sublayer (Launder, 1984). Wall functions are based on the semi-logarithmic behaviour of the mean velocity and temperature near solid walls (Alamdari, 1991). Unfortunately, at low Reynolds numbers the log-law is not valid. Wall damping need to be applied to ensure that viscous stresses take over from turbulent Reynolds stresses at low Reynolds numbers and in the viscous sub-layer adjacent to solid walls (Versteeg and Malalasekera, 1995).

Bergstrom (1994) points out that eddy viscosity model relations have been shown to be potentially incapable of reproducing the effect of buoyancy on the turbulent transport. He performed a numerical prediction of an airflow configuration, to the fountain-filling box problem (Baines *et al.*, 1990). His computational method marched forward implicitly in time, using a coupled equation line solver to simultaneously update the mean velocity and temperature fields. He modelled the turbulent transport by a low-Reynolds-number (LRN) formulation of the transport equations for the turbulence kinetic energy (k) and its dissipation rate together with an algebraic stress model (ASM) closure. The latter is an economical way of accounting for the anisotropy of Reynolds stresses without going to the full length of solving the Reynolds stress transport equations (Versteeg and Malalasekera, 1995). The numerical grid used two-dimensional cylindrical coordinates and consisted of 50 control volumes in each coordinate directions. Bergstrom compared his results to the case of self-similar axisymmetric buoyant jet, noting that negative buoyancy precludes a self-similar asymptotic state, and concluded that the use of simple jet models to predict the thermal mixing would be inappropriate and would yield unrealistic results. He also compared satisfactorily the jet penetration obtained by his numerical simulation with that calculated based on the correlation of Baines *et al.*(1990) for $Fr = 12.9$.

The standard k-ε model was used by Li and Huai (1995) to model numerically a vertical round buoyant jet in a static, linearly stratified environment. They solved the two dimensional convective-diffusion type equations using the iterative Hybrid Finite Analytic Method (HFAM) with a staggered grid, and compared their results with experimental data obtained by Ogino *et al.* (1980). The number of grid points with uniform space used in this work were 51 and 101 in the x and r directions respectively. Li and Huai pointed out that most of the literature on experimental measurements does

not provide the profiles for the initial turbulent kinetic energy, k_0 and its dissipation rate, ε_0, so, based on previous experimental work they assumed Gaussian profiles:

$$0 \le r \le \frac{d}{2}\ ,\ x = 0;\ k_0 = k_{0c}\exp\left(-1.7r^2\right),\ k_{0c} = 0.06u_0^2\ ,$$
$$\varepsilon_0 = \varepsilon_{0c}\exp\left(-1.7r^2\right),\ \varepsilon_{0c} = \frac{0.06u_0^3}{d}\ , \qquad 2.9$$

where the centreline values of k and ε at the exit are denoted by k_{0c} and ε_{0c} respectively. When experimental data for the boundary conditions of k_0 and ε_0 are not available, it is usual to estimate them based on fully developed mean field profiles (Versteeg and Malalasekera, 1995; AEA, 1997). In this case:

$$k_0 = 1.5\left(u_0 T_i\right)^2$$
$$\varepsilon_0 = \frac{k_0^{1.5}}{0.3d} \qquad 2.10$$

where T_i is the turbulent intensity and is linked to the kinetic energy and a reference mean flow velocity U_{ref} as follows:

$$T_i = \frac{\left(\frac{2}{3}k\right)^{1/2}}{U_{ref}} \qquad 2.11$$

The solution procedure used by these researchers required an initial guess for the maximum height of rise for buoyant jet. This initial guess is given by an empirical formula similar to that obtained by Ogino *et al.* (1980). Their predicted results coincided with others that the whole field of buoyant jets is static linearly stratified environments can be divided into three main regions, namely buoyant jet region, mushroom-cloud region and spreading layer region. Since the numerical results of Li and Huai showed a good agreement with the experimental data, they concluded that HFAM is an effective numerical method for the calculation of the convective-diffusion type equation.

The density-profile evolution on a stably stratified environment mixed by a turbulent non-swirling round jet pointing downward was modelled by Larson and Jönsson (1995) and their results are validated against experimental data reported elsewhere (Larson and Jönsson, 1994). The model used by these researchers employed integral formulations of the conservation equations for volume, momentum, and buoyancy for the jet and plume, respectively. The model used by these researchers did not consider any turbulence modelling. The coupled system of equations is solved for steady-state conditions at each

time step. A Gaussian shape is assumed for the radial distribution of velocity and buoyancy in the jet, whereas a top-hat distribution is used for these quantities in the plume. However, the dynamic interaction and momentum transfer between the jet and plume is not modelled, because of the entrainment of plume water into the jet is neglected. Some difficulties of the model of Larson and Jönsson include the necessity of knowing the maximum jet penetration to establish boundary conditions, and to define an upper limit of the spreading of the plume. Also, the model requires a prescription for the smooth transition in the density felt by the jet between the density of the plume and the density of the ambient fluid when calculating the maximum jet penetration in the buoyancy equation of the jet. The model also requires a way of accounting for additional mixing induced by the horizontal spreading of the plume. The model compared favourably with the data for Froude numbers exceeding about 20, and underestimated the mixing for Froude numbers below 15. Larson and Jönsson attributed the latter to neglecting of additional mixing in the model, which occurs when the jet changes into a plume, since this additional mixing is relatively more important for lower Froude numbers.

Homan and Soo (1997) presents numerical solutions for the model of the stratified flow into a tall tank with a single jet of cold liquid entering horizontally at the bottom filled initially with hot liquid which is removed at the top of the tank. They mention that there are relatively few numerical simulations of the tank-filling process reported in the literature. Furthermore, studies of gravity currents have traditionally been motivated by problems such as local exchange and atmospheric flows, which differ notably from common engineering situations in the smaller scale and in confined volumes.

The model proposed by Homan and Soo is two-dimensional and transient and it is assumed that the tank is sufficiently tall that inlet and outlet are decoupled. They used a start-up function to ramp the inlet boundary conditions on velocity and temperature from their initial condition to their steady-state values while maintaining finite rates of change. The length of the start-up period was fixed at two dimensionless time units to avoid the introduction of temporal oscillations on the convective time scales due to numerical effects. The numerical simulations were reported for a laminar, work fluid with properties similar to water and Re = 50, Pr = 10, T = 10°C; and Fr = 1.

One of the main conclusions of Homan and Soo is that the filling of a stratified storage tank initially full of hot water by an inflow of cold water produces a wide range of

gravity-driven phenomena. The initial inflow of cold fluid produces a gravity current that traverses the width of the tank, thereby forming a thermocline-type stratification. The presence of the thermoclyne forms a barrier between the uniform flow above the thermocline and the recirculating flow beneath the thermocline driven by the inlet jet.

Sommer *et al.* (1997) investigated the capability of different turbulence models to predict the formation of gravity waves and the countergravity fluxes that are developed in a stably stratified flow. These researchers state that under stable stratification, countergradient fluxes develop to keep the energy budget in equilibrium, and oscillations are formed in the evolution of the Reynolds normal stress aligned with the gravity vector, temperature variance and the turbulent vertical heat flux. These oscillations can be interpreted as an exchange of energy between turbulent kinetic energy and potential energy associated with the temperature variance, and these are know as internal gravity waves. The formation of the gravity waves leads a to reduction in vertical mixing and the ultimate collapse of turbulence.

Numerical simulation of these kinds of flows have been undertaken using additional equations to account for the potential energy and its dissipation rate on the k-ε type and second-order models. Sommer *et al.* studied systematically those models using a Runge-Kutta method with adaptive step size control. They concluded that the k-ε models fail to reproduce the essential physics of the turbulence. Particularly, they are unable to reproduce the oscillations associated with the exchange of energy between turbulent kinetic and potential energy. Thus, it is not sufficient to account for nonequilibrium effects alone in the calculations of stably stratified flows. Furthermore, k-ε model fail in the predictions of the oscillation frequency and amplitude when it is modified to account for history effects in the evolution of the normal heat flux, assuming turbulence isotropy. Finally, they reach a conclusion that gravity waves can only be predicted correctly if turbulence isotropy is not assumed and history effects are taken into account. The latter implies that is not appropriate to apply the concept of 'self-preservation', where effects of the source have been lost (Tennekes and Lumley, 1972).

2.4 Numerical simulation of moisture migration in porous media

The phenomenon of moisture migration in an unsaturated porous medium that involves the combined heat and mass transfer with phase change occurs frequently in nature as well as in various engineering processes. Movements of moisture in soil and insulation material, drying and wetting processes in the chemical industry are just a few examples. An analysis of this phenomenon is complicated by various factors. The structure of the solid matrix in a porous medium varies widely in shape and size. It may, for instance, be composed of cells, fibres or grains. The randomly distributed voids in the unsaturated porous medium contain different distributions of moisture (in liquid or vapour phase or both) and air. Heat transfer in such a medium occurs by conduction in all the phases, as well as by advection in the fluid phases. Mass transfer also occurs between the voids of the medium.

Withaker (1998) pointed out in his review that in many situations the multiphase transport equations for heat, mass and momentum transfer are inferred from single-phase analogies. This leads to the use of equations containing effective transport coefficients that one hopes can be measured experimentally, and in some cases this approach is successful. Darcy's law is a classic example in which spatially smoothed momentum equation can be deduced by the solution of Stokes' equations for laminar flow in a tube, and reliable experiments can be carried out for porous media to determine the permeability tensor. However, single-phase flow in rigid porous medium is a rather benign process in which the interface is fixed in space and subject only to the no-slip condition. If we move on to consider two-phase flow, we find an entirely different situation involving severe theoretical and experimental challenges. One can contrast the simplicity of the measurements of the permeability for single-phase flow with the very complex experiments required for the determination of the coupling permeability tensors for two-phase flow. Coupling in two-phase flow occurs at two levels: at the macroscopic on Darcy scale, where the two momentum equations are joined by the capillary pressure-saturation relation, and at the microscopic or closure scale, where the coupling at both levels requires a theoretical framework and thoughtful experiments.

Somasundaram *et al.* (1989) mentions that a detailed study of the transport processes occurring within the solid matrix and in the voids is very complicated even for a regularly shaped matrix. The normal procedure in such a case is to consider the porous

medium as a continuum. The heat and mass transfer processes then have to be described by conservation equations.

The experimental approach has been extensively used, but it may become expensive in both time and resources. Moreover, experimental approaches often lack the flexibility needed when a sensitivity study is desired. At the moment, powerful computer facilities are available at affordable cost. Thus the numerical approach seems a very promising and accurate way to predict transport phenomena and their effect in all situations. However, CFD simulations are not commonly in use in industry yet and are certainly not the principal basis for design decisions (Péniguel, 1998).

The CFD approach to model transport phenomena has been used to model processes common in the Chemical Industry. Gouvalias *et al.* (1993) used a commercial CFD code to simulate adsorption/regeneration cycles in packed-bed reactors. They solve the full two-dimensional Navier-Stokes equations, energy and species conservation equations in steady state and transient modes using a prescribed constant turbulence viscosity inside the fixed bed. Also, Tierney *et al.* (1998) used two different CFD codes to simulate the flow in annular packed beds and compared their results against experimental data. They modified the codes to include Ergun terms to the porous region. Based in the experimental data they conclude that CFD is a realistic design tool capable of predicting gas distribution adequately.

CFD has only recently been applied to food processing applications. The simulations include airflow in clean rooms, ovens and chillers; flow of foods in continuous-flow systems; and convection patterns during in-container thermal processing (Scott and Richardson, 1997).

To study heat and mass transfer in porous bulks of particulate foodstuffs (potatoes) Xu and Burfoot (1999[a]) used the CFD package CFX-4.1. The mass, momentum and energy equations in a three dimensional model were solved to predict the air flows, temperature and moisture changes of the air and solids. The interaction between the airflows and the porous media were described by the Ergun equation. Moisture diffusion and heat transfer within the solids was predicted assuming the solids to be spheres, and the heat of respiration was included in the model as an empirically derived function of temperature. In this work, the store of foodstuff is subdivided into a set of imaginary control volumes called cells. Some of the cells contain air while others contain air and

solid spherical particles, the foodstuff. The latter mixture is treated as a porous medium and the flow resistance of that medium is described by a Darcy coefficient. Predicted weight loss of the bed in a 4-day test period was within 5% of the measured value.

More recently Xu and Burfoot (1999[b]) included the simulation of condensation in their calculations. Although they are aware that air flows, and the associated heat and moisture, are always three-dimensional and time dependent in crop store, in this work they simplified the three dimensional problem to a one-dimensional case. This was done because complete information about the store was not available and a direct simulation would be lengthy and require a huge computer resource. Other assumptions made were that air flow around each duct was periodic along the store, implying that all of the ducts behave the same; and symmetry about the centre line, which allowed then to use a symmetry plane and simulate only half of the section, as depicted in Figure 2.3. Nonetheless, they showed how condensation develops and why can it be found in various region of the bulk and mid-way between the air supply ducts.

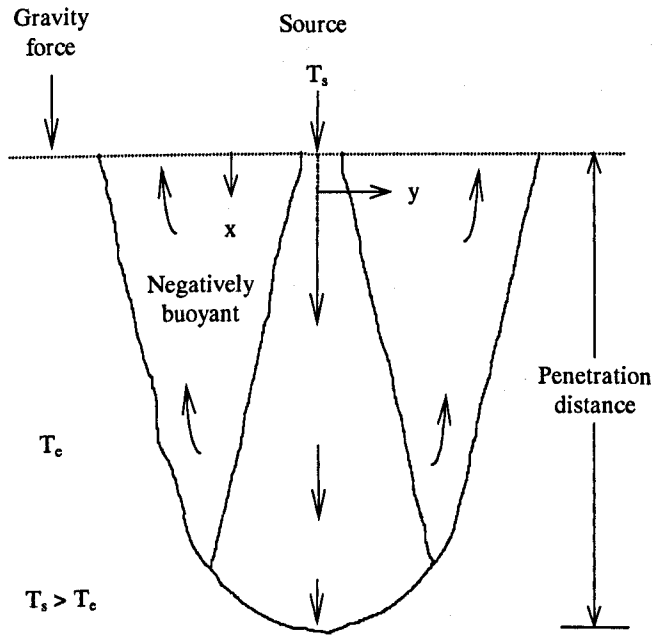

Figure 2.1. Sketch of a negatively buoyant jet.

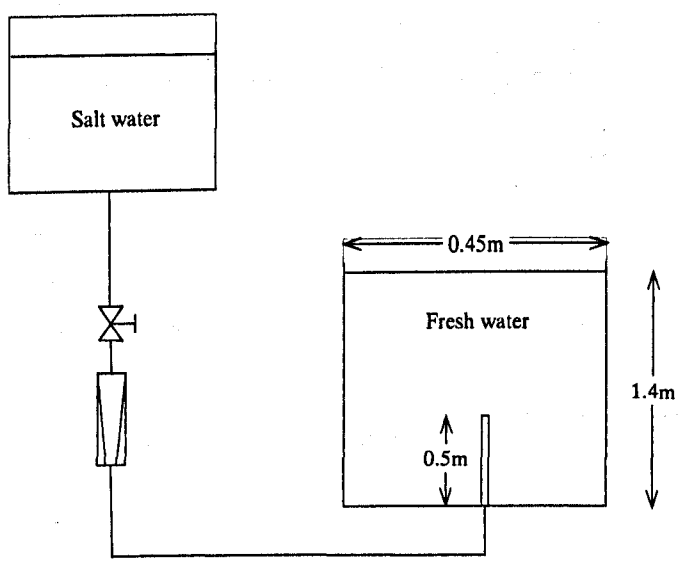

Figure 2.2. Sketch of Turner's (1966) experimental apparatus.

Table 2.1. Experimental relations of Ogino *et al.* (1980) for buoyant jet discharged in a linearly stratified environment.

Zero momentum and zero buoyancy heights		
$\frac{Z_p}{r_0 Fr_0^{1/2}} = 5.95(S_o Fr_0)^{-1/3}$	Momentum	$10^{-3} < S_o\, Fr_0 < 10^3$
$\frac{Z_p}{r_0 Fr_0^{1/2}} = 4.1(S_o Fr_0)^{-2/5}$	Buoyancy	$10^{-2} < S_o\, Fr_0 < 10^3$

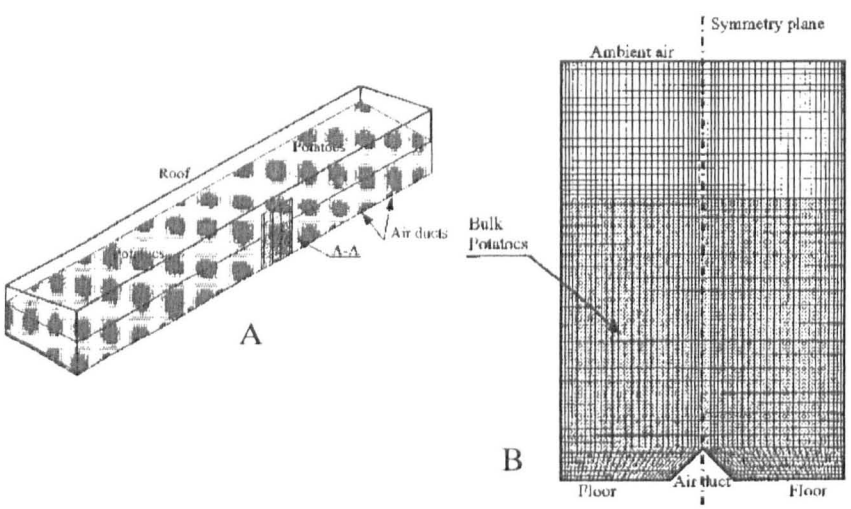

Figure 2.3. A) Schematic diagram of a quarter section of a bulk potato store. B)Two dimensional domain representing the bulk store. (Xu and Burfoot, 1999)

3 NUMERICAL MODELLING THEORY

3.1 Introduction

Numerical modelling is based on solving a set of partial differential equations that describe the variation of velocity, pressure and any other scalar variable. These variables are calculated at discrete points throughout the computational domain.

This chapter present the continuity, momentum and energy equations and approximations adopted to simplify these equations. As we are mainly interested in the mean flow characteristics, we consider only steady flows. Therefore, all transient terms have been removed from the equations, and in the case of turbulent convection, the equations have been time-averaged. Finally, a brief explanation of the process to solve the differential equations is presented.

3.2 Governing equations

The equations that we aim to solve in order to describe the movement of the fluid are written with reference to the Cartesian coordinates x, y and z. The index notation is used to write the equations.

$$\frac{\partial u_i}{\partial x_i} = 0. \qquad 3.1$$

Equation 3.1 is known as the continuity equation for an incompressible fluid.

The conservation of momentum is given by:

$$\rho u_j \frac{\partial u_i}{\partial x_j} = \frac{\partial \sigma_{ij}}{\partial x_j} + \rho g_i. \qquad 3.2$$

The stress tensor for a Newtonian fluid, σ_{ij}, is given by:

$$\sigma_{ij} = -\left(p + \frac{2}{3}\mu \frac{\partial u_j}{\partial x_j} \right) \delta_{ij} + 2\mu D_{ij}, \qquad 3.3$$

where p is the hydrodynamic pressure, μ is the viscosity, δ_{ij} the Kroeneker delta, which is 1 when $i = j$ and 0 otherwise. For incompressible flows, the second term in brackets in Equation 3.3 is zero by virtue of the continuity equation. The rate of strain is defined by:

$$D_{ij} = \frac{1}{2}\left(\frac{\partial u_i}{\partial x_j} + \frac{\partial u_j}{\partial x_i}\right). \qquad 3.4$$

In Equation 3.2 g_i is the component of the gravitational acceleration $\boldsymbol{g}$ in the direction of the Cartesian coordinate x_i. In this work the gravity is assumed to act in the negative z-direction, i.e. $\boldsymbol{g} = -g\boldsymbol{k}$. In flows accompanied by heat transfer, the fluid properties are normally functions of temperature. The variations may be small and yet be the cause of the fluid motion. If the density variation is not large, one may treat the density as constant in the convection terms, and treat as variable only in the gravitational term. This is called the Boussinesq approximation. In this case the term ρg_i can be split in two parts:

$$\rho_0 g_i + (\rho - \rho_0) g_i, \qquad 3.5$$

where ρ_0 is a reference density. The first part of Equation 3.5 can then be included with the pressure and retaining the density variation only in the gravitational term. Finally, we can write:

$$\rho u_j \frac{\partial u_i}{\partial x_j} = -\frac{\partial p}{\partial x_j}\delta_{ij} + \frac{\partial}{\partial x_j}\left(2\mu D_{ij}\right) + (\rho - \rho_0) g_i. \qquad 3.6$$

Assuming that the density varies linearly with temperature, the last term in 3.6 can be expressed as:

$$(\rho - \rho_0) g_i = -\rho_0 g_i \beta (T - T_0), \qquad 3.7$$

where β is the coefficient of volumetric expansion. This approximation introduces errors of the order of 1% if the temperature differences are below 2°C for water and 15°C for air (Ferziger and Peric, 1997).

As the density in buoyancy term of the momentum equation is locally temperature dependent, an additional equation for solving the temperature is required. This is the energy conservation equation:

$$\rho c_p u_i \frac{\partial T}{\partial x_i} = \lambda \frac{\partial^2 T}{\partial x_i^2} + S_h, \qquad 3.8$$

where c_p is the specific heat at constant pressure and λ is the thermal conductivity. In Equation 3.8 the first term in the R.H.S represents the influence of conduction heat transfer within the fluid, according to the Fourier law of conduction. The second term, S_h, is the volumetric rate of heat generation.

On the whole any conservation equation can be written in a general form. The differential form of the generic conservation equation in steady state is:

$$\frac{\partial(\rho u_i \phi)}{\partial x_i} = \frac{\partial}{\partial x_i}\left(\Gamma \frac{\partial \phi}{\partial x_i}\right) + S_\phi . \qquad 3.9$$

The three terms in Equation 3.9 are the convection term, the diffusion term, and the source term. The dependent variable ϕ can stand for a variety of different quantities, such as fluid age, mass fraction of chemical species or the turbulence kinetic energy. For each of these variables, an appropriate meaning will have to be given to the diffusion coefficient Γ and the source term S.

3.3 Turbulence modelling

There are different methods of predicting turbulent flows. The method followed in this work is based on equations obtained by averaging the equations of motion over time (if the flow is statistically steady), over a coordinate in which the mean flow does not vary. This approach is called one-point closure and leads to a set of partial differential equations called the Reynolds averaged Navier-Stokes equations. These equations do not form a closed set so this method requires the introduction of approximations or a turbulence model. This section describes the k-ε model, which is probably the most widely used in the world.

In a statistically steady flow, every variable can be written as the sum of an average value and a fluctuation about that value:

$$\phi(x_i,t) = \bar{\phi}(x_i) + \phi'(x_i,t), \qquad 3.10$$

where

$$\bar{\phi}(x_i) = \lim_{\Delta t \to \infty} \frac{1}{\Delta t} \int_0^{\Delta t} \phi(x_i,t)dt . \qquad 3.11$$

Here t is the time and Δt is the averaging interval. This interval must be large compared to the typical time scale of the fluctuations. If Δt is large enough $\overline{\phi}$ does not depend on the time at which the averaging is started. The averaging process is named Reynolds averaging, the result of applying to the momentum equation is the Reynolds-averaged Navier-Stokes equations.

From Equation 3.11, it follows that $\overline{\phi'} = 0$. Thus, averaging any linear term in the conservation equations gives the identical term for the averaged quantity. For a quadratic non-linear term we get two terms, the product of the average and a covariance:

$$\overline{u_i\phi} = \overline{(\overline{u}_i + u_i')(\overline{\varphi} + \varphi')} = \overline{u}_i\overline{\phi} + \overline{u_i'\phi_i'}\,. \qquad 3.12$$

The last term in Equation 3.12 is zero only if the two quantities are uncorrelated; this is rarely the case and, as a result, the conservation equations contain term such as $\rho\overline{u_i'u_j'}$, called the Reynolds stresses, and $\rho\overline{u_i'\phi'}$, known as the turbulent scalar flux, among others.

The presence of the Reynolds stresses and the turbulent scalar flux in the conservation equations means that the latter are not closed. Closure requires some approximations, which usually take the form of prescribing the Reynolds stresses and the turbulent scalar flux in terms of the mean quantities.

The eddy viscosity model is based in the assumption that the effect of turbulence can be reproduced as an increased viscosity, this leads to define the Reynolds stresses as:

$$-\rho\overline{u_iu_j} = \mu_t\left(\frac{\partial\overline{u}_i}{\partial x_j} + \frac{\partial\overline{u}_j}{\partial x_i}\right) - \frac{2}{3}\rho\delta_{ij}k\,, \qquad 3.13$$

where k is the turbulent kinetic energy given by:

$$k = \frac{1}{2}\overline{u_i'u_i'}\,. \qquad 3.14$$

The scalar flux is given by:

$$-\rho\overline{u_i'\phi'} = \Gamma_t\frac{\partial\overline{\phi}}{\partial x_i}\,, \qquad 3.15$$

where Γ_t is the eddy diffusivity. In particular the eddy diffusivity for heat is related to the eddy diffusivity for momentum by:

$$\Gamma_T = \frac{\mu_t}{\sigma_T}. \qquad 3.16$$

Here σ_T is called the turbulent Prandtl number. The Reynolds analogy assumes that σ_T equals one, suggesting that heat is transported as rapidly as momentum.

In the k-ε turbulence model the eddy viscosity is estimated as the product of a characteristic velocity scale of the turbulent velocity fluctuations and a appropriate length scale of the turbulent eddies. In the k-ε model, $k^{1/2}$ is used as the turbulence velocity scale and $k^{3/2}/\varepsilon$ is taken for the turbulence length scale. The following relation is then found for the eddy viscosity:

$$\mu_t = C_\mu \rho \frac{k^2}{\varepsilon}, \qquad 3.17$$

where C_μ is a dimensionless constant.

In this work we will use the k-ε model, which includes two extra differential equations that accounts for the effects of turbulence. Also, the equations presented are for the time-mean values of the variables. The derivation of the equation can be found elsewhere (Tennekes and Lumley, 1972; Chen and Jaw, 1998). The final set of equations to be solved for turbulent buoyant flows is:

$$\frac{\partial u_i}{\partial x_i} = 0, \qquad 3.18$$

$$\rho u_j \frac{\partial u_i}{\partial x_j} = \frac{\partial}{\partial x_j}\left(2(\mu + \mu_t) D_{ij}\right) - \frac{\partial p}{\partial x_j} - \rho \beta \Delta T g_j, \qquad 3.19$$

$$\rho u_j \frac{\partial T}{\partial x_j} = \frac{\partial^2 T}{\partial x_j x_j}\left(\frac{\mu}{\mathrm{Pr}} + \frac{\mu_t}{\sigma_T}\right) + S_h, \qquad 3.20$$

$$\rho u_j \frac{\partial k}{\partial x_j} = \frac{\partial}{\partial x_j}\left[\left(\mu + \frac{\mu_t}{\sigma_k}\right)\frac{\partial k}{\partial x_j}\right] + P - \rho\varepsilon + G, \qquad 3.21$$

$$\rho u_j \frac{\partial \varepsilon}{\partial x_j} = \frac{\partial}{\partial x_j}\left[\left(\mu + \frac{\mu_t}{\sigma_\varepsilon}\right)\frac{\partial \varepsilon}{\partial x_j}\right] + C_1 \frac{\varepsilon}{k} P - C_2 \rho \frac{\varepsilon^2}{k} + C_1 \frac{\varepsilon}{k} C_3 G. \qquad 3.22$$

The last two equations can be read as:

Transport of k or ε by convection	=	*Transport of k or ε by diffusion*	+	*Rate of production of k or ε*	-	*Rate of destruction k or ε*	+	*Production or destruction of k or ε by buoyancy*

The third term in the R.H.S. of Equation 3.21represents the rate of production of turbulence by shear stresses and is defined by:

$$P = \mu_t D_{ij} \frac{\partial u_i}{\partial x_j}. \qquad 3.23$$

Applying the Boussinesq approximation the term G can be expressed in terms of the temperature gradient:

$$G = -\beta g_j \frac{\mu_T}{\sigma_T} \frac{\partial T}{\partial x_j}. \qquad 3.24$$

The sign of this source term is dependent on the sign of the temperature gradient in the direction of gravity. In Equation 3.24, if the temperature is decreasing with height the thermal gradient will be negative and the buoyancy force will increase the turbulence. On the other hand if the temperature is increasing with height, the thermal gradient will be positive and the buoyancy force will reduce the turbulence.

The standard *k-e* model employs values for the constants that are arrived at by comprehensive data fitting for a wide range of turbulent flows. Finally, the values of the constants are (Tennekes and Lumley, 1972; Lee and Chen, 1996; Chen and Jaw, 1998):

C_μ=0.09, C_1=1.44, C_2=1.92, C_3=0.8, σ_T=1.0, σ_k=1.0, σ_ε=1.3.

3.4 Solution of the governing conservation equation in CFD

The analysis of s fluid system using a CFD code comprises three main stages:

I. Pre-processing. This stage involves the definition of the computation domain and the subdivision of the domain into a number of smaller sub-domains.

II. Processing. Here the integrated governing equations with the appropriate boundary condition are discretised and the resulting set of algebraic equation solved.

III. Post-processing. The generated data is presented in the different forms for analysis.

In this section a brief description of these stages will be presented. The CFD literature contains some excellent background material. Two good examples of these are the

books by Versteeg and Malalasekera (1995) and Ferziger and Peric (1997). Much of the information presented in this section is taken from those sources.

The first stage to obtain a numerical solution is to discretise the geometric domain, i.e. a numerical grid must be defined. A numerical grid divides the solution domain into a finite number of subdomains or control volumes. Some of the options available are the following:

- Structured (regular grid). Consist of families of grid lines with the property that members of a single family do not cross each other and cross each member of the other families only once. This allows the lines of a given set to be numbered consecutively. The position of any grid point (or control volume) within the domain is uniquely identified by a set of two or three indices. This is the simplest grid structure. The disadvantage of structured grids is that they can be used only for geometrically simple solution domains. Also, it may be difficult to control the distribution of the grid points. An example of this type of grid is shown in Figure 3.1.

- Block-structured grid. This type of grid divides the domain in blocks, each of blocks consist of structure grids. The structure of the blocks may be irregular and they may or may not overlap. This kind if grid is more flexible than the previous one, as it allows the use of finer grids in regions where greater resolution is required. Figure 3.2 shows an example of this type of grid.

- Unstructured grid. Here, the elements or control volumes may have any shape and there are no restrictions on the number of neighbour elements or nodes. In practices, three-dimensional grids are made of tetrahedral of hexahedral elements. The advantage of the flexibility is offset by the disadvantage of the irregularity of the data structure. An example of this type of grid is shown in Figure 3.3.

The next stage requires choosing a method to perform the numerical solution of the governing equations. The most common methods are the finite difference method, the finite element method and the finite volume method. In this work we will use the later, thus the explanation of the solution of the governing equation will be orientated towards the finite volume method.

The finite volume method uses the integral form of the conservation equations. The solution domain is subdivided into a finite number of contiguous control volumes, and

the conservation equations are applied to each control volume. Interpolation is used to express variable values at the control volume surface in terms of the centre control volume values or nodal values. Surface and volume integrals are approximated using suitable formulae. As a result, one obtains an algebraic equation for each control volume, in which number of neighbour nodal number appear.

The formal integration over a control volume of Equation 3.9 gives:

$$\int_A \mathbf{n}\cdot(\rho\phi\mathbf{u})\,dA = \int_A \mathbf{n}\cdot(\Gamma grad\phi)\,dA + \int_{CV} S_\phi dV\,. \qquad 3.25$$

Where **n** is a unit vector oriented outwards form the control volume. The algebraic equation for a particular control volume has the form:

$$a_p\phi_p + \sum_n a_n\phi_n = S\,. \qquad 3.26$$

Here p denotes the node at which the partial differential equations is approximated and index n runs over the neighbour nodes. The node p and its neighbours form what is called the computational molecule, as shown in Figure 3.4. The coefficients a_n involve geometrical quantities, fluid properties and, for non-linear equations, the variable value themselves. S contains all the terms that do not contain unknown variable values; they are presumed known.

The number of algebraic equations and unknowns are equal to the number of control volumes. If we sum equations for all control volumes, we obtain the global conservation equation, since surface integrals over inner control volume faces cancel out. To obtain an algebraic equation for each control volume, the surface and volume integrals need be approximated using appropriate formulae.

The net flux through the control volume boundary is the sum of integrals over the six control faces:

$$\int_S f dS = \sum_q \int_{Sq} f dS\,. \qquad 3.27$$

Here f is the component of the convective of diffusive vector in the direction normal to the control volume face. One approach to locate the nodes in the grid is to assign the node to the centre of the control volume. The integral in Equation 3.27 is approximated in terms of the variable values at one or more locations on the cell face, then the cell face value are approximated in terms of the nodal (control volume centre) values. Differential methods to approximate the value of ϕ and its normal derivative have been

developed. The most common for its robustness it's the hybrid-differencing scheme, which is based on a combination of central and upwind schemes.

To approximate the value at the centre of a face of a control volume, the central differencing scheme uses linear interpolation between the two nearest nodes. For example, at location '*e*' in Figure 3.5 on a cartesian grid we have:

$$\phi_e = \phi_E \lambda_e + \phi_p (1 - \lambda_e) . \qquad 3.28$$

Where the linear interpolation factor is defined as:

$$\lambda_e = \frac{x_e - x_p}{x_E - x_p} = \frac{\Delta x_{Pe}}{\Delta x_{EP}} . \qquad 3.29$$

The assumption of a linear profile between the P and E nodes also offers the simplest approximation of the gradient, which is needed for the evaluation of diffusive fluxes:

$$\left(\frac{\partial \phi}{\partial x}\right)_e = \frac{\phi_E - \phi_P}{x_E - x_P} . \qquad 3.30$$

By using the Taylor series expansion it can be show that Equation 3.28 is second order accurate. The truncation error term is proportional to the square of the grid spacing, on uniform or non-uniform grids. Also, this scheme may produce oscillatory solutions.

One of the major disadvantages of the central differencing scheme is its inability to identify flow direction. In a flow dominated by convection from west to east, the east cell should receive much stronger influence from node E than from node P, as sketched in Figure 3.6. The upwind differencing scheme approximates ϕ_e by its value at the node upstream of '*e*', as follows:

$$\phi_e = \begin{cases} \phi_P \text{ if } (\mathbf{u} \cdot \mathbf{n}) > 0 \\ \phi_E \text{ if } (\mathbf{u} \cdot \mathbf{n}) < 0 \end{cases} . \qquad 3.31$$

The upwind differencing scheme retains only the first term of a Taylor series expansion. Its leading truncation error term resembles a diffusive flux:

$$f_{ed} = \Gamma_e \left(\frac{\partial \phi}{\partial x}\right)_e = \frac{(\rho u)_e \Delta x}{2} \left(\frac{\partial \phi}{\partial x}\right)_e . \qquad 3.32$$

The truncation error, also called by some authors 'numerical diffusion', is magnified in multidimensional problems if the flow is oblique to the grid. Peaks or rapid variations in the variables will be smeared out and very fine grids are required to obtain accurate solutions.

The hybrid-differencing scheme blends the central differencing scheme and the upwind differencing scheme, switching between one or the other depending on the local Peclet number:

$$\mathrm{Pe} = \frac{\rho u \Delta x}{\Gamma}. \qquad 3.33$$

The hybrid-differencing scheme changes for central differencing to upwind differencing when Pe>2. The scheme is highly stable when compared with higher order schemes. The disadvantage is that the accuracy in terms of Taylor series truncation error is only first-order.

The advection terms in the momentum equations have the same form as in the generic conservation equation. However, the solution of the continuity and momentum equations presents two problems:

- The convective terms of the momentum equations contain non-linear quantities.
- The strong coupling between equations. The most complex issue is the contribution from the pressure, which has not analogue in generic equation.

The numerical arrangements already outlined may become more complicated when coupled equations for vector fields are being solved. The collocated or non-staggered arrangement, Figure 3.7, stores all the variables at the same set of grid points and use the same control volumes for all variables. Since many of the terms in each equations are essentially identical, the number of coefficients that must be computed and stored is minimised and the programming is simplified by this choice. The use of a collocated arrangement for incompressible flow computations presents difficulties with the pressure-velocity coupling and the occurrence of oscillations in the pressure. This problem is addressed by using interpolation algorithms, such as the Rhie-Chow algorithm, to obtain the velocity components and pressure on control volume faces from those on control volume centres.

The most common approach to solve the continuity and momentum equations is by using a pressure-correction method. In this type of method a guessed pressure field is used to solve the momentum equations and a pressure correction equation, deduced from the continuity equation, is solved to obtain a pressure correction field which is in turn used to updated the velocity and pressure field. A flow diagram of the broadly used

Semi-Implicit Method for Pressure-Linked Equations (SIMPLE) developed originally by Patankar and Spalding (1972) is presented in Figure 3.8.

The result of the discretisation process is a system of algebraic equations, which are linear or non-linear according to the nature of the partial differential equations from which they are derived. However, whether the equations are linear or not, efficient methods for solving linear systems of algebraic equations are needed.

There are two families of solution techniques for linear algebraic equations: direct methods and indirect or iterative methods. In the former the number of operations to the solution of a system of M equations with M unknowns in on the order of M^3, thus, the simultaneous storage of M^2 coefficients of the set of equations imposes a huge demand of core memory. The matrices derived from partial differential equations are always sparse, i.e. most of their elements are zero. Iterative methods take advantage of this situation, because only non-zero coefficients of the equations need to be store in core memory. This fact has favoured the use of iterative method over direct methods. An iterative method works by guessing a solution and using the equation to systematically improve it.

In most CFD codes the iteration procedure is used at two levels: an inner iteration to solve for the spatial coupling for each variable and an outer iteration to solve for the coupling between variables. In the inner iteration the set of linearised difference equations for a particular variable, one equation for each control volume in the flow, is solve by an iterative solution method, such Stone or ICCG (Conjugate gradient method using incomplete Cholesky decomposition). The outer iteration is controlled by a convergence criterion set in the SIMPLE algorithm.

The finite volume method requires that the boundary fluxes either be known or expressed in terms of known quantities and interior nodal values. Usually, at an inlet boundary, all quantities have to be prescribed, this type of condition is known mathematically as Dirichlet conditions. Although the mean field components are usually known, and therefore be specified, the turbulent kinetic energy, k, and the dissipation rate, ε, tend to be less well defined. In this case it is usual to approximate them with the use of the following assumed empirical forms:

$$k_{inl} = 0.002U_{inl}^2;\ \varepsilon = \frac{k_{inl}^{1.5}}{0.3D_h}. \qquad 3.34$$

Here U_{inl} and D_h are the imposed velocity at the inlet boundary and the hydraulic diameter, respectively. The approximations of Equation 3.34 essentially assumes that the fluid is similar to fully developed pipe flow.

Sometimes the net mass flowing out the system is known, however at the outlet little is known about the flow. For this reason, these boundaries should be set as far downstream of the region of interest as possible. Otherwise, error may propagate upstream. In mass flow boundaries imposed at the outlet of the system Neumann boundary conditions are imposed on all transported variables. All variables are given a zero normal gradient, which is equivalent to an assumption of fully developed flow at the outlet. In this type of boundary conditions the pressure is extrapolated from upstream . In the commercial code used in this work, in order to maintain global mass continuity, a procedure for the mass flow boundary condition is implemented as follows:

- The normal derivatives of velocity are set to zero at the end of a velocity update.
- The mass conservation difference is evaluated.
- A constant multiple of the unit outward normal to the velocity is added at each outlet control volume.

This procedure modifies the zero gradient condition on the velocity by setting the normal velocity gradient equal to a constant multiple of the unit outward normal.

There are situations where the mass flow rate is not known, but the pressures at the inlet or outlet or both are prescribed. The conditions imposed at outflow through a pressure boundary are: Dirichlet boundary conditions on pressure and Neumann boundary conditions for velocity and all other transport quantities, i.e. zero normal gradients.

At an impermeable wall, the following condition applies:

$$u_i = u_{i,wall} \qquad 3.35$$

This condition follows from the fact that viscous fluids stick to solid boundaries (no-slip conditions).

Since there is no flow through the wall, convective fluxes of all quantities are zero. For scalar quantities the diffusive fluxes may be zero (adiabatic walls), may be specified (prescribed heat flux), or the value of the scalar may be prescribed (isothermal walls).

Finally, turbulence quantities near the wall are calculated using wall functions, which rely on the assumption of a logarithmic region in the velocity profile. In the logarithmic layer, the profile is:

$$u^+ = \frac{\bar{v}_t}{u_t} = \frac{1}{\kappa}\ln n^+ + B \qquad 3.36$$

Where $\bar{v}_t$ is the mean velocity parallel to the wall, u_t is the shear velocity, κ is the von Karman constant ($\kappa = 0.41$), B is an empirical constant related to the thickness of the viscous sublayer and n^+ is the dimensionless distance from the wall.

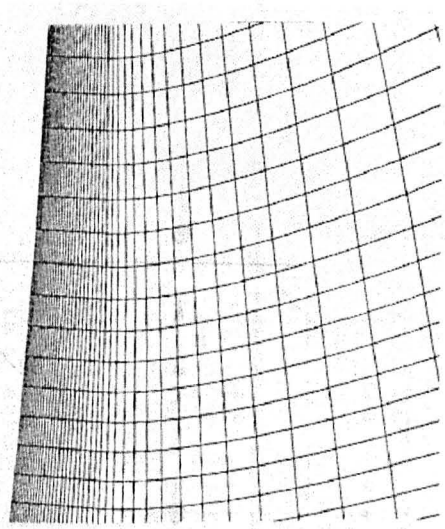

Figure 3.1. Structured grid. (From Hagmeijer and De Cock. 1992)

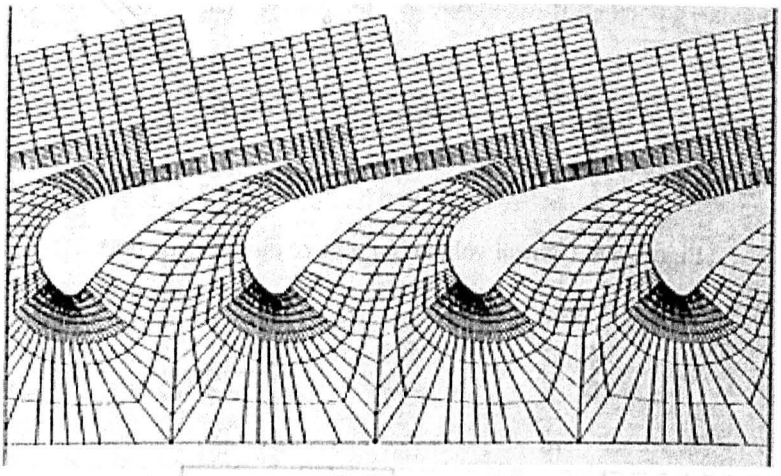

Figure 3.2. Block-structure grid. (From Mensink and Deconinck, 1992)

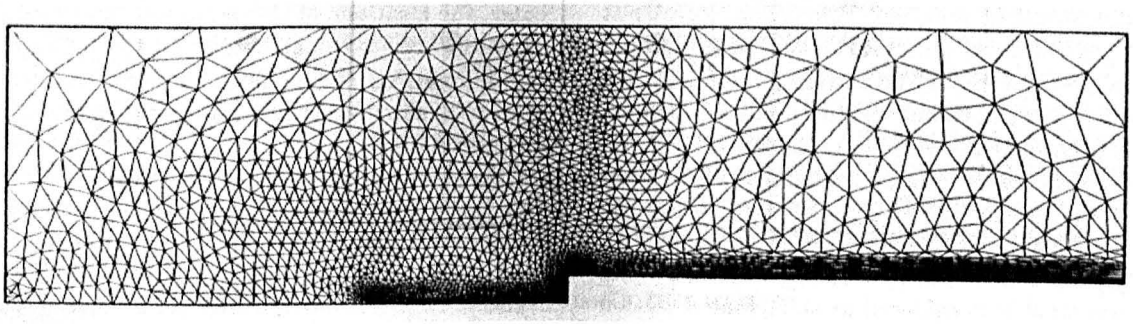

Figure 3.3. Unstructured grid. (From Vilsmeier and Hänel. 1992)

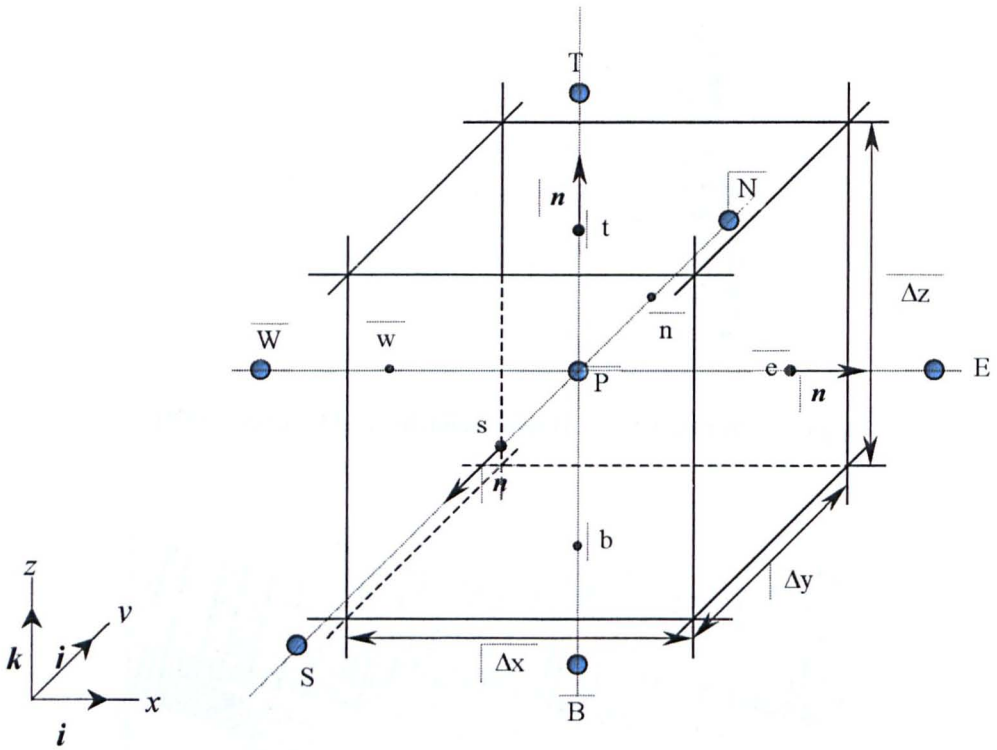

Figure 3.4. Control volume for a three dimensional grid.

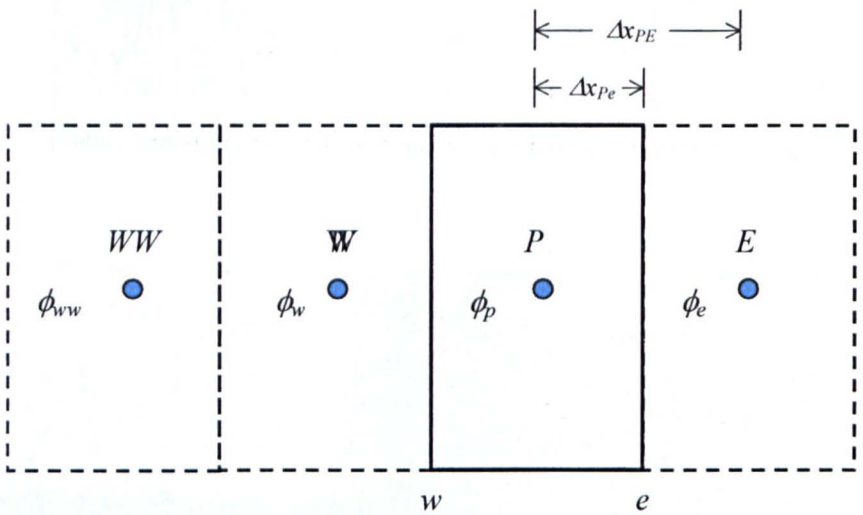

Figure 3.5. Control volume notation.

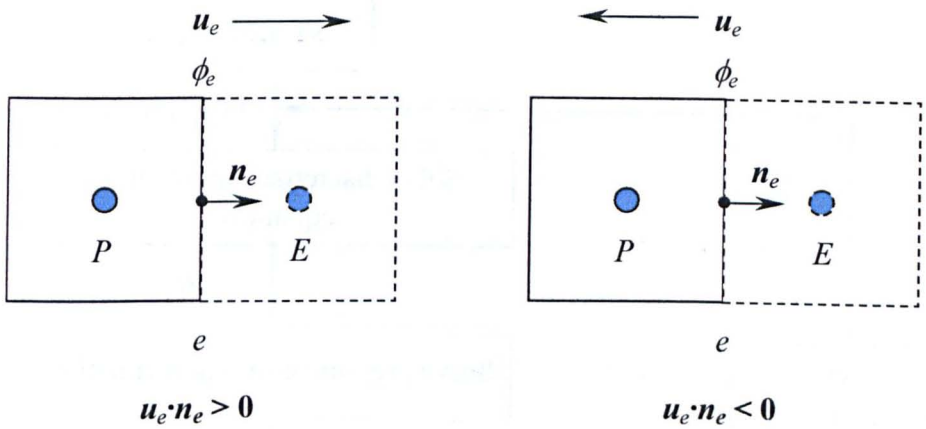

Figure 3.6. Approximation of ϕ_e using the upwind differencing scheme.

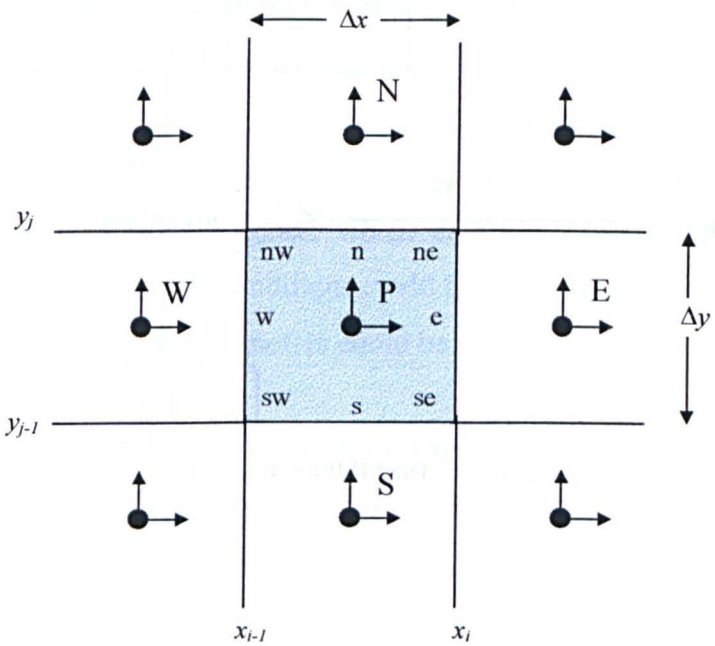

Figure 3.7. Colocated arrangement of velocity components and pressure on a finite volume grid.

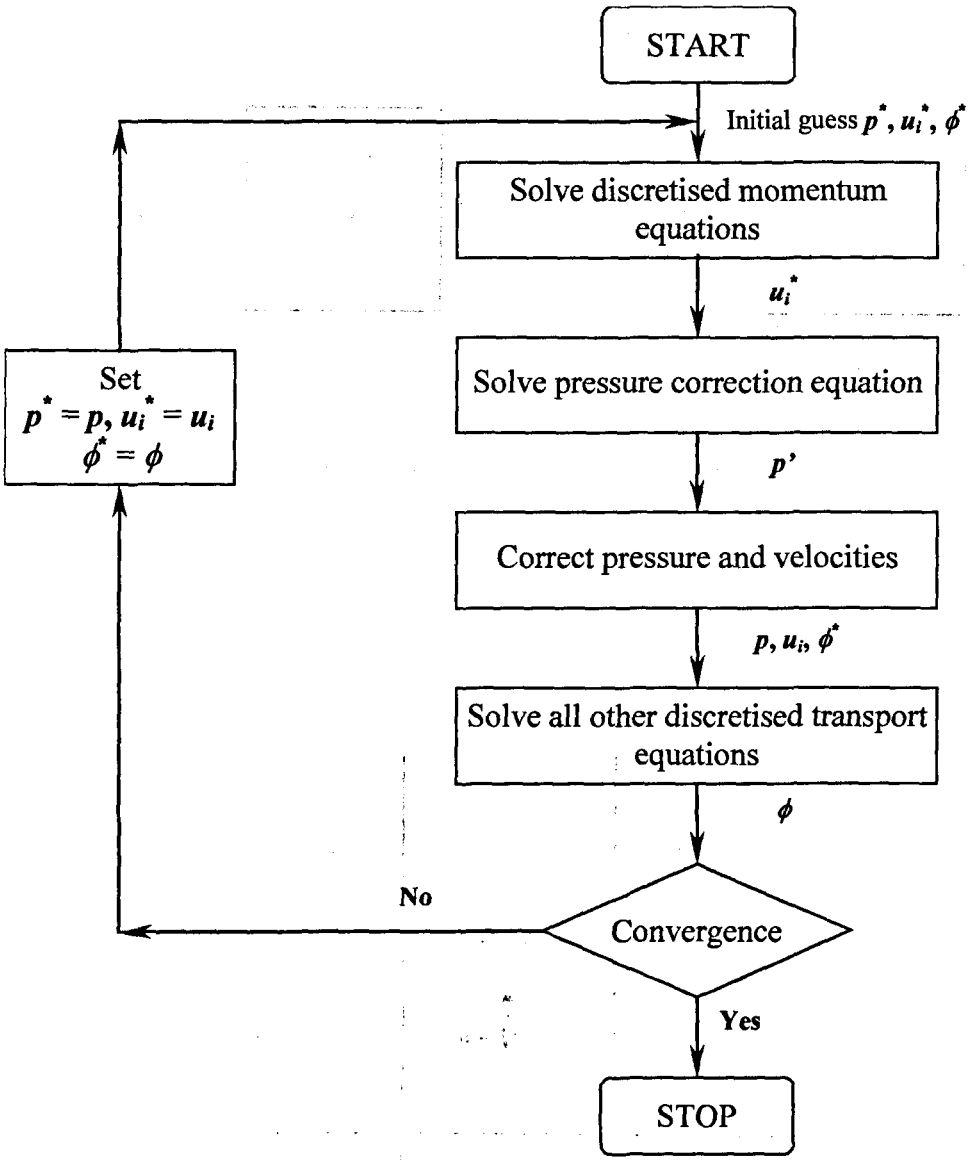

Figure 3.8. The SIMPLE algorithm.

4 EXPERIMENTAL DEVICES AND PROCEDURES

4.1 Introduction.

This chapter describes the experiments and measurement techniques used in the field and laboratory work. Also provides the objectives of these experiments. The chapter is divided in two main parts:

- Experiments and measurements done for buoyancy affected flow.
- Experiments and measurements done for porosity affected flows.

4.2 Buoyancy affected flows.

The work on buoyancy affected flows was divided in two phases. The first one covered the field measurements *in situ* and the numeric simulation of the industrial case. During this phase, some interesting problems arose that could not be satisfactorily explained by the literature on the subject. Also, doubts about the ability of numerical simulation to replicate the natural phenomena compelled us to obtain experimental data. Thus it was decided to undertake a second phase, which comprised the design of a laboratory experiment where the boundary conditions could be controlled and simple mathematical relations to calculate relevant parameters could be obtained.

4.2.1 Field measurements on an industrial site.

British Aerospace (BAe) operates large hangars where much of the work occurs at ground level. BAe is interested in provide heating to just the areas occupied by their staff. At the moment the air conditioning system installed consist of heaters that force hot air from the top of the hangar. However, buoyancy tends to force the warm air towards the ceiling, leaving the workers in cold draughts or causing additional heating.

The experimental programme was undertaken to estimate the boundary conditions for the CFD calculations and to aid validation of the CFD predictions. Four different tests were conducted while BAe's Building Energy Management Systems (BEMS) was in

use. Because the hangar was in operation during the tests the measurement techniques had to satisfy BAe's safety requirements. Thus, the equipment used at catwalk level was secured in order to avoid it falling onto aircraft or workers.

The BAe building is sited at Filton approximately 7.5km north of Bristol. It was constructed in 1946, of steel frame with sheet cladding, and consists of three bays, West, Centre and East; Figure 4.1 shows a panoramic view of the hangars. The experimental work was undertaken in the last one.

The East bay or hangar is 35m high, 105m long, and 85m wide. The whole of the south facade is occupied by a folding esavian door which is 26m high and consist of two sections, each movable from either end. The north end of the hangar is occupied by two stories of office accommodation as in Figure 4.2. In 1985, the roof was modified and now consists of a steel sheet-plastic foam sandwich construction, with a resin based outer coating and is provided with lines of glazing running N to S and fitted with double-glazed plastic units (Dane G.E. 1991).

As mentioned, the hangar has 10 direct gas fired heaters installed at a height of 23m from the floor. Six of these can be used to introduce fresh air or recirculate it: four located at the south wall and two at the north wall. The remaining four recycle the air inside the edifice and are located in the central zone of the building. To extract paint fumes BAe has installed three outlets near the East wall of the hangar (Day B. 1990). When these are operated, units H1 to H4 and H9 and H10 for east bay switch to fresh air as do the units in the centre and west bay. Units H6 and H8 are interlocked off to prevent the risk of fire (see Figure 4.2 for location of these units).

4.2.1.1 Test 1. Point temperature logging.

This test was conducted to identify the temperature distribution throughout the hangar, under normal operating conditions. The temperature measurements were taken using a rope with 31 T-type thermocouples tied at different intervals.

The first top 10 thermocouples had 1m spacing and the last 21 had 0.5m spacing. The last thermocouple was at a height of two meters above the floor so as not to interfere with the workers at ground level as reported in previous work (Day B. 1990). However, measurements taken at floor level, using a contact thermocouple, showed the temperature difference between the floor and the last thermocouple was only about 0.5°C.

All temperatures were continuously logged by connecting the thermocouples to a Data Acquisition System, model IIE-770, which in turn was connected to a portable computer. The measurements were taken at 20 locations (P1 - P20) inside the hangar, as shown in Figure 4.3. The temperatures were measured for each thermocouple every 5s over a 120s period. The values reported here are the average over the 120secs taken by each thermocouple at each location. The average time to take measurements between each point, allowing for saving data and moving equipment, was 13min.

4.2.1.2 Test 2. Continuos temperature logging.

This test was used to monitor temperature variations in the hangar with time, at a single point. Point 4 was chosen as it is located between two of the gas fired heaters and was the least likely to be moved as a result of the ongoing work below. This was reported to have been a major problem in the previous work undertaken in the hangar (Day B. 1990).

4.2.1.3 Test 3. Boundary conditions.

The boundary conditions were established by taking various temperature and velocity measurements.

The inlet conditions were measured using a hot wire anemometer and a type K thermocouple. The outlets conditions were measured with the extraction system on and off.

The infiltration through the esavian doors and between the hangars was estimated by taking air velocity and temperature measurements at various heights and locations and averaging the results.

The wall, floor and roof temperatures were measured using an infrared temperature-sensing thermometer. The outside temperature was recorded by the BEMS.

4.2.1.4 Test 4. Jet penetration.

In order to estimate the jet penetration light plastic strips were used to indicate flow patterns and direction. The velocities and the temperatures were also measured at different heights with the aid of a moveable platform. Also, some smoke tracing experiments were undertaken to visualise the flow, and smoke movement was videoed.

4.2.2 Laboratory experiments.

The field measurements showed that it was important to known the maximum penetration of the hot jets used in the hangar. The literature survey showed that there is a lack of experimental work on jet penetration on a stratified field. Although the work done by Ogino *et al.* (1980) considered stratification, their experiments differs from the characteristics that the hangar presents. Their experiments were designed as an open chamber. In Figure 4.4.A., the surface of the fluid is free to increase at the rate of injection of the dense fluid, ρ_f, and the front of the mixed fluid and the density structure above it are evolving in an environment which is moving downwards at this mean rate (Baines *et al.*, 1990). In Figure 4.4.B., although the stratified environment causes an horizontal spreading of the flow near the maximum penetration height, the incoming fluid falls back mixing with the lower layers and, eventually, filling the tank. In the hangar the inflow and outflow are both behind the front. This case leads to the formation of a sharp interface between the injected and the original fluid, located at the top of the fountain (Baines *et al.*, 1993). We must recall that in the hangar, hot air is injected from the top and an outflow region exists at the same level. This case is quite different from that where the fluid is allowed to flow from the bottom, as already pointed out. Thus, it was decided to perform an experimental program. A set of ten experiments were undertaken in the laboratory. The objectives of the experimental work are:

- To obtain a mathematical expression to calculate the jet penetration on a stratified environment.
- To study and identify the parameters that control the unstable layer developed once a steady state condition has been achieved.

4.2.2.1 Dimensional analysis.

Before proceeding to a description of the experimental set-up and the measurement systems, the basic considerations underlying the design of the experiment will be outlined. For this purpose, the governing equations for the flow may be considered to yield the dimensionless parameters appropriate for presenting the experimental data in generalised terms.

Dimensional analysis is a method for reducing the number and complexity of experimental variables that affect a given physical phenomenon, by using a compacting

technique. Its main purpose is to reduce variables and group them in dimensionless form. One of the advantages of this approach is that provides scaling laws which can convert data from dimensionally small systems to large systems. The main disadvantage of dimensional analysis is that although its application is very successful when the system can be described by one or two parameters, when the system is complex, i.e. described by many parameters, its application is ruled out.

For self consistency, the dimensional analysis is presented because the experimental results of the present work are going to be compared with relations developed by others.

Consider a source of hot fluid injected with downward momentum into and stratified environment, which could be considered infinite in the horizontal dimension. If the source is small compared with the height of the resulting fountain the flow will depend only on the fluxes of volume, Q_o, momentum, M_o, and buoyancy, B_o, defined as follows:

$$Q_o = \pi r_o^2 W_o \qquad 4.1$$

$$M_o = \pi r_o^2 W_o^2 \qquad 4.2$$

$$B_o = \pi r_o^2 W_o g\beta\Delta T \qquad 4.3$$

Where W_o is the mean velocity at the source, r_o the inlet radius, and ΔT is the characteristic temperature difference, which have been chosen as $\Delta T = T_j - T_z$, where T_j and $T_{z\infty}$ are the inlet and is the ambient temperature, respectively.

Using 4.1 we can rewrite 4.2 and 4.3 as

$$M_o = \frac{Q_o^2}{\pi r_o^2} \qquad 4.4$$

$$B_0 = g\beta\Delta T Q_o \qquad 4.5$$

As show by Turner (1966) the height of the fountain is defined by dimensional analysis as:

$$Z_m = C_m M_o^{3/4} B_o^{-1/2} \qquad 4.6$$

In 4.6, C_m is a constant obtained experimentally. Now, we use the definition of the Froude number

$$Fr = \frac{W_o^2}{g\beta\Delta T r_o} \qquad 4.7$$

Taking the square root of 4.7 and using 4.1, we can write

$$Fr^{1/2} = \frac{Q_o}{(g\beta\Delta T r_o)^{1/2}\pi r_o^2} \qquad 4.8$$

Using 4.2 and 4.3 we can put Z_m as a function of $Fr^{1/2}$

$$Z_m = C_m \pi^{1/4} r_o Fr^{1/2} \qquad 4.9$$

Where C_m is a constant that must be determined by experiments.

4.2.2.2 Experimental tank and measurement equipment.

The jet penetration experiments were undertaken in a perspex box using water as the working fluid. With the help of Figure 4.5 we will describe the functioning of the system. The water is heated in tank 1. The water is transferred to the experimental tank, 6, using a centrifugal pump, 2. The excess of water is diverted towards tank 1 by means of valve 3. The volume flow into the experimental tank is measured using rotameter 4. The water leave tank 6 through outlets, 7. The volume leaving the tank is measured by rotameter 8.

The rotameters are manufactured by KDG MOBREY LTD and correspond to the series 2000, which are variable area flowmeters. The tubes are made from borosilicate glass; the maximum working temperature is 100°C. The floats are plumb-bob type. In order to cover the whole range of mass flow used in the experiments two tube sizes and two float sizes are used, Table 4.1.

The experimental tank, Figure 4.6, is made of four transparent perspex sheets of 12mm thick each, so that it would be possible to observe the flow. The sheets are joined by stainless steel screws and were glued to avoid possible leakage. A silicon gasket is placed at the top and bottom of the tank where the high and low temperature baths are joined to the tank to achieve water- tightness.

A high temperature bath has been installed on top of the experimental tank. A tank with an electrical heater controlled by a variac maintains the desired temperature in the high temperature bath, Figure 4.7. A mechanical refrigeration system is used to reduce the temperature of the water that is pumped into the low temperature bath located at the bottom of the experimental tank. The pipe is made of copper 22mm of diameter and insulated with CLIMAFLEX.

The high and low temperature baths are both made of aluminium, have the same dimensions, and are divided into departments to obtain a better circulation of the water,

Figure 4.8. In particular, the high temperature bath has three orifices to permit tubes to pass through the bath and penetrate into the experimental tank. The orifice at the back (I) introduces a thermocouple frame. The orifice situated at the left side (II) has a float to assess the level on the rest of the tubes. The orifice at the front (III) helps to drain the air trapped as bubbles when the experimental tank is filled with water. Finally, the jet is located at the centre of the tank (IV).

Three different jet diameters were used in the experiments: 1, 0.5 and 0.25cm, Figure 4.9. The jets were introduced through orifice I. The jet have 'o' ring seals to prevent leaks.

A movable frame with thermocouples is used to measure temperature inside of the tank. The frame of has 18 'T' type thermocouples. Seventeen of them are located along the frame with a distance between them of 3cm; the last one is located at the back of the frame 16cm from the centre of the tank. The frame could be moved to any level inside of the tank by mean of a system of pulleys, Figure 4.10.

The thermocouples are connected to a data acquisition system and this through RS232 cable to a computer. The scanning rate for the 18 thermocouples channels is 1ms. Therefore, at the mentioned rate, the time lapse to take all the 18 thermocouples channels is 0.25s. Also, there are two thermocouples in the top of tank and two at the bottom of the tank. Furthermore, thermocouples have been set at the entrance of the jet and at inlet and outlet of the high and low temperature bath, respectively. The diameter of the insulated thermocouple cable is 1.1mm. All the thermocouples were calibrated using a constant temperature bath. Finally, the tip of all thermocouples were insulated with a thin layer (~0.35mm) of non-corrosive silicon.

The flow was visualised with ink. All the visualisation tests were filmed with a Panasonic video camera model PN-ST558. The recording speed of the camera is 25 frames per second. The tank was illuminated using ten 50W lamps. The lamps were installed over one side of the tank and were kept on for no more than 5min during to avoid the heating of the tank A white cover was located at the back of the tank to diffuse the light evenly over the whole space of the tank.

4.2.2.3 Experimental procedure.

All the experiments followed a three-step method. The first step was to impose a stable thermal stratified field on the tank. The tank achieved a stable stratification typically

after 72h. The temperature profile was measured each 8h and it was considered that a steady state was achieved when the difference between two consecutive measured profiles were less than 0.5°C on average. Meanwhile, the water in the jet circuit was been heated in order to have it ready for the next step.

The second step was to open valves 10 and 11 depicted in Figure 4.5. The jet was left open 12h after which a first temperature profile was taken. Again, temperature profiles were taken until the difference between two consecutive temperature profiles and the measured jet penetration was 1% approximately.

Finally, ink was introduced through the porthole at the top to the entrance of the jet. The results were videoed.

4.3 Porosity affected flows.

Nestlé is interested in improving the operation of ventilated rooms which are used to modify the properties of one of his products; specifically, the Nestlé storeroom in York. Nestlé bake their own biscuits and then store them for periods of eight to ten days before using them to produce the final chocolate biscuit. The main purpose of the storeroom is to correct and stabilise the moisture content of the product before the final chocolate coating/moulding. The individual biscuit layers have already been sandwiched with fat cream and formed into wafers. It is these wafers which are placed in the store or maturing room.

This particular product can be characterised as multi-domain food. In this type of food, moisture migration from one food component to another will continuously occur in order to reach thermodynamic equilibrium with the surrounding food components and the environment. Labuza and Hyman (1998) have pointed out that two factors affecting moisture migration in this type of food are water activity equilibrium (thermodynamics) and factors affecting the diffusion rate (dynamics of mass transfer).

Nestlé has a moisture content target for the product at the end of the maturation period. If the moisture content of the product is too low then after coating with chocolate the biscuit attracts moisture from the chocolate coating causing it to crack. At the moment, there is inconsistency of the moisture content of the products leaving the room.

The operation of the room made it difficult to perform experiments within it. By carrying out some simple experiments and using CFD as an exploratory tool for different scenarios the present work suggested possible room arrangements which should lead to an improvement of the speed to satisfactory maturation and better uniformity of product quality.

The experimental techniques satisfied Nestlé's safety requirements. All due care was taken when working on the room so neither the workers safety nor the product integrity were placed at risk.

4.3.1 Field measurements on industrial site.

The product storeroom is located in York and it is 6.12m high, 36m long and 31m wide, as shown in Figure 4.11. The room has three entrances which are orientated to the north, east and west, respectively; and it is divided in five sections, each storing either two or

four finger products. Figure 4.12 show a photograph of the storeroom, the main entrance is at the back of the photography.

The ventilation system consists of twelve inlets 46cm long by 45cm wide, eleven of them are aligned in the centre of the room's ceiling orientated toward the north and separated by a pitch of 2.98m; one of the inlets is locate off-line, as can be noted in Figure 4.13. Also, there are twelve outlets, six of them located at the east wall while the other six are in the west wall. 45.4% of the air that is used in the room is fresh air, which introduced through the system from previously filtered ambient air. 54.6% of the air in the ventilation system is recycled air.

The wafers are stored in three 1.61m tall stacks each separated by a gap of 30cm. Each group of stacks is separated by a gap of approximately 24.21cm, as show in Figure 4.14.

Each stack has 13 trays where with a capacity of 6 wafer books. Depending on the type of product the gap between the trays could be 5mm or 25mm, Figure 4.15. In the first case the space allowed for air circulation is restrained by a factor of 5 with respect of the former, promoting short-circuiting in the ventilation system. The later can be appreciated in Figure 4.16.

4.3.1.1 Point temperature logging.

The temperature distribution along the centre of the maturing room was measured using an array of 13 type T thermocouples (copper-constatan) connected directly to a data acquisition system, Figure 4.17.

The thermocouples were attached to a rope at 0.5m intervals covering the heigth of the room. Then measurements were done over the 12 inlets.

The data acquisition took measurements during 2 minutes each 5 seconds in each experimental spot, in order to take the average of the temperature measurements in each spot.

4.3.1.2 Continuos temperature logging.

This test was used to monitor temperature variations in the storeroom with time, at two different points, Figure 4.18.

The temperature was logged intervals of 10 minutes during two weeks in each experimental position. The loggers were located approximately at a height of 1.7m from the floor.

4.3.1.3 Velocity measurements.

Measurements with airflow probes underneath each air-inlet (to quantify airflow velocity). A funnel with a known area was used to estimate the air velocity at the inlets, Figure 4.19.

Airflow measurements were performed under selected air-outlets. It was not possible to reach all the outlets because of the presence the wafer stacks. However, measurements were undertaken at the position of the damper, Figure 4.20.

Flow measurements have been taken at three separate locations in the ancillary ductwork, Figure 4.21. At each of these locations the velocity distribution was measured using a hot wire anemometer. The measurements have been used to build confidence in the boundary conditions imposed on the CFD calculations and to validate CFD itself.

In order to visualise airflow patterns under each air-inlet dry ice was used. This tracer was used to avoid any contamination risk to the products. It should be notice that dry ice vapour has a negative buoyancy and thus will tend to 'drop', unless forced convection very strong. Only spot measurements were carried out. For convenience reasons the dry ice used was stored in a stainless steel vessel. An electric lift vehicle was used to reach the ceiling. Factory employees operated the vehicle and assisted with the video. Another person held a bowl of water under the air-inlet and dropped a pellet of dry ice into it. This generated visible vapour, which outlined the airflow pattern. As additional lighting was necessary, a standard (240V) power supply standard introduced in room to ensure a high quality video of the vapour pattern.

Finally, spot measurements air velocities were undertaken at 15 horizontal positions within the room. At each position measurements were taken at height of 0.5, 1.0 and 1.5m, approximately.

4.3.1.4 Moisture measurements in maturing room.

Humidity measurements were taken near the inlet and at a height of 1m from the floor directly below the same inlet.

Silicagel bags in tray arrangements were used to monitor the moisture take up at different horizontal and vertical positions within the room. Silicagel was chosen because its hygroscopic properties will exaggerate the moisture take up. Silicagel is a partially dehydrated polymeric form of colloidal silicic acid with the formula $SiO_2 \cdot nH_2O$. Silicagel tends to be used for drying applications in which capacity is required at low and moderate water vapour pressures (Crittenden and Thomas, 1998). Additional experiments under controlled conditions in cabinets were carried out in order to obtain the saturation time of silicagel.

The silicagel in the trays were contained in porous (non-airtight) bags to avoid contact with the wafer books placed in the room. The silicagel used in the experiment was mixed to ensure that the entire batch has the same characteristics at the start. The trays were clearly labelled and the moisture take up of each bag was monitored. A total of 25 trays were used and located at 5 different locations inside the room and at 5 different vertical positions with tray arrangement I, Figure 4.22. Additional experiments with silicagel were undertaken in two different positions with a new tray arrangement as is shown in the figure previously mentioned.

Figure 4.23 shows the location of the silicagel bags. The number in the square represents the row; full line squares represent arrangement I and interrupted line squares arrangement II. The number at the top right corner of the locations represents the number of days that the arrangement was kept inside the room, and the numbering of the rows is in italics.

Finally, some data for moisture uptake for wafers in the room was collected. The method consisted in taken one wafer from the centre of a tray previously marked. Similarly as with the silicagel bags, the time that these trays stayed in the room was determined by the operation of the room.

4.3.2 Laboratory experiments.

4.3.2.1 Wafer in cabinets.

The aim of this work was to analyse the effect of the packing technique on moisture take up and to establish by experimental methods the functional form of the moisture take up of the wafer under different conditions. Table 4.2 summarises the different wafer arrangements and packing techniques that were used. The moisture take up of

wafer trays was measured under controlled steady state conditions in a single cabinet model FE 6110H/S/R-D-DP-IND constructed by Gallenkamp Industrial. All the experiments were carried out at a temperature of 20°C with and averaged velocity and the inlets of 2m/s.

Figure 4.24 shows the arrangement of a well packed and a badly packed tray. The former is arranged in a way that reduces the space for the air to flow. Also, the gap in the four finger stacks is almost 5 times less than that present in the two finger trays, increasing the air resistance to flow through the wafers.

Additional experiments under controlled conditions in stacks of three trays with 4 Finger wafers were undertaken. The stack was placed on top of an analytical balance. Two different flow conditions: 2.5 and 0.5m/s were tested. These experiments where not undertaken in the cabinets but in the laboratory and the velocity reported is that measured coming from the trays as shown in Figure 4.25. The ambient relative humidity was monitored resulting in an averaged value of 35%. The temperature of the room was 24°C approximately.

Finally, cabinet experiments were carried out to characterise the effectiveness of silica gel bags as moisture sinks. The weight of bags with silicagel was monitored as a function of time after insertion into the cabinet.

Figure 4.1. Panoramic view of BAe's hangars.

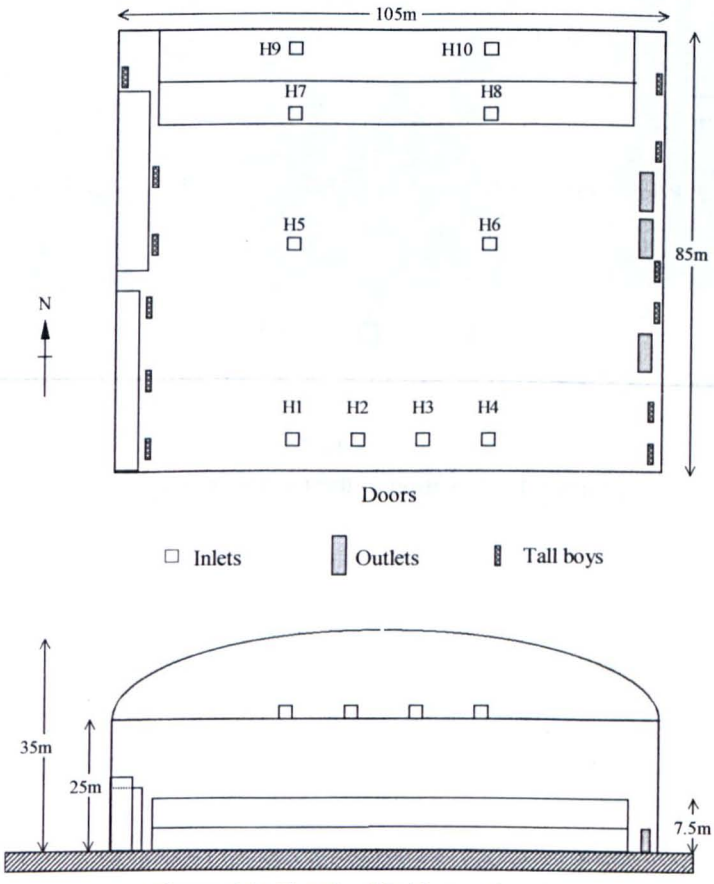

Figure 4.2. Sketch of BA's east hangar.

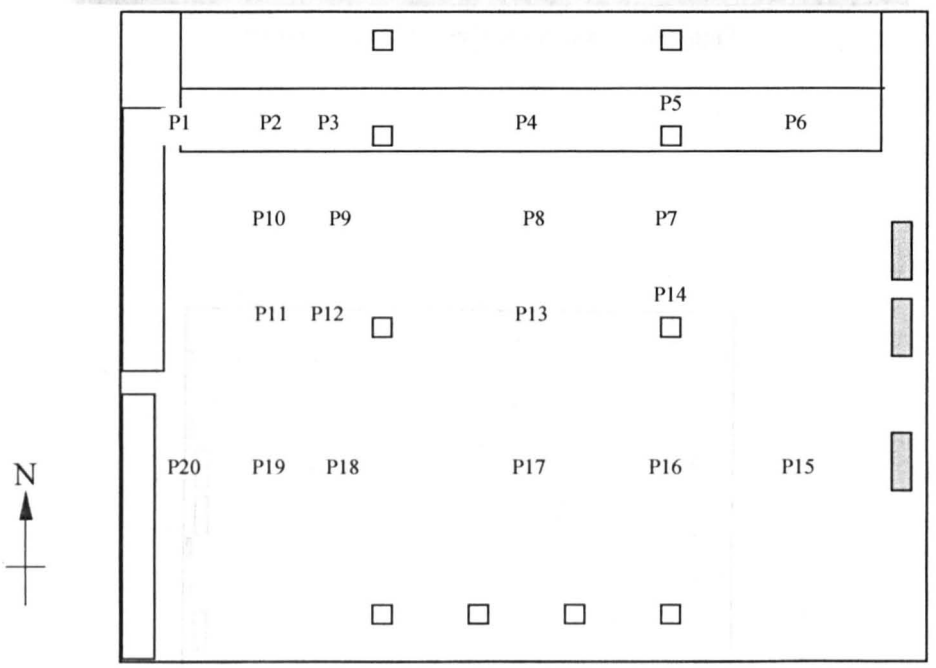

Figure 4.3. Location of thermocouples trees.

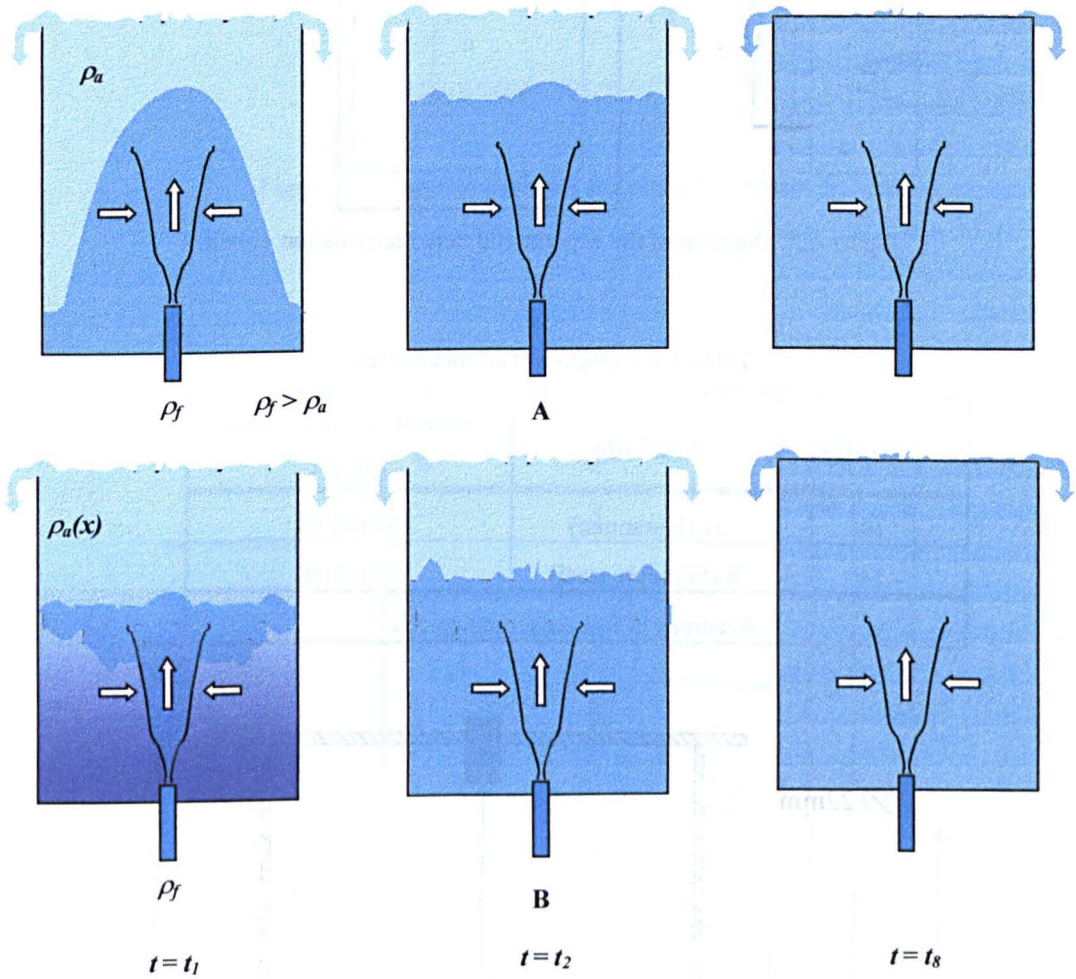

Figure 4.4. Turbulent fountain in an open chamber. A) Baines *et al.* (1990). B) Ogino *et al.* (1980).

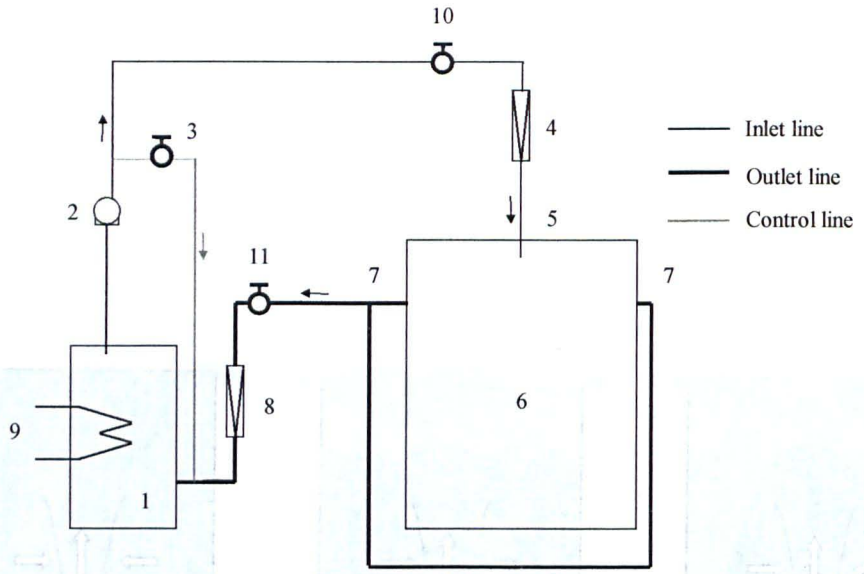

Figure 4.5. Diagram of the experimetal tank recirculation circuit.

Table 4.1. Component of rotamenters.

Tube size	Float size	Mass flow range, l/min (20°C)
10	K (Korannite)	0.10-0.98
14	S (Stainless steel)	0.50-5.50
Accuracy at full scale reading 5%		

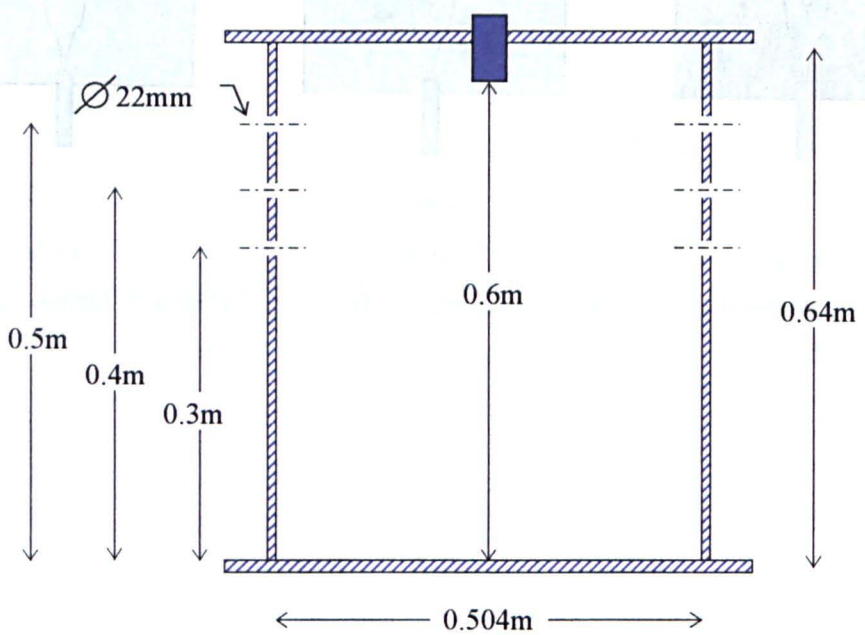

Figure 4.6. Dimensions of the experimental tank.

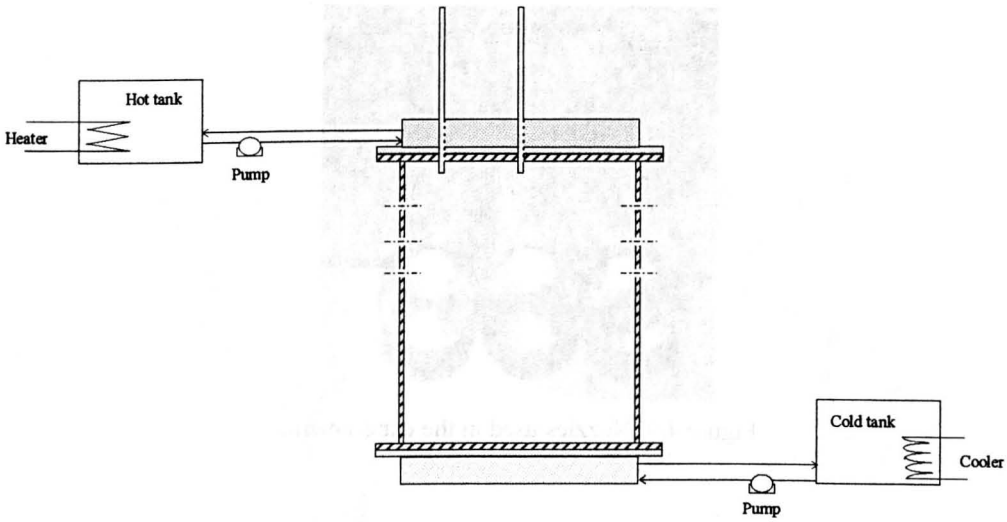

Figure 4.7. Experimental tank hot and cold circuits.

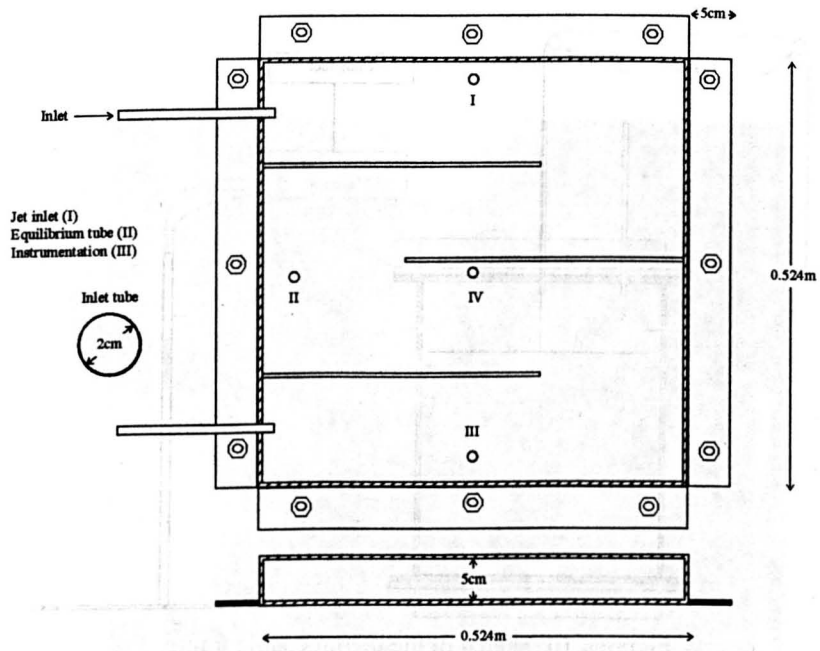

Figure 4.8. Drawing of the hot bath.

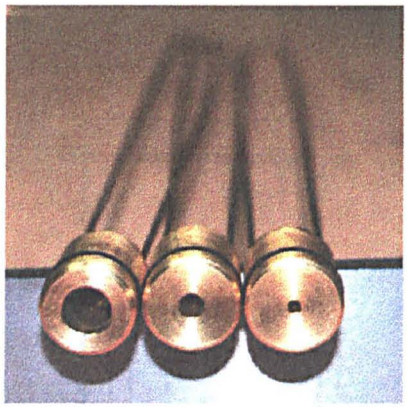

Figure 4.9. Nozzles used in the experiments.

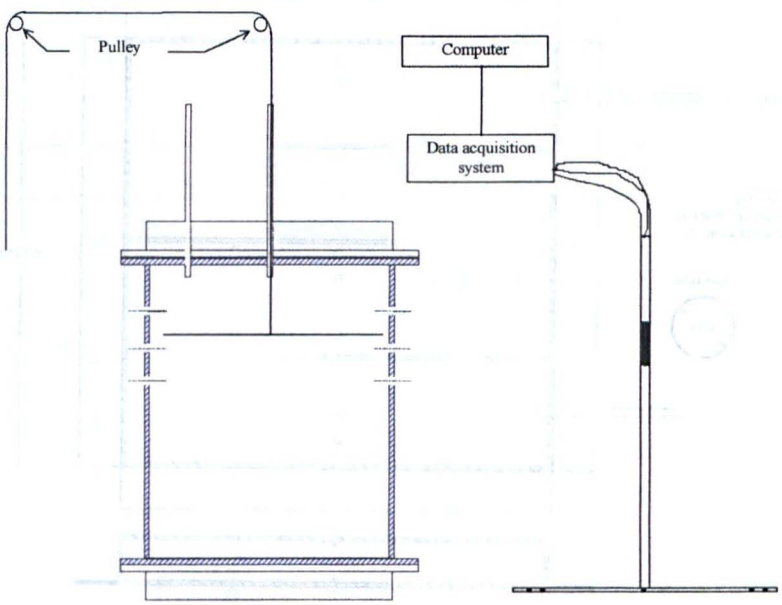

Figure 4.10. Sketch of the thermocouple frame.

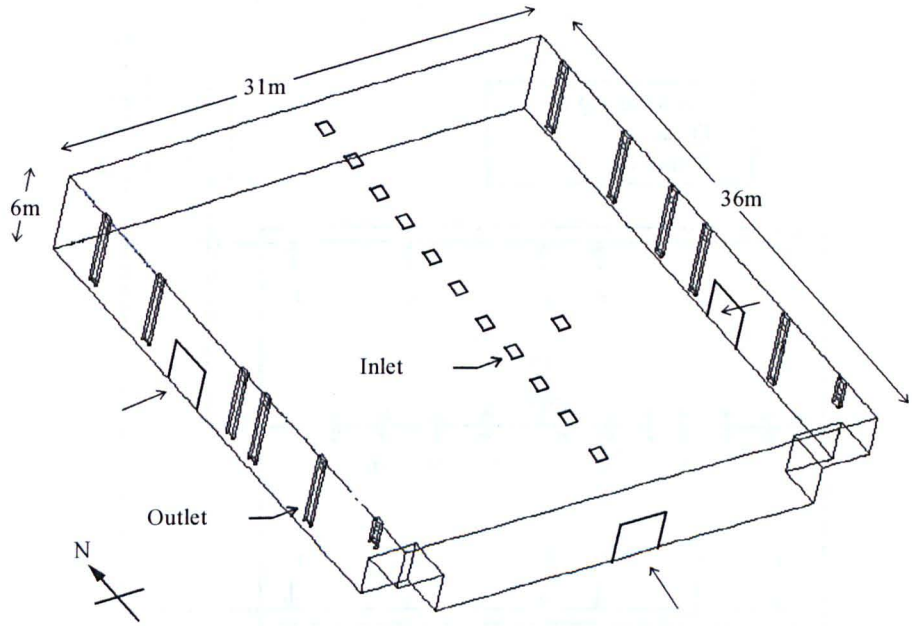

Figure 4.11. Sketch of the maturing room.

Figure 4.12. View of the maturing room.

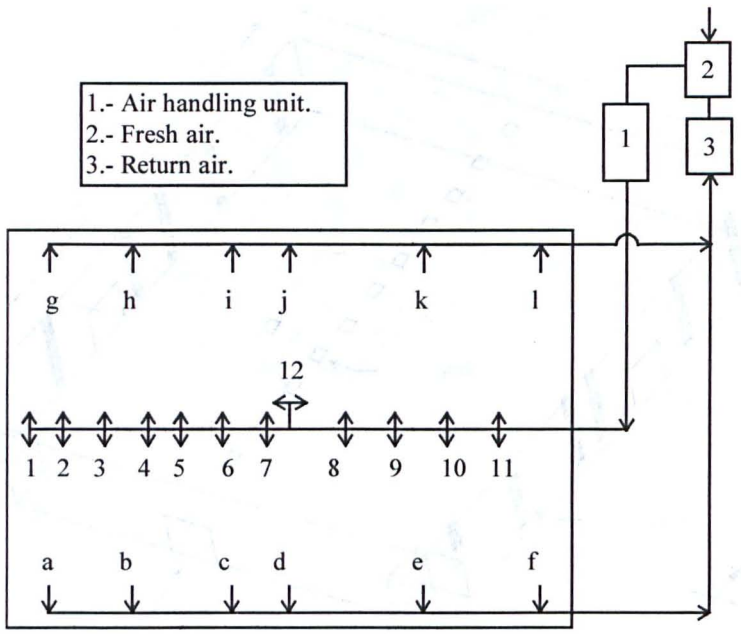

Figure 4.13. Sketch of the ventilation system.

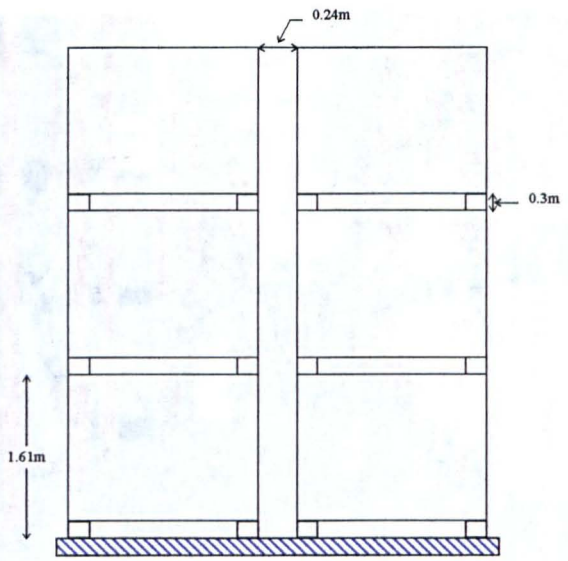

Figure 4.14. Stack and array arrangement.

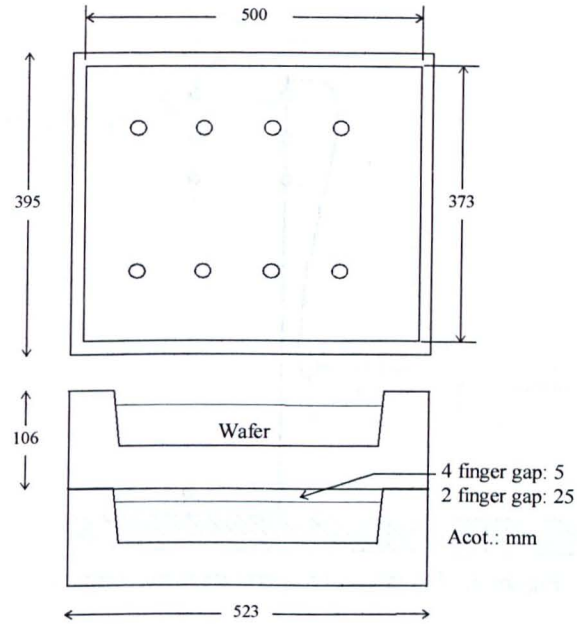

Figure 4.15. Dimensions of the wafer tray.

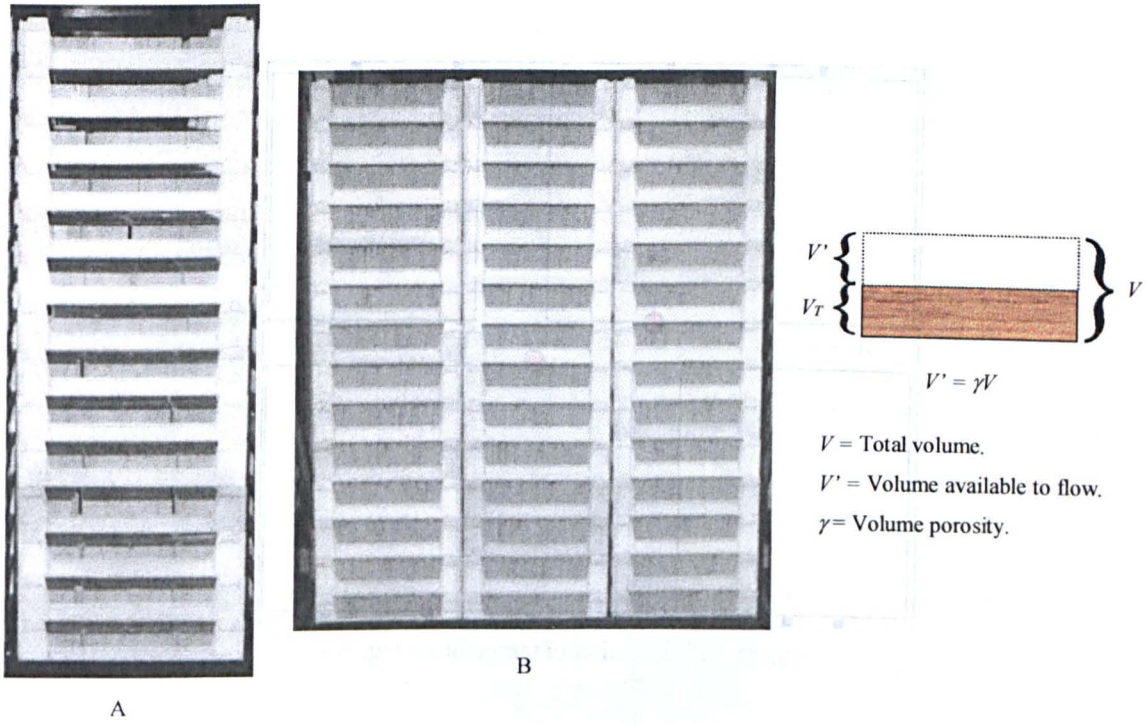

Figure 4.16. The product inside of the storeroom. A) High porosity arrangement. B) Low porosity arrangement.

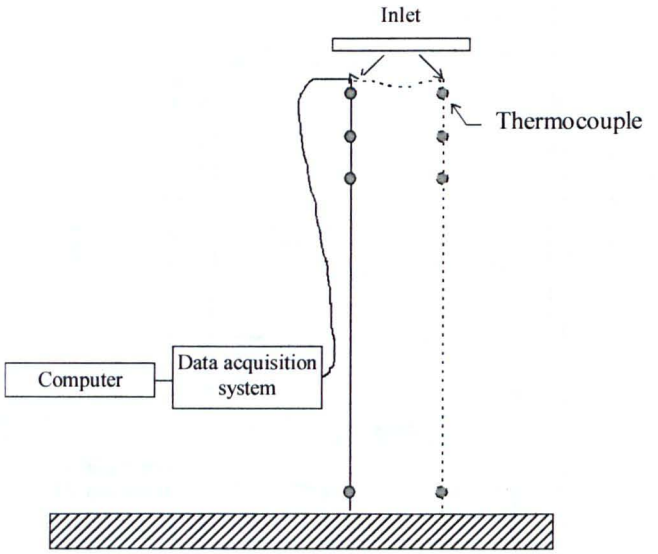

Figure 4.17. Vertical temperature measurement.

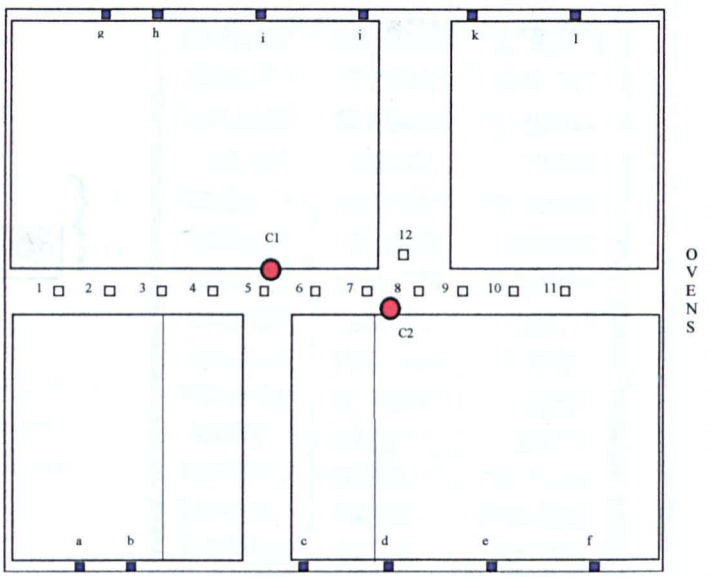

Figure 4.18. Location of temperature loggers.

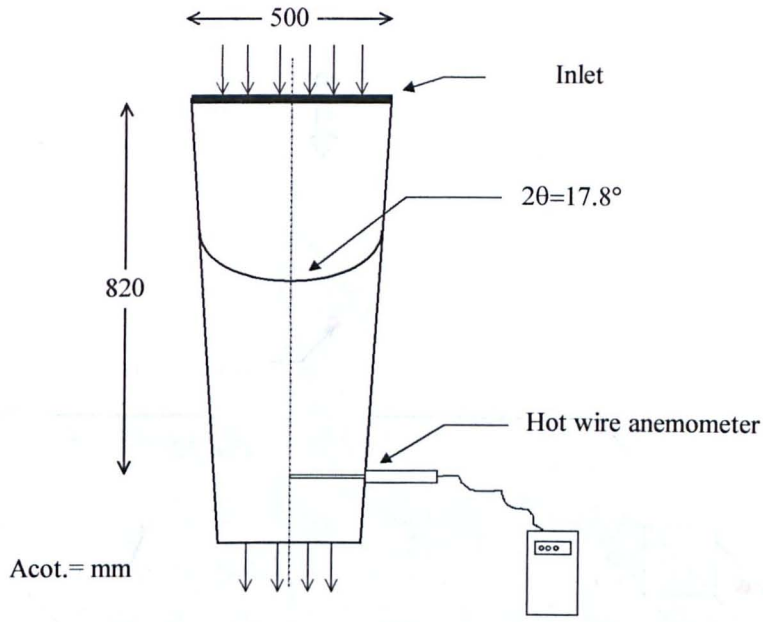

Figure 4.19. Sketch of the funnel used to measure velocity at the inlets.

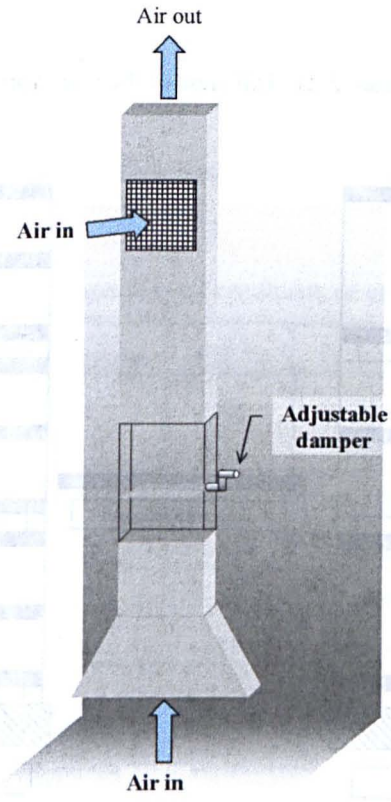

Figure 4.20. Sketch of the outlets.

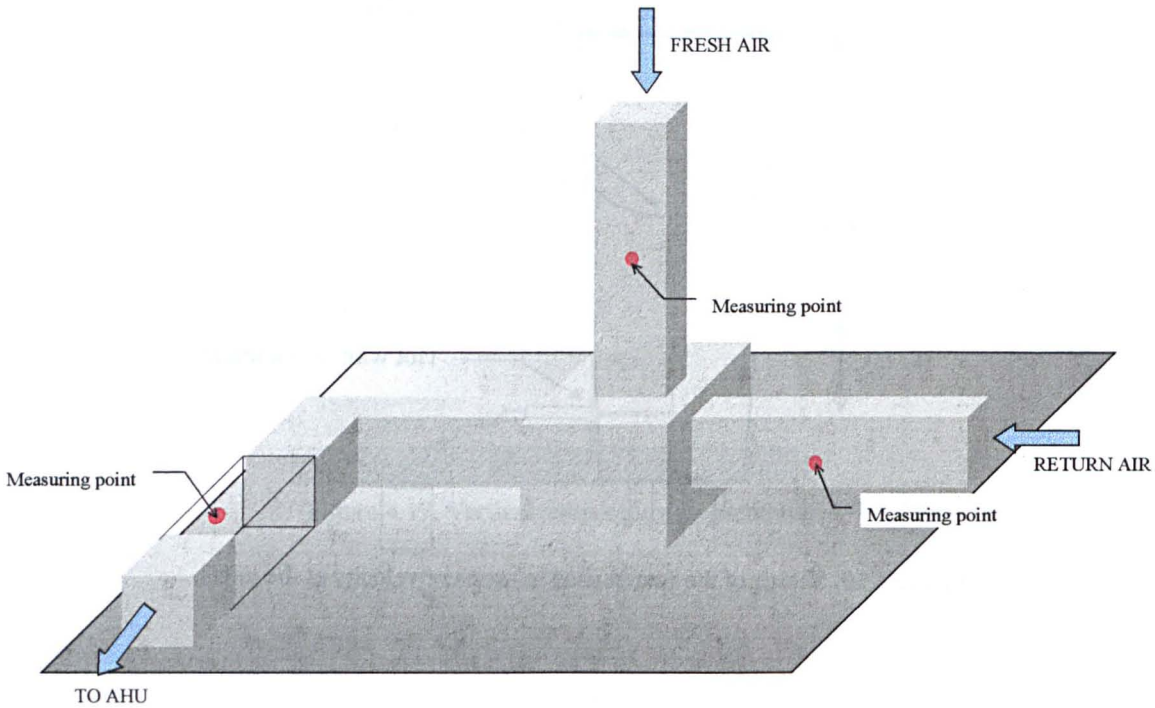

Figure 4.21. Top view of the duct work.

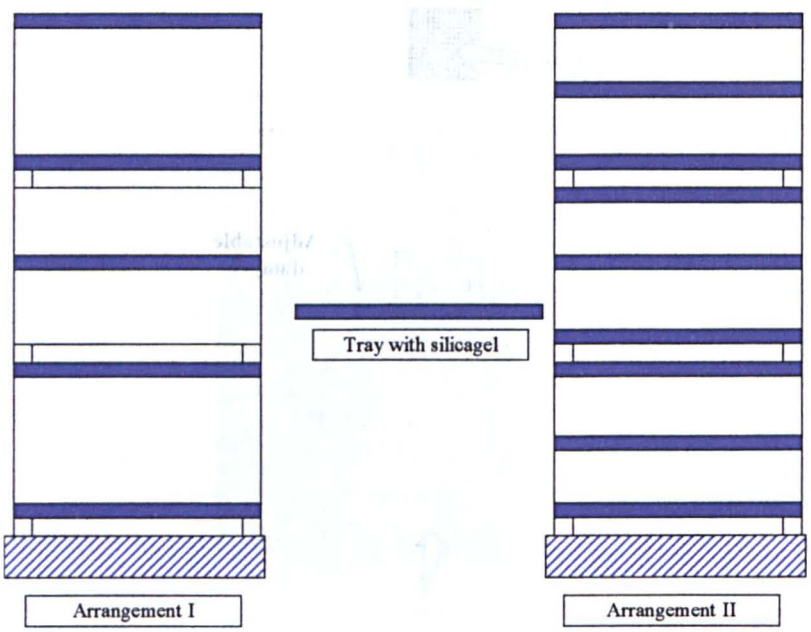

Figure 4.22. Vertical position of silicagel bags.

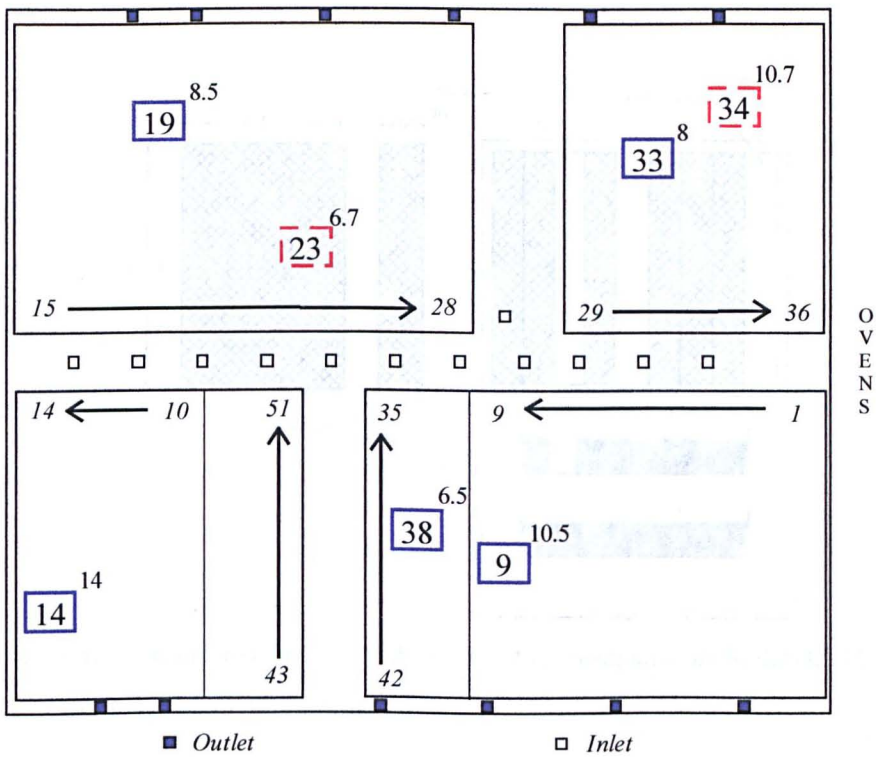

Figure 4.23. Location of stacks with silicagel bags.

Table 4.2. Experimental conditions on cabinets.

Wafer arrangement	RH, %	Packing technique
2 Finger	50	Well packed
	50	Badly packed
4 Finger	50	Well packed
	50	Badly packed
4 Finger	35	Well packed
	35	Badly packed

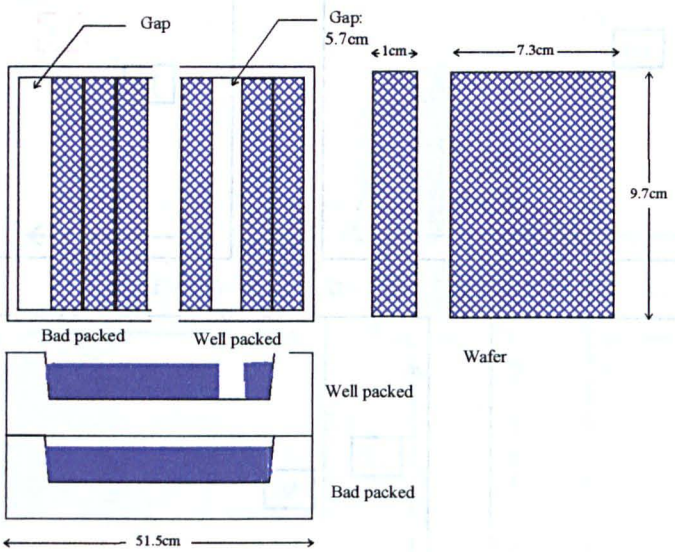

Figure 4.24. Sketch of the arrangement of wafer in the trays and four finger wafer dimensions.

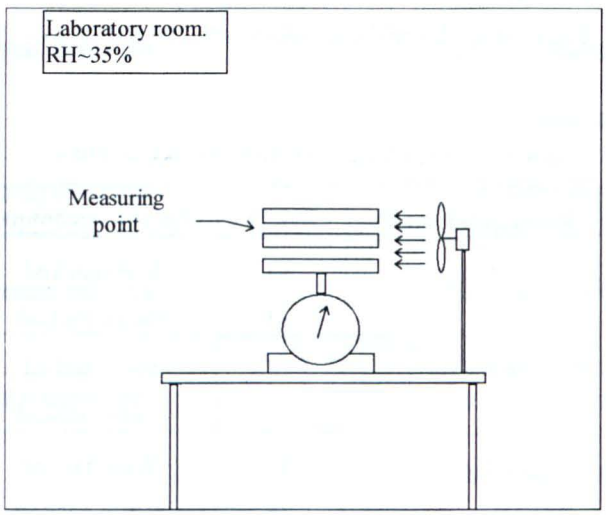

Figure 4.25. Nestlé experimental set up.

5 EXPERIMENTAL RESULTS

5.1 Introduction

This chapter describes the experimental and field measurements and divides naturally in two main parts:

- Field and laboratory work done in buoyancy affected flow.
- Field and laboratory work in porosity affected flows.

5.2 Buoyancy affected flows

This section present the information obtained by measurements made *in situ* in BAe's hangar and the data obtained in a set of 10 experiments done in the laboratory. As mentioned before, the laboratory experiments were designed to complement the work done in the hangar and to increase the confidence in the numerical work.

Others have extensively studied the penetration depth of a jet into an isothermal field and different algebraic equations have been produced to calculate it. However, most of the experimental work has been produced for open chambers.

The laboratory experiments attempts to obtain simple algebraic relations to calculate the penetration depth of a round jet into a thermal stratified field where the inflow and outflow are both behind the final penetration depth. The experimental results are compared with the data obtained in BAe's hangar.

The standard used for comparison for comfortable thermal environment is ISO Standard 7730, which has been recommended for industrial spaces with different levels of activity (Olesen and Zhivov, 1994).

5.2.1 Experimental results. Hangar.

5.2.1.1 Test 1

Point temperature logging tests were conducted on both the 6th February and the 19th 1998 March under different operating conditions.

- On February 6 the hangar conditions were:
- The fan of heater number 6 was working
- Average temperature 18.8°C
- Highest temperature 22.9°C, at the top of point 19
- Lowest 17.3°C, at the bottom of point 6.

A comparison of the vertical stratification in the hangar at different points (north and south) is presented in Figure 5.1 and Figure 5.2. These show similar trends and a point of inflection is observed at a height between 6 and 8m. Figure 5.1 shows another possible inflection point at a height between 16 and 18m, however this is less accentuated than that located at the lower height. Figure 5.3 is used to illustrate it by plotting the temperature and location as dimensionless variables, θ and z/H respectively, where z is the height of the measuring point and H the total height.:

$$\theta = \frac{\left(T(z) - T_c\right)}{\left(T(z = H/2) - T_c\right)}. \qquad 5.1$$

Where T_c is the temperature of the cold wall, in our case the floor. This definition of dimensionless temperature has been previously been used by Neymark, J. *et al* (1989).

Figure 5.3 shows that the linearity of the stratification is broken and is divided in two linearly stratified zones.

On 19th March the hangar conditions were:

- All heaters and fans are operating (except heater and fan number 1)
- Average temperature 20.3°C
- Values of the highest and lowest temperature were 23.7°C and 17.8°C, respectively.

From this data it can be seen that the temperature difference between the top and the bottom of the hangar increased by almost 40% from that recorded on February 6th.

The temperature profile at different points inside the hangar are presented in Figure 5.4 and Figure 5.5, from these it is possible to observe that there is a point of inflection at a height between 6 and 8m similar to that detected on February 6.

Figure 5.6 presents plots of the relative stratification for selected points. The stratification is less accentuated than that seen on February 6th and the same could be said about the break of the stratification profile. This behaviour could be due to the operation of the fans and heaters on March 19th, thereby promoting the mixing of the air inside the hangar and reducing the inflection of the stratification profile. However, it is not clear what is causing the break of the linearity of the stratification.

It is clear that thermal stratification exists in the hangar, where temperature variation gives rise to a density variation with height. A stratified medium could be in stable equilibrium or not. A medium would be in a stable stratification condition when a lighter fluid lies over a heavier one, since a restoring force arises if a fluid element is displaced vertically (Jaluria Y. 1980). This motion can overshoot the equilibrium position and oscillate about it; thus giving rise to internal waves (Turner J.S. 1973).

The fluid element will oscillate in a simple harmonic motion with angular frequency, N, which could be evaluated by means of the buoyancy frequency (Turner J.S. 1973):

$$N = \sqrt{g\beta \frac{\partial T}{\partial z}}, \qquad 5.2$$

where β is the coefficient of volumetric expansion ($3.2 \times 10^{-3} K^{-1}$ for a temperature of 296K) and g is the acceleration due to the Earth's gravitational field ($9.8 m/s^2$) and when the correct values are used this gives corresponding periods, $2\pi/N$, of 30s approximately. The oscillations can be appreciated in Figure 5.7. These oscillations can be seen at a height between 6-8m.

Also, the field results showed a discontinuity in the temperature profile, this phenomenon is called 'inversion' (Scorer, 1997). In the atmosphere thermal inversions are caused by three main phenomenona (Masters, 1998):

- Radiation inversions which are caused by nocturnal cooling of the earth's surface. This type of thermal inversions occurs close to the ground and last for only a matter of hours.
- Subsidence inversions are the result of the compressive heating of descending air masses in high-pressure zones. This type of inversion may last for months on end and occur at higher elevations in the atmosphere.
- Advection of warm airstreams over a cold surface that is chilled from below by conduction.

Temperature inversion acts as a stable layer settled over the place of interest and effectively restricts the removal and dispersion of pollutants.

In the hangar the thermal inversion can be caused by different factors. These factors could be coupled and have a transient nature. Some of these factors can be:

- Burst of air due to infiltration or exfiltration at low level.
- Deflection of warm air by internal structures.
- Air exchange at high level between the hangars.

Although it has been observed that the use of the heaters affects the thermal inversion, if the hot air blown from the heaters does not penetrate the stratified environment it may be difficult to break the thermal inversion layer. Thus, it is important to know which is the maximum penetration of a hot circular jet in a stratified environment.

5.2.1.2 Test 2

A continuous temperature-logging test was conducted over a two-week period from 4th to 17th and the temperatures were logged in 10min intervals.

The results show the variation of the temperature with time. The test is divided in three parts, each of three days duration.

The fluctuation of the temperature for the first three days of the test is shown in Figure 5.8. In the course of the first 42 hours of this test there was a minimal fluctuation of the temperature. For the three different heights plotted the maximum difference between top and bottom was 3°C. After the initial 42 hours the temperature difference increased to 7.5°C. Also, the last 30 hours the top data series of temperature increases while the bottom series decreases. This could be due to a combination of factors. For example, if

the doors of the hangar were opened thus allowing the entrance of cold air. Whilst at the same time, the heaters were on, causing the rising of the temperature at the top. This suggestion is based on observations that the doors of the hangar where left open during long periods of time and the BEMS sensing a low temperature switched on the heaters, despite the open doors.

Figure 5.9 and Figure 5.10 further show the fluctuation of the temperature on selected vertical heights for days 4-6 and 7-9 respectively. These figures show that during long periods of time there exists a temperature difference between the top and the bottom level which can be as high as 11°C.

The average temperature difference between the height of 2m and 24m over the whole test was 5°C. It was also observed that the temperature difference between the three levels could be low while the temperature inside the hangar drops, Figure 5.9.

On March 10th, the temperature drops in a uniform way at the three levels and at the same time the temperature difference between the top and bottom level is around 3°C, Figure 5.9. This trend is maintained until 08:00 of March 11th when the temperature at the three levels rise uniformly and stays stable from 13:00 till 16:00. After that moment there is a sudden temperature drop at medium and bottom levels of 3°C. However, the temperature at medium levels reaches an acceptable value for human comfort, around 21°C, whilst the bottom temperature is evidently too low. In fact, with the exception of a few hours, the temperature difference between top and bottom levels is around 8°C for more than 24 hours. In addition, from March 14th to March 17th there are periods of time where sudden temperature drops are followed by high temperature differences between top and bottom temperatures, Figure 5.10. This figure shows that from March 15th at 20:00 hours and during the next 24 hours, the temperature at the three levels has a similar path. However, at 22:00 hours of March 16th there is another sudden temperature drop which, again, is followed by an important temperature difference between top and bottom temperature. This behaviour could be due to the entrance of cold air that enhances temperature inversion.

To support this behaviour we will compare three different situations. Figure 5.11 shows similar temperature profiles for March 10th at 22h and March 16th, when the temperature is dropping uniformly and when the temperature at three levels is stable respectively. (In both cases the temperature difference between the top and bottom levels is around 3°C.)

On the other hand, on March 12th at 8:00 hours it is clear that there is a steep break in the stratification profile at a height of 6.5m.

These scenarios may have arisen from a closed-door position with heater system off thus causing the temperature to drop uniformly at the three levels. Then, the hangar is heated and the temperature rises. However, suddenly the doors are opened causing the temperature at medium and low level to fall thus enhancing the temperature inversion at low levels. The door could be closed at any time, but the effect of the entrance of cold air will remain until mixing has occurred. The heater fans could enhance mixing, but without these, buoyancy effects will tend to keep mixing at relatively low levels.

Although temperature values as low as 11.4°C were logged, Figure 5.10, the average temperature over the complete test for the top, middle and bottom levels selected were 22.5, 20 and 17°C, respectively. This shows that the temperature inside the hangar was within the range recommended by ISO Standard 7730, Figure 5.12.

5.2.1.3 Test 3

The results of the boundary conditions are shown in Table 5.1. The velocity and temperature of the heaters/fans recorded is an average value. The velocity values range from 4 to 16 m/s and the temperatures from 60 to 30°C; these values are similar to those reported by Day (1990).

The outlets are not always in operation. They are operated only whilst spray painting in some aeroplane is being undertaken.

5.2.1.4 Test 4

The jet penetration test showed that for a single jet with heater on and when the doors are closed the penetration distance was approximately 19m.

This was verified by doing velocity and powder smoke measurements which showed that at a height of around 3 to 4m the air velocity drops from around 1m/s to 0.2m/s.

The visualisation carried out with plastic streamers allowed us to estimate the maximum penetration of the jet. We must recall that the hangar was in operation during the test and that the tests were performed during a short period of time. Thus, it was not possible to be certain that a steady state was achieved. Figure 5.13 show that the streamer falls abruptly at a height of approximately 4m when the doors are closed (the ladder at the

left-hand side of the picture has a height of 3.5m). However, when the west door was opened the jet penetration was reduced to approximately 16m, Figure 5.14. The sketch in Figure 5.15 gives a general perspective of the hangar in this test. Figure 5.15.B in particular suggest that the decrease in the jet penetration could be related to air exchange with the exterior.

5.2.2 Experimental results. Tank.

5.2.2.1 Description of the flow

Following the explanation of Baines et al. (1993) we will describe the flow observed in the experiments. At the beginning of the experiment the jet advances to a penetration depth where the momentum is reduced to zero. Then a mixture of the source fluid of temperature T_o and the environment fluid of temperature T_e floats back around the downward flow, with considerable horizontal spreading. Because this mixture has a temperature higher than T_e buoyancy keeps it at the top of the tank, as sketched in Figure 5.16.A. As time progresses there is a gradual increase in the jet penetration as the ambient temperature increases, Figure 5.16.B. Finally a sharp interface forms, Figure 5.16.C.

When the upward flow reaches the top, it spreads laterally. The fluid in the layer is hotter than the environment in a lower position, so mixing is inhibited. However, the jet flux produces a downward velocity at the bottom of the mixed layer and so a front of constant temperature moves downward. Figure 5.17 illustrate the last: A correspond to the initial stratification; B, C and D shows the advance of the front during a period of time of 12:33h.

As time progresses the temperature of the mixed layer increases because of the continuos re-entrainment to the jet, which results in a stable temperature profile between the top of the tank and the final penetration. As the surface of constant temperature descends, entrainment reduces the distance between them. Thus a sharp interface forms at the end of the jet where the environment velocity is close to zero.

The flow was visualised with food colouring, as described in Chapter 4. Figure 5.18 shows the structure of the flow in experiment number 2. The frames showed in the figure were taken at intervals of 2s and present the state of the flow after approximately 26h after the jet inlet has been opened. Frames A-F show the development of the jet

until it reaches the maximum penetration depth. We can appreciate that the jet has a turbulent behaviour. This is more evident in the rest of the frames were the spreading of the jet reveals an extensive entrainment. When the jet reaches the maximum penetration it starts to expand horizontally and, at the same time, a strong back-flow develops, which generates a considerable amount of mixing in the upper part of the tank. Advance of the hot fluid at this stage depends on the entrainment at the bottom of the jet.

5.2.2.2 Flow penetration

Ten experiments were undertaken in the laboratory. Information about the experiments is presented in Table 5.2. The penetration distance, *Zpi*, was quantified by defining it as the vertical distance from the jet inlet to the location where the temperature difference between two consecutive levels was 1-%. Food colouring was used to mark the height where the jet comes to a halt. Also, temperature measurements were undertaken to obtain the maximum penetration depth.

In all the experiments two zones divided by a sharp interface were observed. Figure 5.19 presents images of experiments 1 and 5 where the sharp interface formed between the (top) zone influenced by the jet and the stratified and motionless (bottom) zone can be seen. The measured temperature field for experiments 1 and 5 is shown in Figure 5.20. As expected the effect of the buoyancy force keeps the top zone of the tank hotter that the bottom. The temperature in the downward flow decreases very slowly as the distance from the inlet increases. An abrupt change in temperature marks the level of the penetration of the jet. From there the jet spreads horizontally and upwards, promoting the mixing of the fluid in the upper zone. This effect becomes evident when we observe the almost uniform temperature field at the top zone of the tank. The lower zone of the tank shows a clear stratification. The shape of the stratification is not linear as can be seen in Figure 5.21. This can be explained by the fact that the walls of the tank were not perfectly insulated, and some energy transport does occur here.

Based on the dimensional analysis, presented in Chapter 4, it has been decided to display the dimensionless penetration depth as a function of the Froude number, defined as:

$$Fr = \frac{W_o^2}{\bar{g} r_o}, \qquad 5.3$$

and

$$\overline{g} = \frac{\rho_a - \rho_o}{\rho_m} g, \qquad 5.4$$

where ρ_a, ρ_o and ρ_m are the ambient, inlet and mean density of water, respectively.

An appropriate value for density of water, ρ, is needed in the calculation of the Froude number. Gebhart et al. (1984) has stressed the need for an accurate equation of state, if the initial temperature difference between the jet and the ambient is greater than 3°C. The value of ρ was obtained from the equation reported by Popiel and Wojtkowiak (1998):

$$\rho = a + bT + cT^2 + dT^{2.5} + eT^3, \qquad 5.5$$

where a = 999.79684, b = 0.068317355, c = -0.0107402248, d = -0.00082140905, and e = -2.3030988x10^{-5}, and T is the temperature in Celsius. The estimated uncertainty of Equation 5.5 is ±0.002% to ±0.004%.

Figure 5.22 shows that the dimensionless downward penetration distance, Zpi/r_o, is very well correlated in terms of $Fr^{1/2}$, over the range investigated, since a single curve fits the data. The experimental results are consistently higher than the correlation of Zhang and Baddour (1998). A higher value of the constant means a decrease in the entrainment of fluid from the environment to the jet and an increase in the penetration depth. The value of the constant reported by Zhang and Baddour is 11.04% lower than that obtained in this work. These researchers placed a ruler close to the jet to measured jet penetration above the nozzle. Thus, the difference could be due to experimental error. However, a reduction of the entrainment was expected since in our experiments the relative buoyancy between the jet flow and the environment is lower. As mentioned in Chapter 2, Zhang and Baddour allowed the dense layer to spread on the bottom without affecting the jet behaviour. Finally, stratification reduces the effect of buoyancy at the beginning of the jet development due to a reduced temperature difference between the ambient fluid and the jet fluid.

5.2.2.3 The hangar and the tank

The penetration depth of the jet in the hangar was estimated using the correlations obtained in the laboratory experiments and compared with some of those found in the literature. The data used to calculate the penetration in the hangar is presented in Table

5.3 and the results in Table 5.4. The correlations based only on the Froude number underpredict the penetration distance observed in the hangar. The penetration depth calculate with correlation obtained in this work predicts a value 20% lower whilst the other correlations predict on average a value 35% lower.

The experiments undertaken in the tank also helped to understand some events seen in the industrial case. In particular, the temperature measurements in the hangar showed an oscillation layer at a height between 5-8m, approximately. This oscillatory movement was explained as the result of gravity waves in the interface of two thermally different layers. The period of the motion of these waves were roughly predicted by the buoyancy frequency.

Figure 5.23 shows the temperature field at the centre of the tank for experiment 9. Figure 5.24 depicts a magnification of the zone where the jet reaches the maximum penetration depth. In that zone the flow has lost much of its momentum and buoyancy forces became predominant. The fluid then flows out towards the sides and not being cold enough to sink buoyancy drives the fluid upward towards its equilibrium position. The arrows in Figure 5.24 illustrate this movement. The temperature in the marked points of this latter figure is plotted in Figure 5.25. As can be appreciated the temperature in point 1 varies considerably, the standard deviation at this point is 1.53°C whilst in points 2 and 3 is 0.85 and 0.78°C, respectively. The fluid in this zone is turbulent and oscillatory. Taking in account that the gradient at the centre between the heights of 46 and 42cm is 251°C/m; the period of the oscillations is 6.3s approximately. Also, by performing a Fourier analysis of the data we can obtain the characteristic period of the data. The result of this analysis is presented in Figure 5.26; the value of the characteristic period is similar to that predicted by the buoyancy frequency. The ordinate in Figure 5.26 shows the characteristic period and the abscissa the complex magnitude squared of the coefficients of a Fourier series. The figure also shows some spikes for longer periods, which can be explained on the randomness of the phenomenon. The presence of sudden high or low values of temperature causes a skew in the data that affect the analysis.

The temperature field in the hangar on March 19th is showed in Figure 5.27. The locations of points 1 to 6 corresponds to positions along the horizontal dimension of the hangar of 6, 30, 34, 54, 66 and 90m, respectively. The missing data was obtained using the filling method named kriging. This is a weighted fill method that looks at statistical

distances rather than physical distances. Conceptually the variance in kriging plays the role of a weighting function (Davis J.C. 1973). Kriging work best with datasets that have regions of densely scattered data and other regions of lightly scattered data, as is the case with the available data for the hangar.

The tongue of high temperature showed in Figure 5.27 is due to hot air being blown by heater seven. A similar structure cannot be seen in the other side of the figure because the measuring points five and six are too far apart. The figure also suggest that, as in the tank, the hottest air reach the maximum penetration at some point between the heights 9 to 5m and then start raising towards its equilibrium position. The raising air is colder than the air at the position of the maximum penetration.

Finally, the fluid in the zone of maximum penetration is turbulent and oscillatory. The period of the oscillations in the hangar was estimated as 30s approximately. If the real period is around 24s the sampling rate, Δt = 5s, and the length of time used to sample, t = 120s, would not be enough to reproduce with fidelity the characteristic form of the temperature oscillations that is corrupted by random noise as shown in Figure 5.28. It is possible that relevant information has not been detected. This effect it is much more likely in the zones were the jet is close to its maximum penetration depth.

5.3 Porosity affected flow

This section present the information obtained by measurements made in Nestle's food storeroom. Also, the data obtained different experiments undertaken in the laboratory. The laboratory experiments were designed to obtain basic data of the moisture absorption of the product. Because of this basic approach a first-order-type kinetics model was adopted to describe the water sorption of the product. This type of model assumes that the main resistance to mass transfer is at the outer layer of the sample (Machado et al. 1998).

5.3.1 Experimental results. Food repository.

5.3.1.1 Point Temperature Logging

The average temperature in the room was 19.5°C, the minimum temperature was 15.3°C, whilst the maximum was 20.9°C. Figure 5.29 plots interpolated data for the whole central area of the room. It should be noted that the data was taken under normal working conditions of the room, and that can explain why highest temperatures are towards the ovens.

Temperature and relative humidity under each of the inlets was also taken. The average temperature at the inlets was 20.6°C, the highest temperature recorded was 21.2°C whilst the lowest was 19.8°C at inlet number 8. The numbering of inlets and outlets is shown in Figure 4.12. The average RH at the inlets was 50.5%.

5.3.1.2 Continuous Temperature Logging

The temperature measurements in the room for the time of the test showed an almost constant pattern. The average temperature during the test period was 21.3°C, with a standard deviation of 0.22°C. Figure 5.30 shows data for a period of 24 hours.

5.3.1.3 Velocity Measurements

The air velocity from the inlets was unevenly distributed, as can be appreciated in Figure 5.31. The performance of the ventilation system can be explained considering the balance of pressure head, $p/\rho g$, and the velocity head, $u^2/2g$, in the Bernoulli equation. The average velocity is 2.9m/s.

The outlets in the room have a damper that controls the bottom flow, the top of the outlet is open. The position of the damper for the different outlets is presented in Table 5.5. The present arrangement of the dampers has been established from practical experience, and has shown an acceptable performance throughout time.

Airflow measurements were undertaken in the ductwork, as show in Figure 5.32. In the fresh air section the air velocity was measured each 50mm over the entire diameter of the duct. The velocity was measured four times at each location. The data shown in the graph correspond to the average of the experimental data collected at each point. The experimental data were fitted using a polynomial curve that was integrated over the measured distance to obtain the averaged velocity, as illustrated in Figure 5.33. The profile shown by the measurements is fairly flat as expected. The average velocity is 9.48m/s and the calculated volumetric flow is $3.41m^3/s$.

The flow in the return duct comes from the maturing room and mixes with the fresh air a short distance downstream of the measuring location. The average velocity is 4.11m/s approximately. The estimated volumetric flow is $4.11m^3/s$. Figure 5.34 shows the velocity profile for the return air duct.

The profile shown by the measurements in the supply duct is as expected: high velocity distribution near the edge with an appreciable diminution of the velocities just passing through the centre of the duct, Figure 5.35. The average velocity is 10.65m/s. The estimated volumetric flow is $8.62m^3/s$ which is approximately 15% higher than expected. This discrepancy may be due to the anemometer not being able to obtain an accurate measurement due to the high turbulence (flow direction not constant) created by the maldistribution in the duct. The manufacturer (Solomat 127 MS) of the anemometer does not specify accuracy levels above 12m/s.

Finally, 15 spot air velocity measurements were undertaken along the main corridor of the room at 3 different heights: 0.5, 1.0 and 1.5m. The average velocity of these measurements was 0.11m/s.

5.3.1.4 Wafers in cabinets

In general, experimental results showed that well packed trays absorb more water vapour than those badly packed. In particular, after 25h the moisture uptake of well packed trays with the 2 Finger arrangement is 1.83 times the moisture uptake of badly packed trays with the same arrangement. A similar trend was observed with the 4 Finger

arrangement, where, for example, the moisture uptake of the well-packed tray trays is 1.66 times the moisture uptake of badly packed trays after approximately 26h. The effect of the packing technique on moisture take-up for the 2 and 4 Finger arrangements is illustrated in Figure 5.36 and Figure 5.37, respectively.

The packing technique does not seem to have an influence on the moisture uptake if the ambient relative humidity is reduced from 50% to 35%, as can be seen in Figure 5.38. By contrast, reducing the space available for the air to flow due to bad packaging has a similar effect than reducing the relative humidity, as shown in Figure 5.39. Bad packaging reduces the space available as much as 69.5% in the 4 Finger arrangement; whilst for the 2 Finger arrangement the space reduction is 25.5%.

The effect of the packing technique seems to have a more influence on the moisture take up than the arrangement of the wafers. The data depicted in Figure 5.40 shows that the moisture uptake of 2 Finger well packed trays is 13% higher than 4 Finger well packed trays after approximately 25h. For about the same time, the moisture uptake of 2 Finger well packed trays is 87.5% higher than 4 Finger bad packed trays.

Although the packing technique does not seen to have a significant effect on moisture absorption under low ambient relative humidity, reducing the air velocity by 80%, from 2.5 to 0.5 m/s, decreases the moisture uptake by approximately 75%. It should be noted that by applying the usual mass transfer analogy, the reduction of the mass transfer coefficients for the same velocities used in test is 74%. Figure 5.41 shows the effect of air velocity on the averaged moisture uptake of a stack of three trays.

The data obtained suggest that moisture uptake could be increased more than 50% by using a well packing technique. Besides, bad packing has a similar effect on moisture uptake as reducing relative humidity of the surrounding air. Also, increasing air velocity clearly helps to promote moisture uptake.

5.3.1.5 Moisture measurements in maturing room

Experiments done with silicagel bags have shown an uneven vertical moisture uptake, as can be appreciated in Figure 5.42. The data suggest better moisture pick up at the top of each stack. This behaviour could be explained because the trays are open at the top, whilst the bottom of the tray is well 'sealed'.

Silicagel bags located on the bottom stack seems to absorb more moisture. For instance, by averaging the moisture uptake of the three trays in each stack the moisture uptake of bottom stack is 17% higher than the top stack in row 34, and 7% higher in row 23, as can be seen in Figure 5.43. This could be an effect of more air being pushed from the inlets through the bottom stack. It should be noted that silicagel bags in row 23 where located in a 2 Finger zone, thus more air was allowed to flow around them. Also, the data depicted in Figure 5.43 has been normalised to one day because the original data for row 24 and row 34 were for 6.7 and 10.7 days respectively.

The data obtained for silicagel in the room for different periods of time was normalised using experimental results of silicagel in cabinets. An exponential function was fitted to the latter data as follows:

$$\Delta W_c = 0.43\left(1-\exp(-kt)\right) . \qquad 5.6$$

In equation 5.6, ΔW_c is the moisture uptake in kg, the value 0.43 is the maximum moisture uptake for the test period, t is time in seconds and k is a coefficient that has a value of $2.4\text{x}10^{-6}$. It is expected that both, silicagel in the cabinets and in the room will reach the same maximum if given enough time. The coefficient k is a function mainly of air velocity. Figure 5.44 represents experimental data from cabinets and the fitting curve for that data.

Also shown in Figure 5.44 is averaged data of silicagel moisture uptake in the room. The fitting curve for this data was obtained by using the following expression:

$$\Delta W_c = 0.43\left(1-\exp\left(-k\left(\frac{k_r}{k_c}\right)t\right)\right) , \qquad 5.7$$

where k_r and k_c are mass transfer coefficients calculated using the heat and mass transfer analogy. To estimate k_c the value of the velocity was 2m s^{-1} and to estimate k_r the value was 0.1ms-1. The former corresponds to the averaged velocity at the inlets of the cabinet; the latter to the averaged velocities measured in the room. Despite all the assumptions the fitted curve is only 26% higher than the expected values. By carefully adjusting the value of the coefficient k it is possible to get a curve to fit the data obtained in the room and normalise them to a desired period of time for comparison purposes.

By normalising data to one day for wafers in bay 4 at an approximate height of 3m from the floor and interpolating between them in the horizontal dimension, a 'map' of the moisture uptake was constructed. The data in Figure 5.45 shows high moisture uptake for the wafer facing the inlets. Also there is a 'moist' area near inlet number 12. As expected the absorption of water diminishes as we approach the walls. Moreover, we can appreciate the uneven moisture distribution on the horizontal dimension, with differences up to 36% between 'wet' and 'dry' areas.

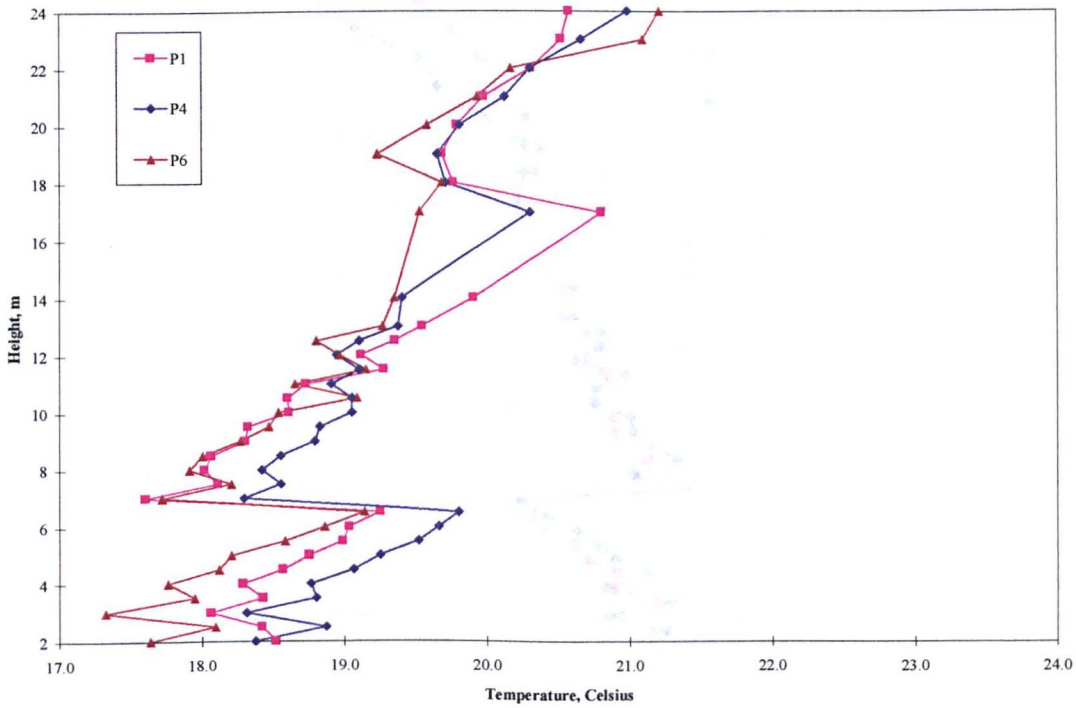

Figure 5.1. February 6th. Points 1,4 and 6.

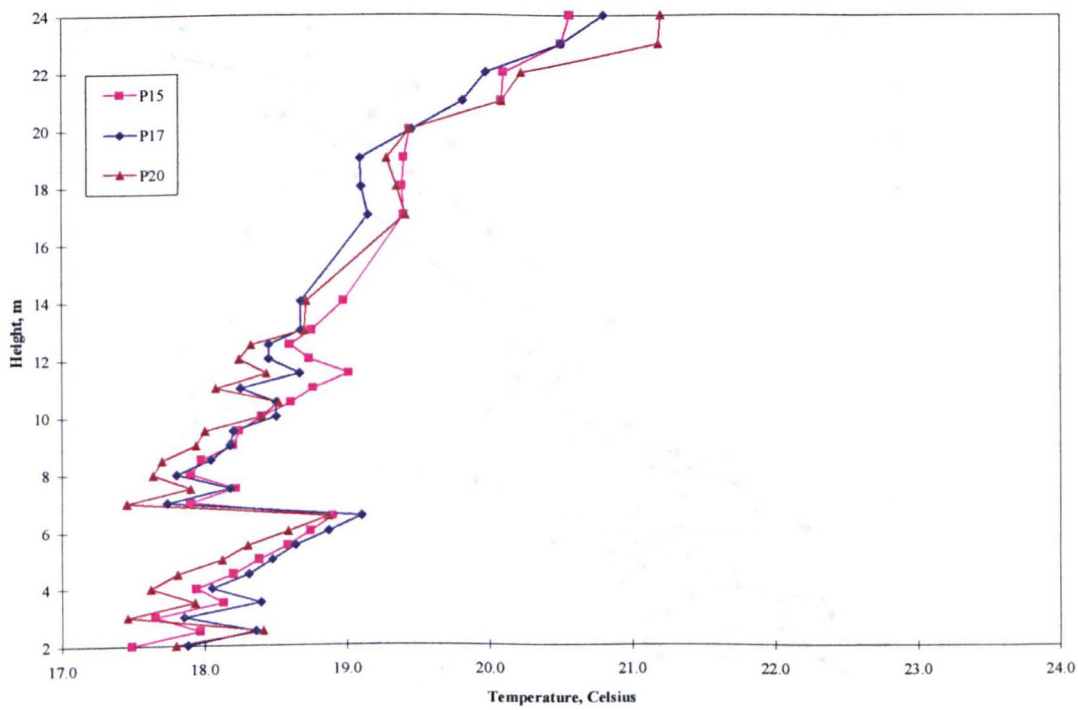

Figure 5.2. February 6th. Points 15, 17 and 20.

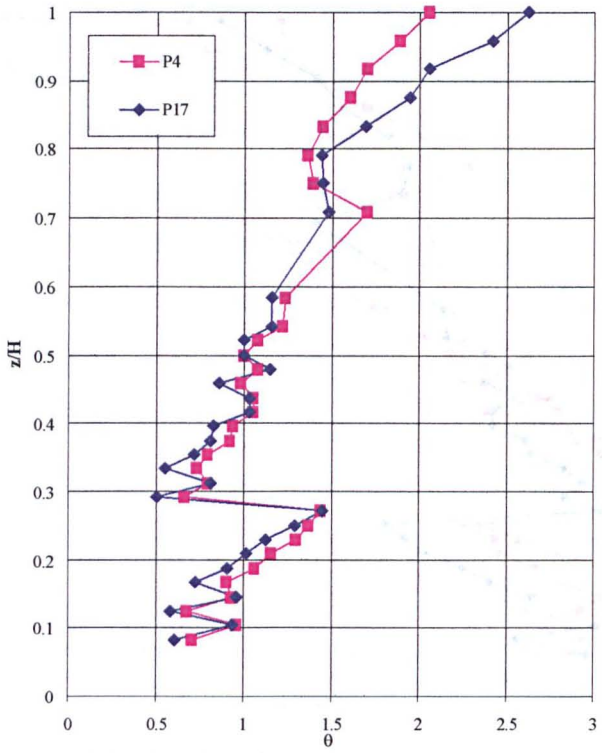

Figure 5.3. Comparison of vertical temperature stratification for points 4 and 17 on February 6th.

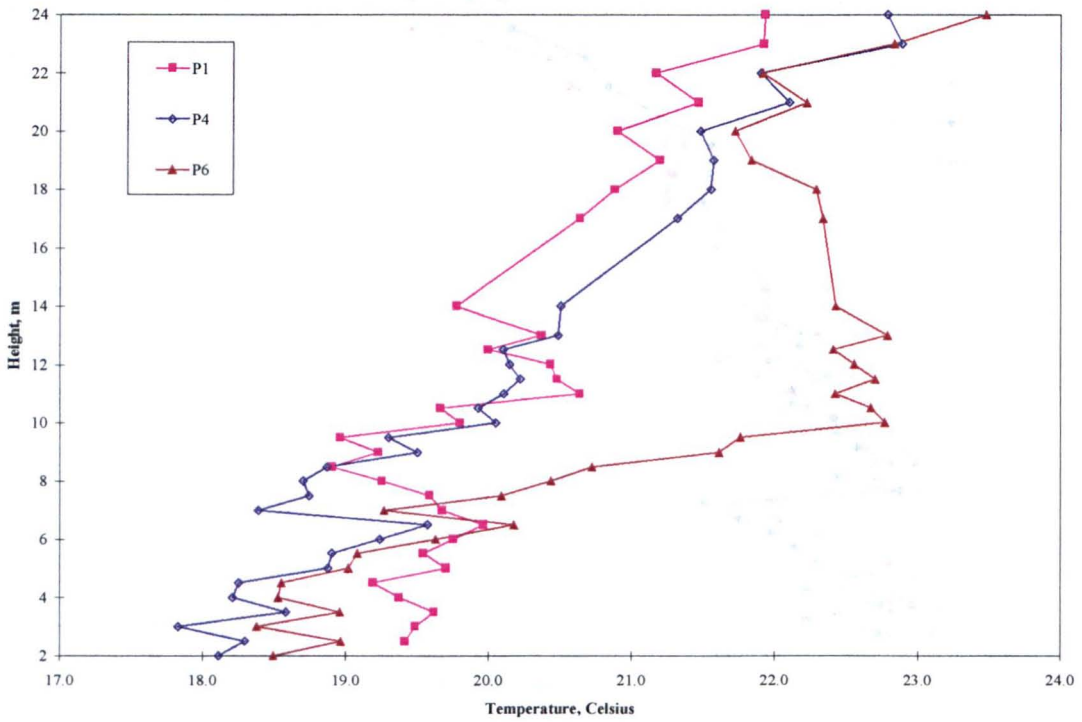

Figure 5.4. March 19th. Points 1, 4 and 6.

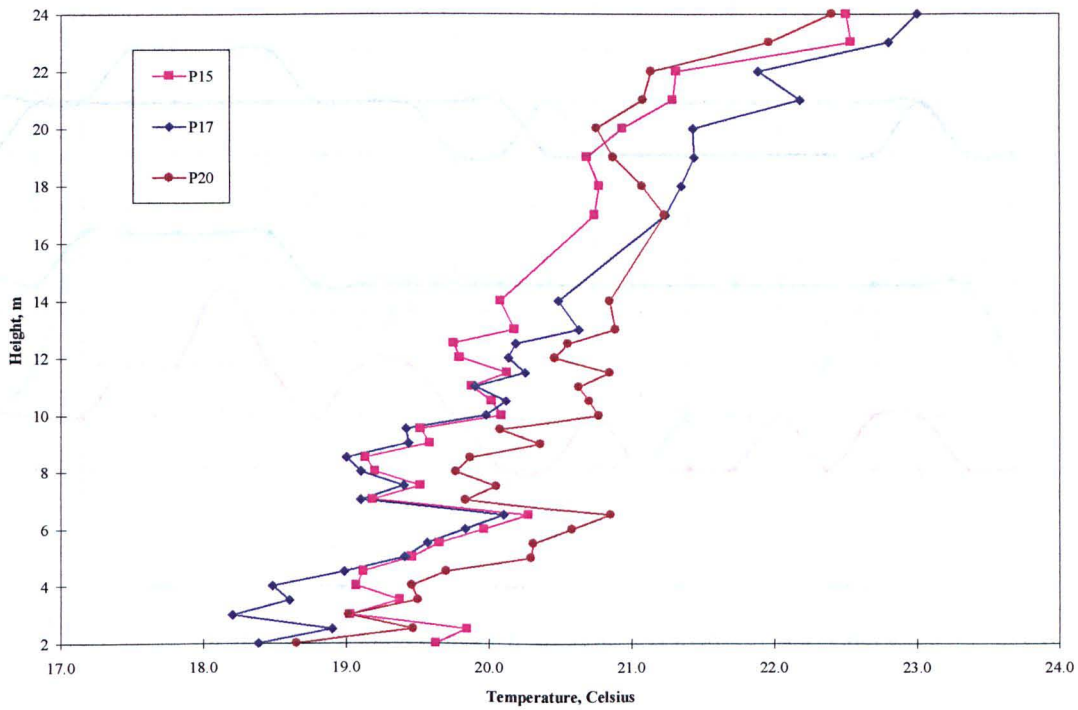

Figure 5.5. March 19th. Points 15, 17 and 20.

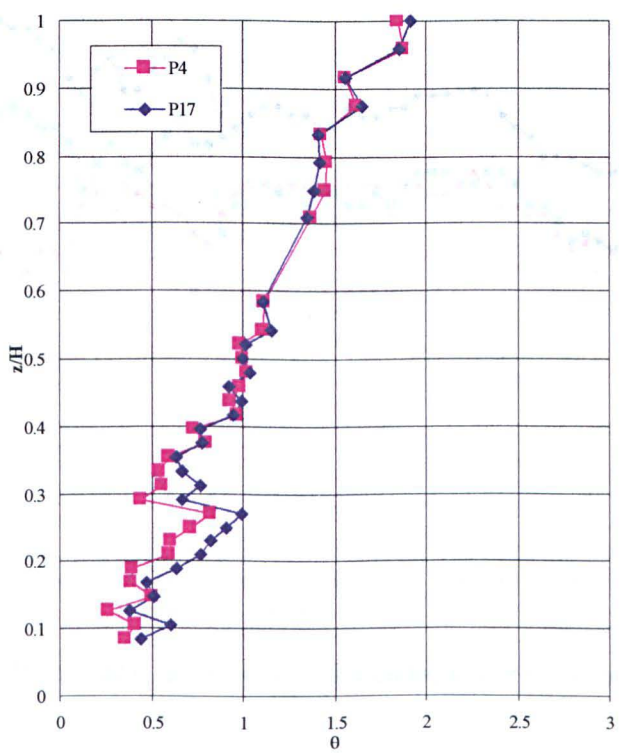

Figure 5.6. Comparison of vertical temperature stratification for points 4 and 17 on March 19th.

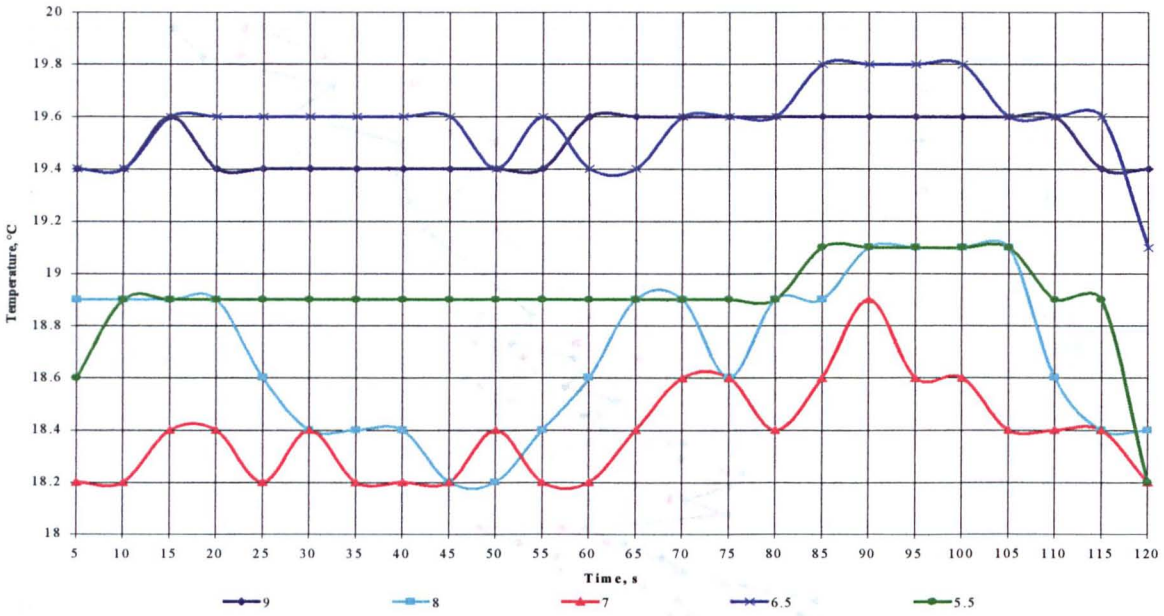

Figure 5.7. Temperature variation in time at point 4 in March 19th.

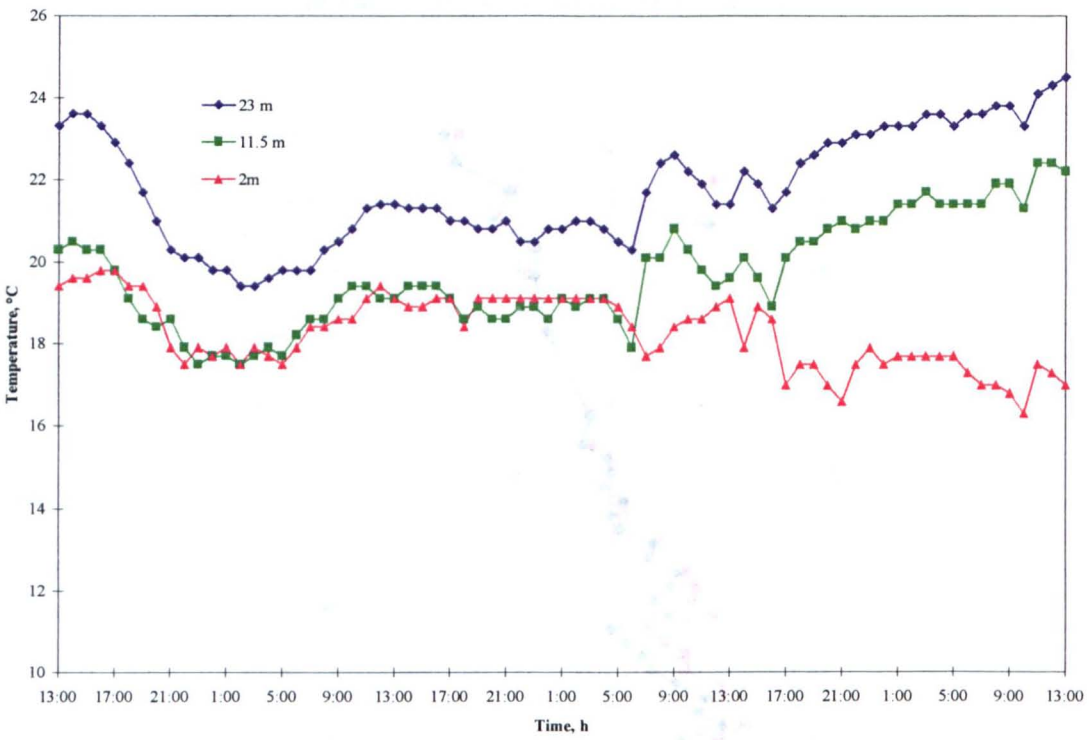

Figure 5.8. March 6 to 9. Temperature fluctuation at top, middle and bottom height.

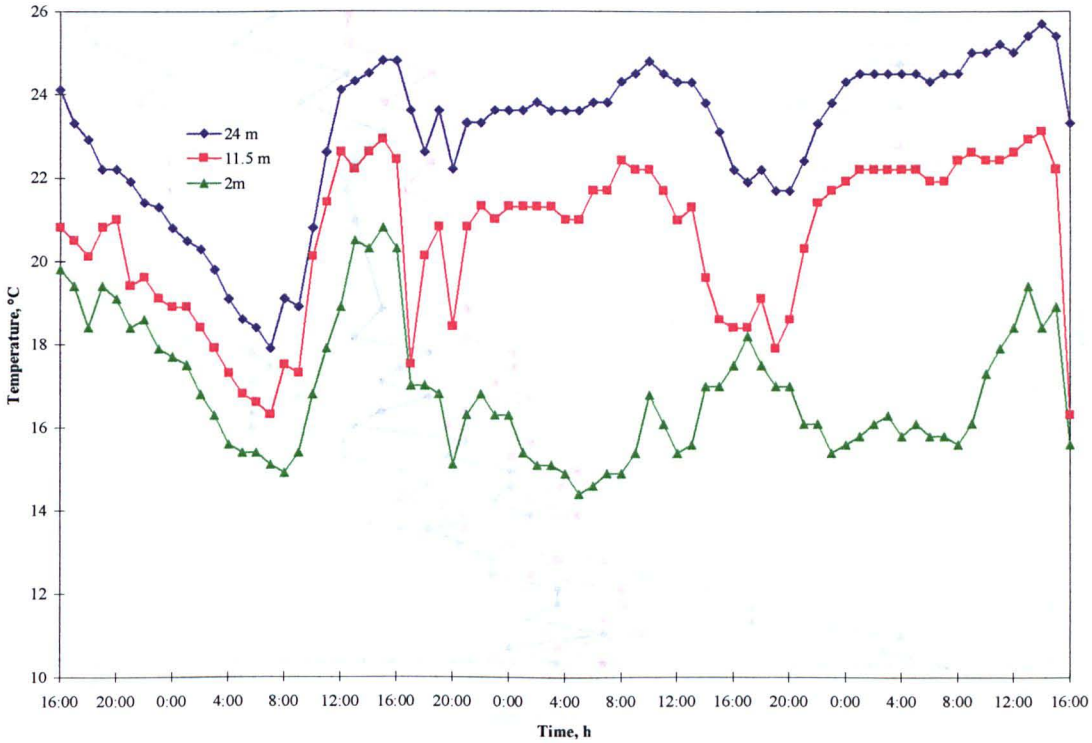

Figure 5.9. March 10 to 13. Temperature fluctuation at top, middle and bottom height.

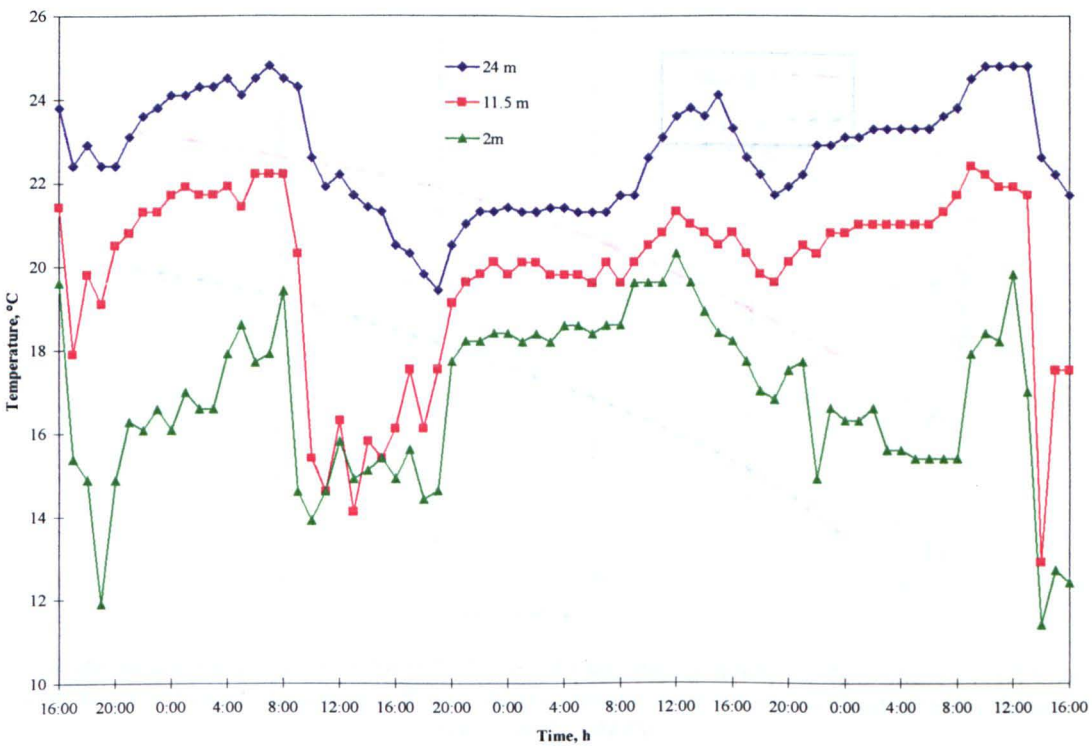

Figure 5.10. March 14 to 17. Temperature fluctuation at top, middle and bottom height.

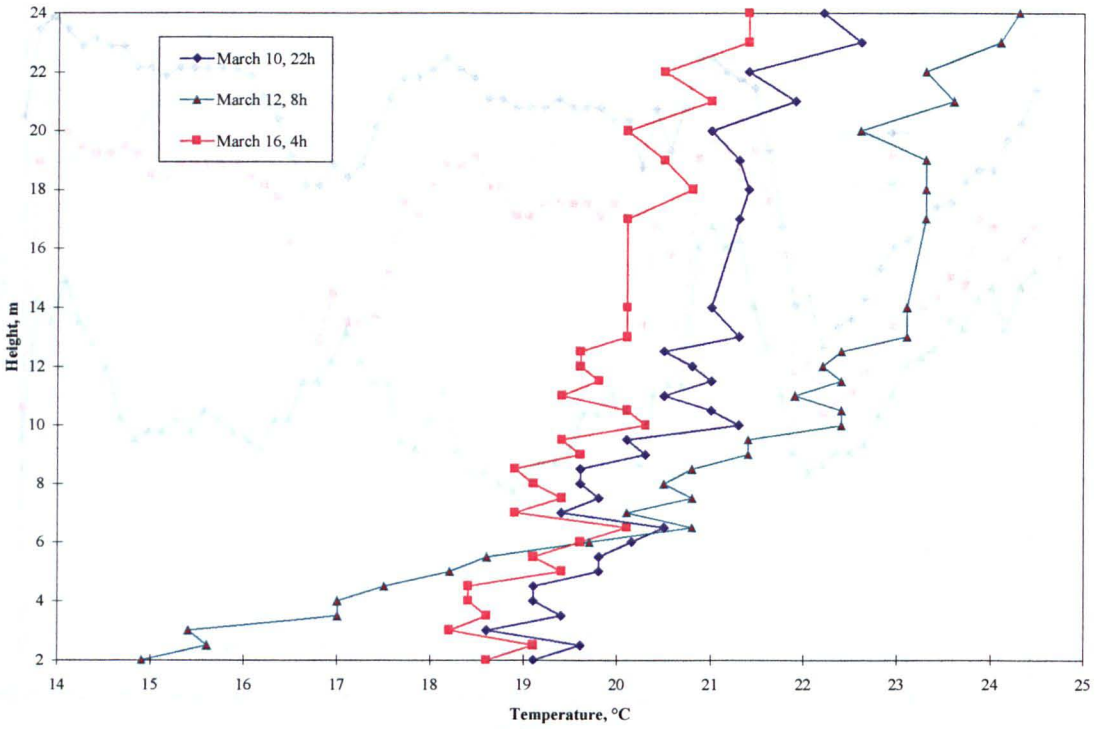

Figure 5.11. Temperature profiles for March 10, 12 and 16 at 22:00, 8:00 and 4:00 respectively.

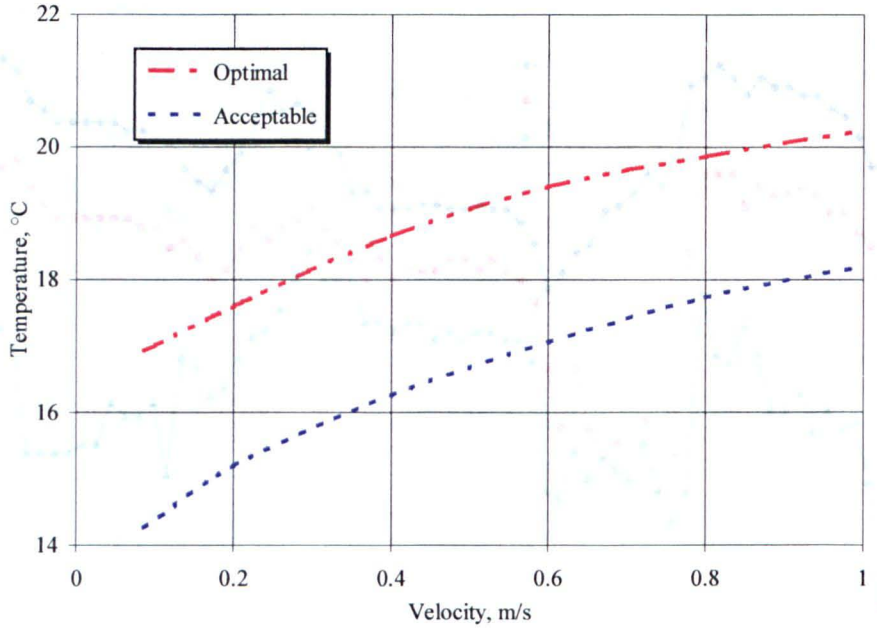

Figure 5.12. Optimal and acceptable ranges (ISO Standard 7730) of air temperature and air speed in the occupied zone for medium human level activity (116 Wm^{-2}). Winter period. (From Olesen B.W. and Zhidov A.M. 1994).

Table 5.1. Results test 3.

Site	Velocity, m/s	Temperature, °C
Inlets	10.0 –16.0	50
Outlets	0.25 - 11.0	17
Infiltration	0.1 - 3.7	14
T wall E	-	15
T wall W	-	16
T wall N	-	16
T wall S	-	14
T roof	-	18
T floor	-	17
T outside	-	14

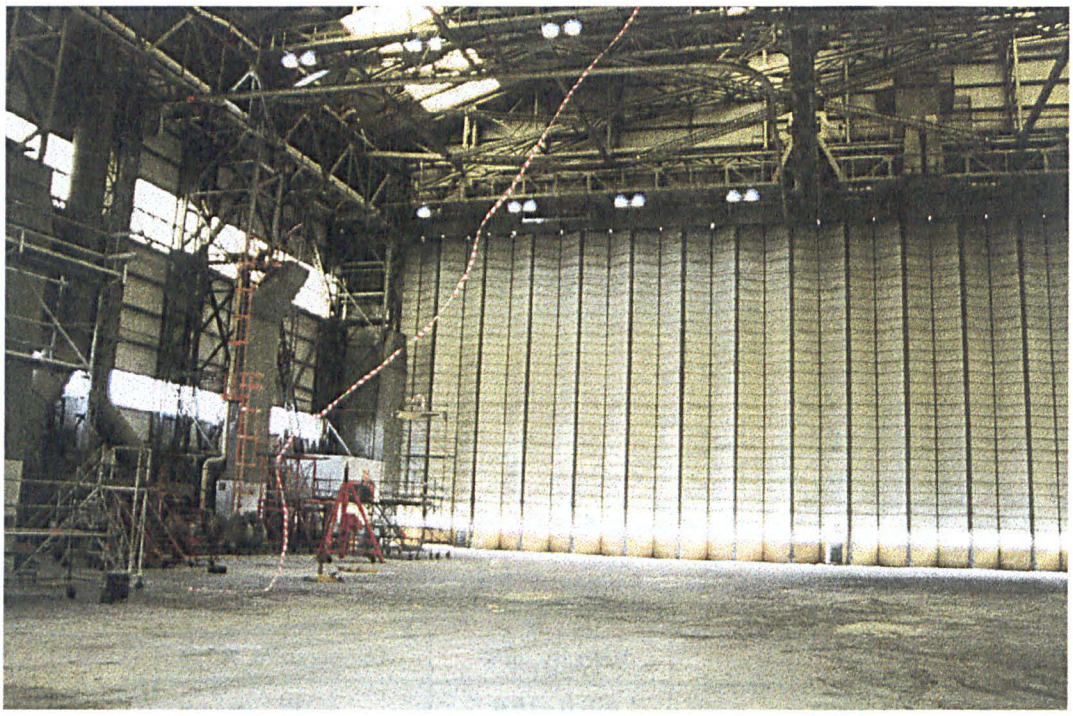

Figure 5.13. Viusalization of jet penetration. Door closed.

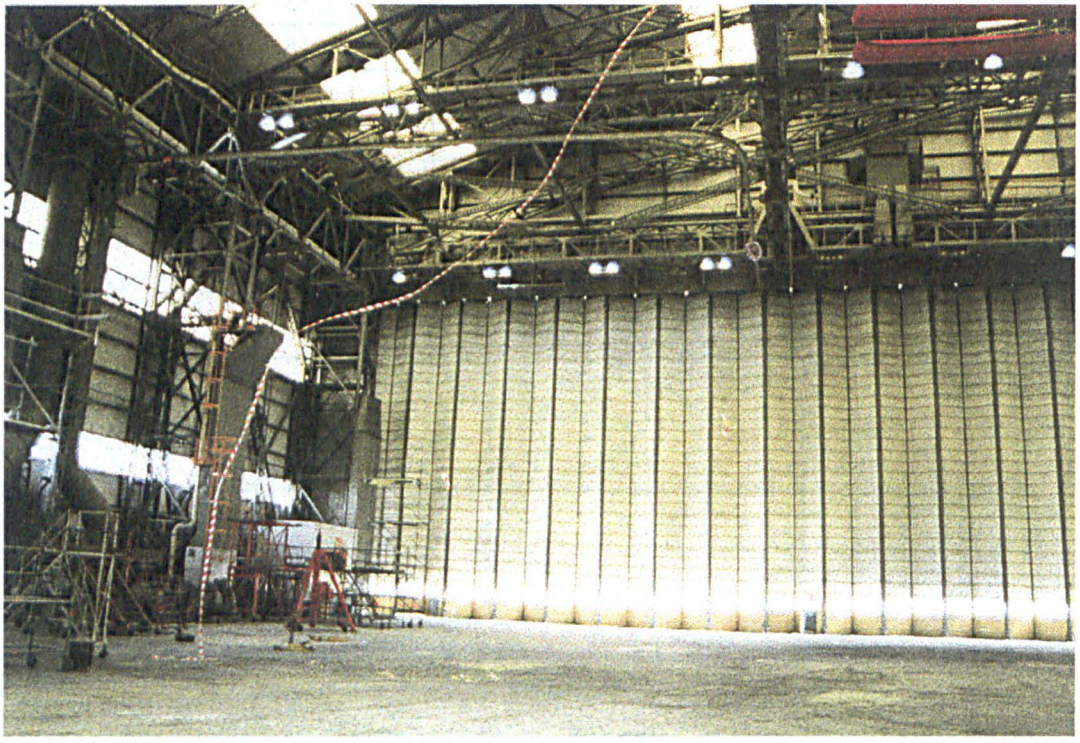

Figure 5.14. Viusalization of jet penetration. Door open.

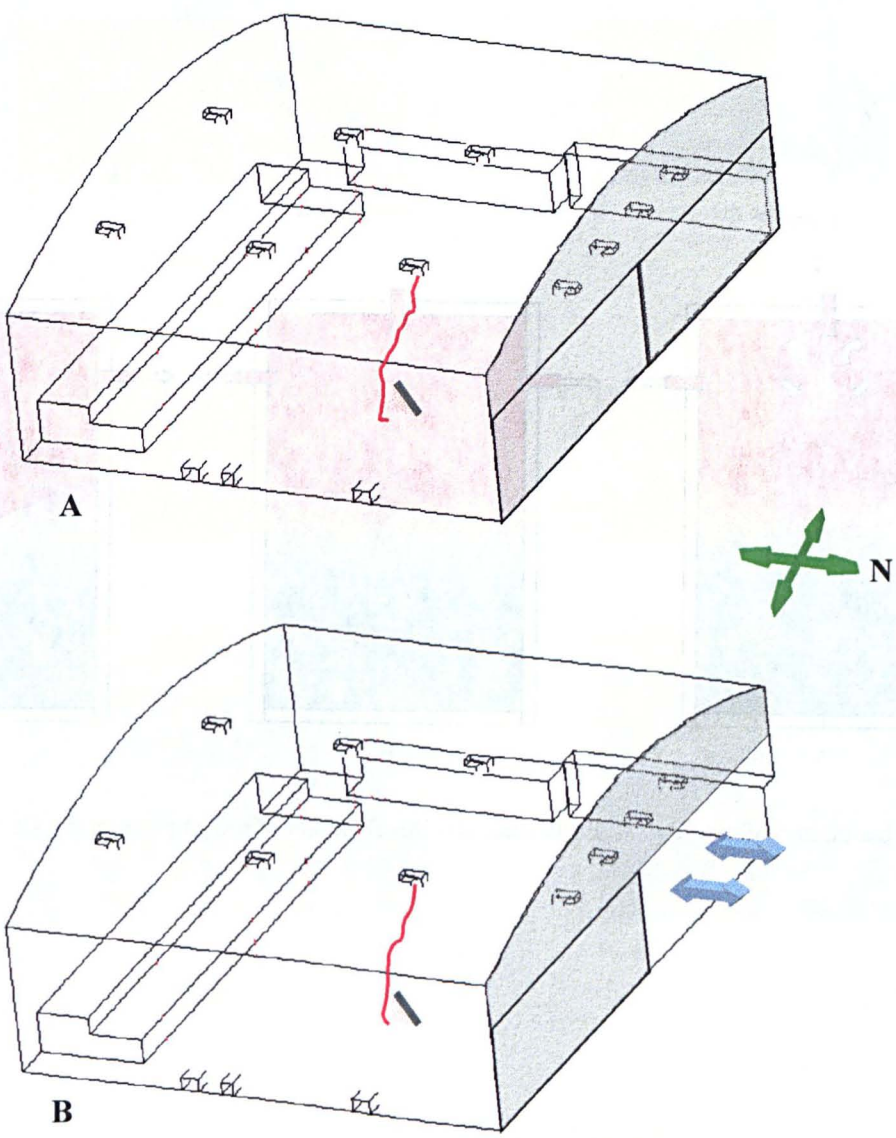

Figure 5.15. Skectch for the streamer visualization.

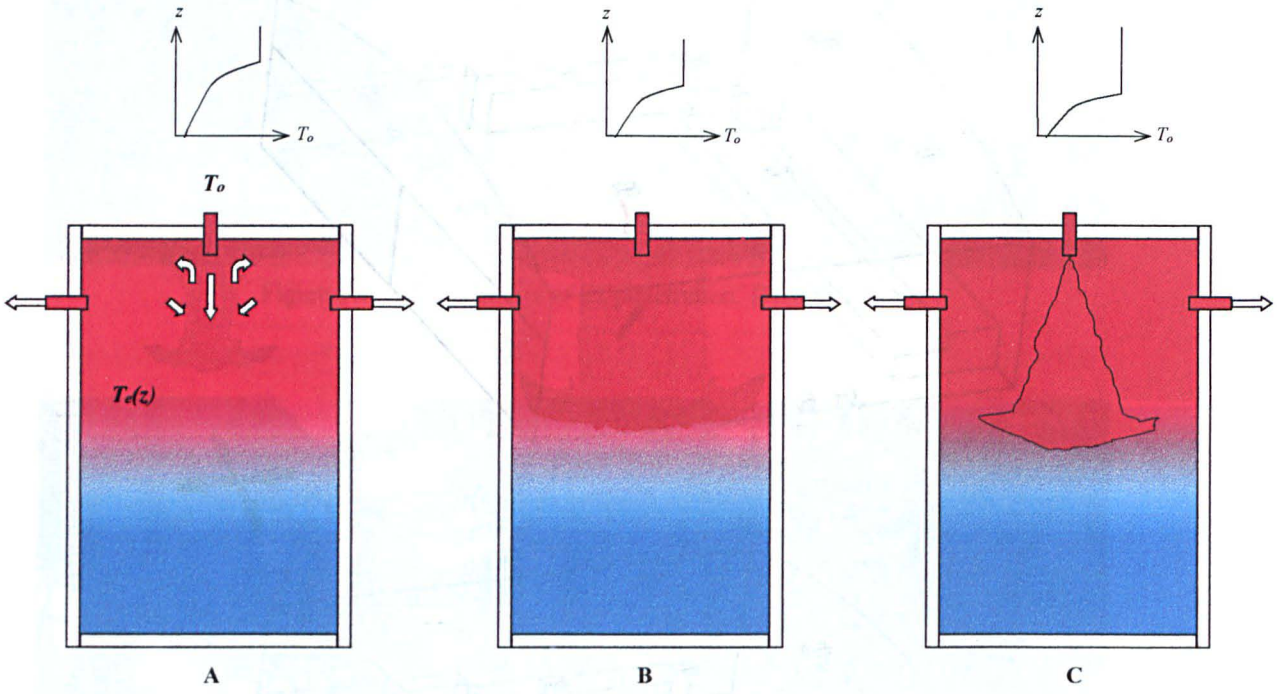

Figure 5.16. Desciption of the flow. A) Early stage. B) Development of the jet penetration. C) Final stage.

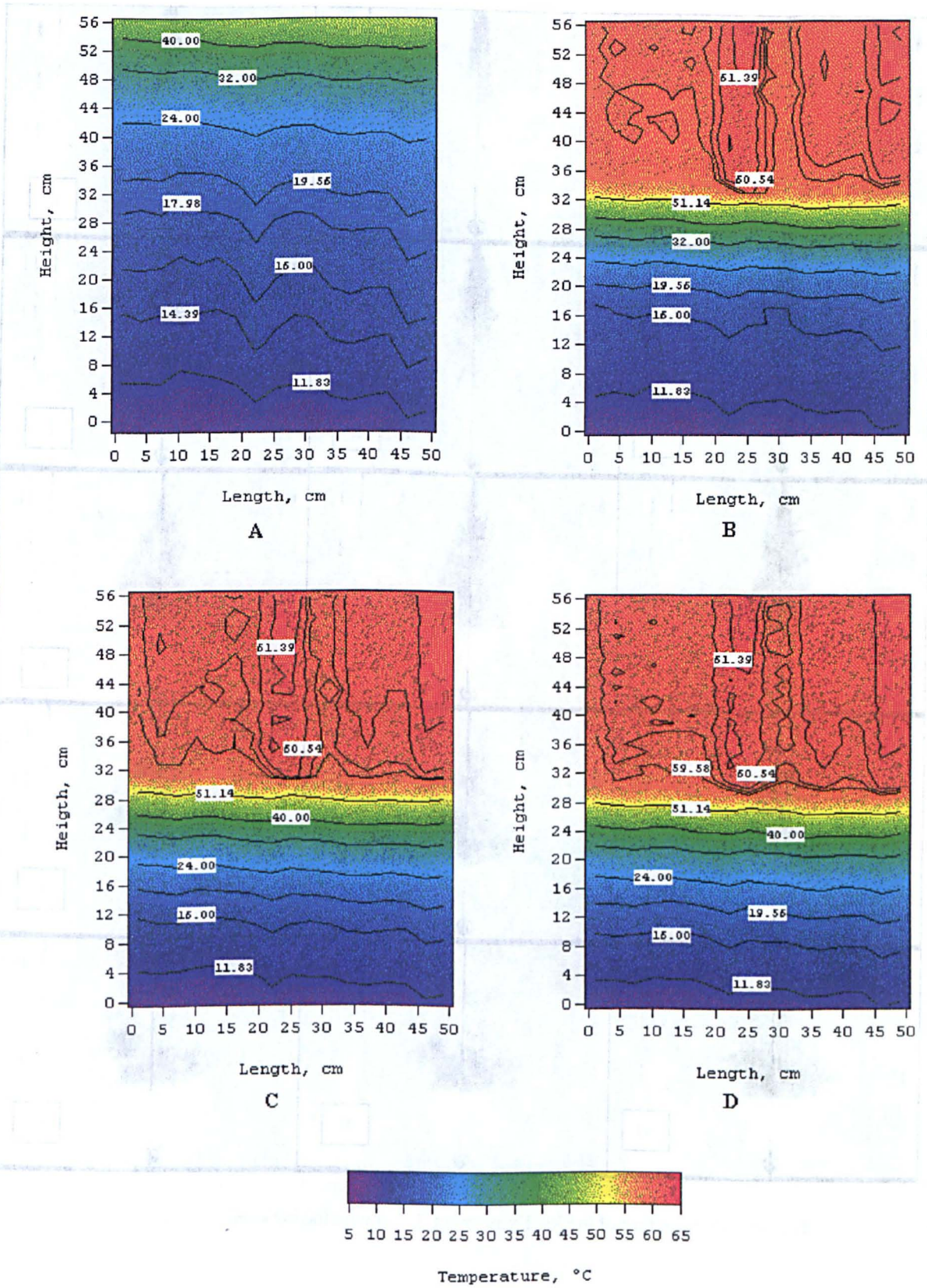

Figure 5.17. Advance of the temperature front in experiment 2. A) Initial stratification; B) After 12h of opening the jet inlet; C) After 20.89h; D) After 24.33h. Fr_o =1314; $S_o = 8.45 \times 10^{-3}$.

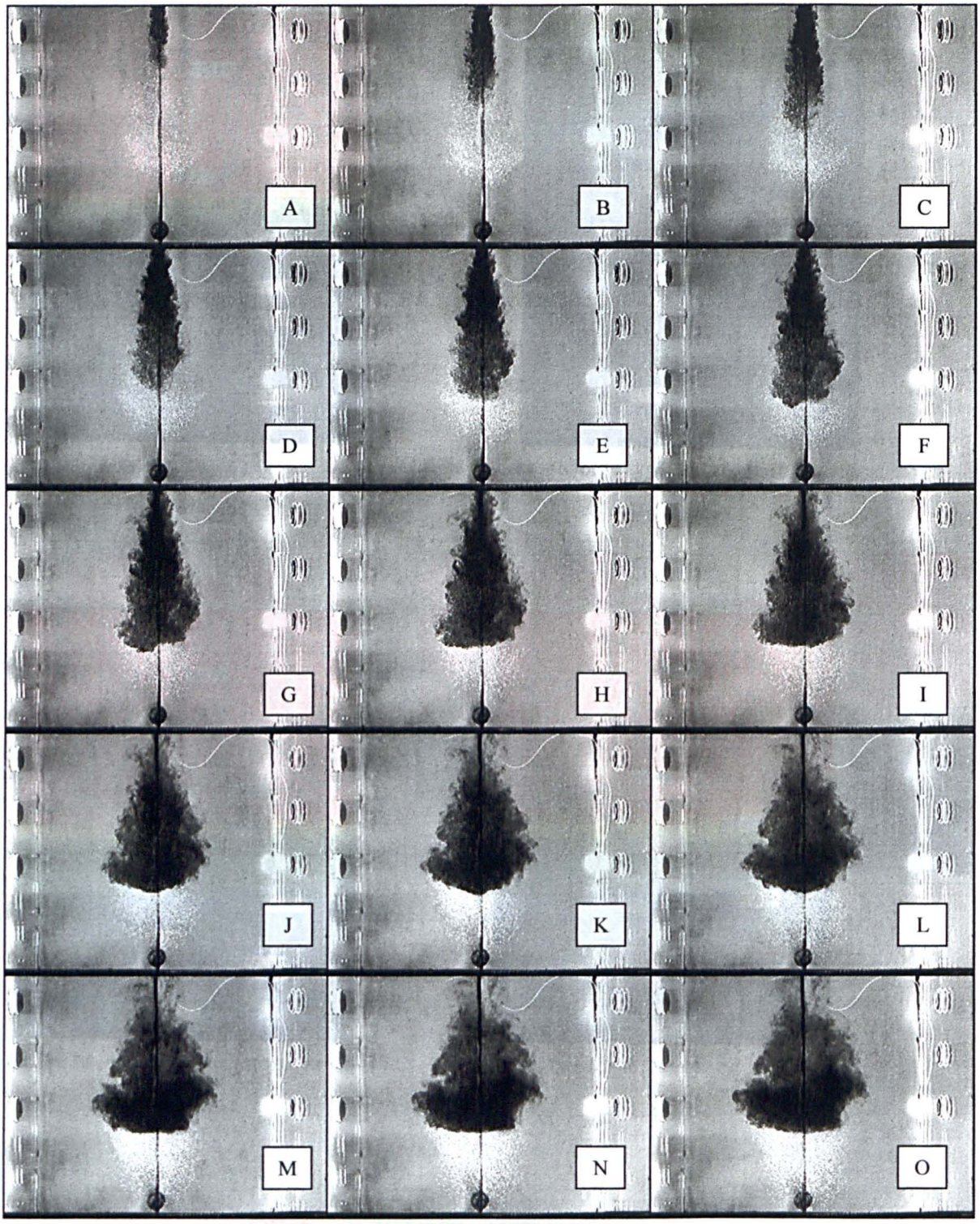

Figure 5.18. Structure of the jet. Experiment 2. Time period between frames: 2s.

Table 5.2. Experimental data for the 10 experiments on the tank.

Experiment	Fr_o	S_o	$d_{o,m}$	Zp, m
7	1.25E+02	1.69E-02	1.00E-02	0.24
9	2.21E+02	8.07E-03	5.00E-03	0.14
10	2.29E+02	1.07E-02	5.00E-03	0.12
4	3.88E+02	8.80E-03	5.00E-03	0.18
3	6.41E+02	7.39E-03	5.00E-03	0.19
2	1.31E+03	8.47E-03	5.00E-03	0.28
1	2.34E+03	1.07E-02	5.00E-03	0.35
5	4.62E+03	4.48E-03	2.50E-03	0.27
8	5.77E+03	5.12E-03	2.50E-03	0.26
6	1.92E+04	4.36E-03	2.50E-03	0.51

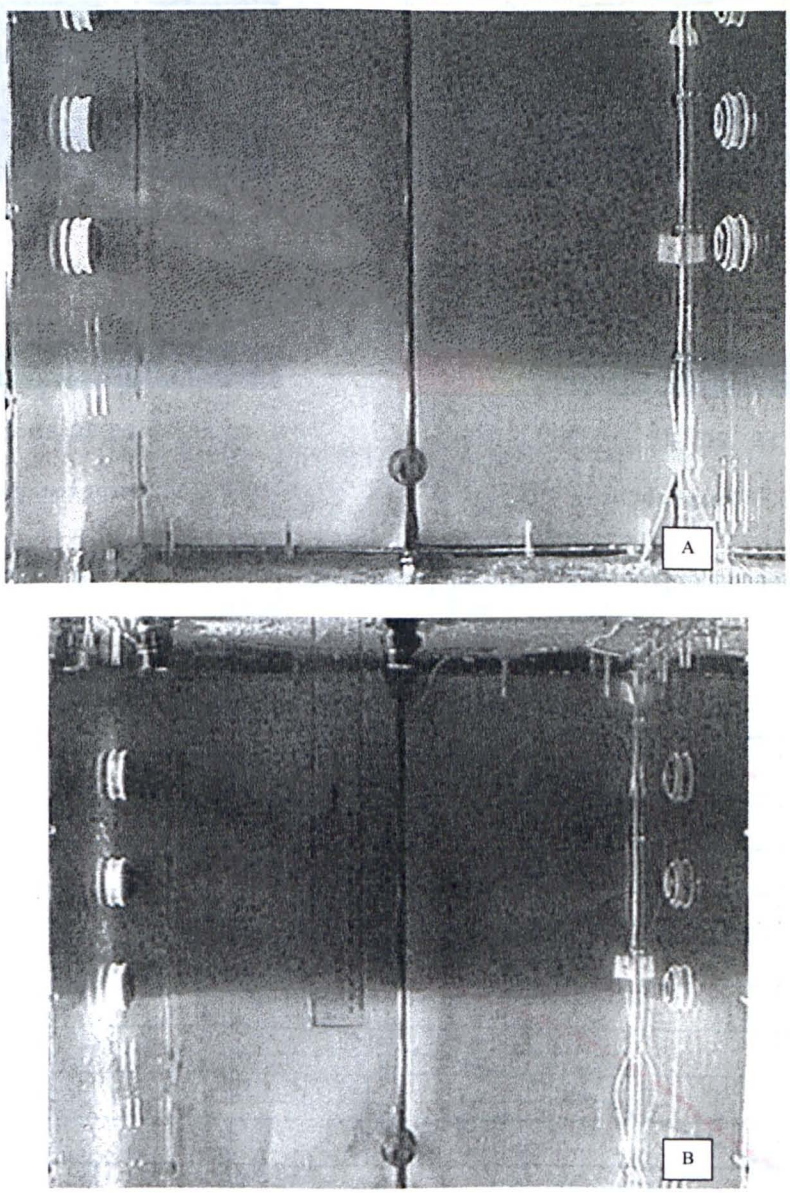

Figure 5.19. Visualization fo the sharp interface. A) Experiment 1; Fro = 2.34x103; So = 4.48x10-3. B) Experiment 5; Fro = 4.62x103; So = 1.07x10-2.

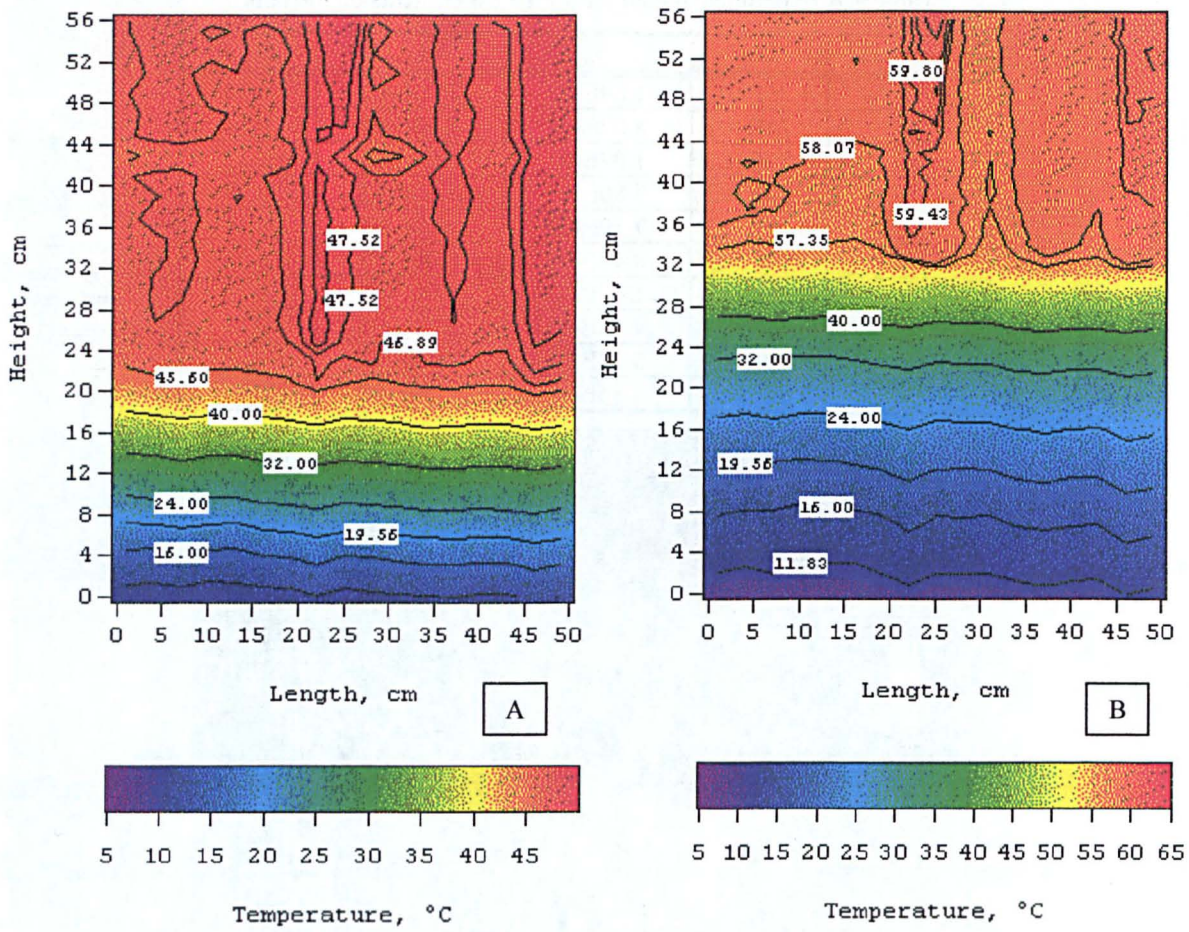

Figure 5.20. Temperature profiles of maximum penetration depth. A) Experiment 1. B) Experiment 5.

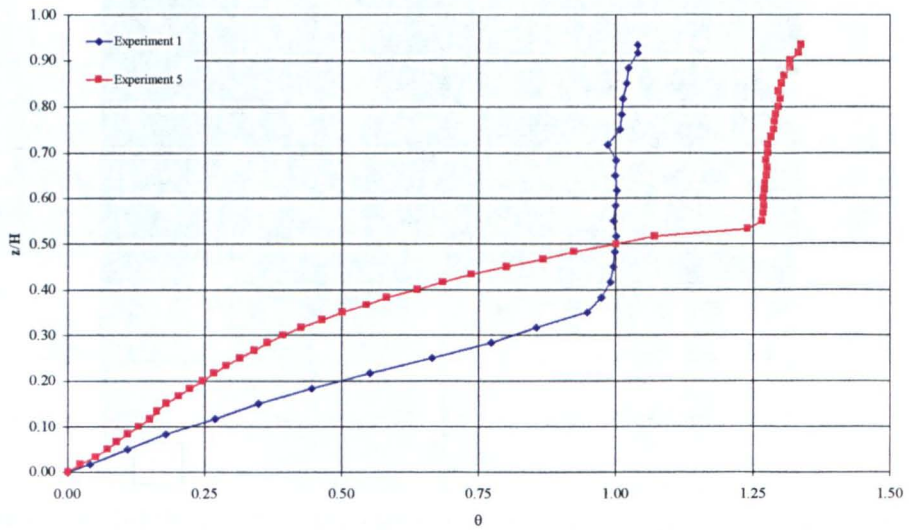

Figure 5.21. Central vertical temperature stratification for experiments 1 and 5.

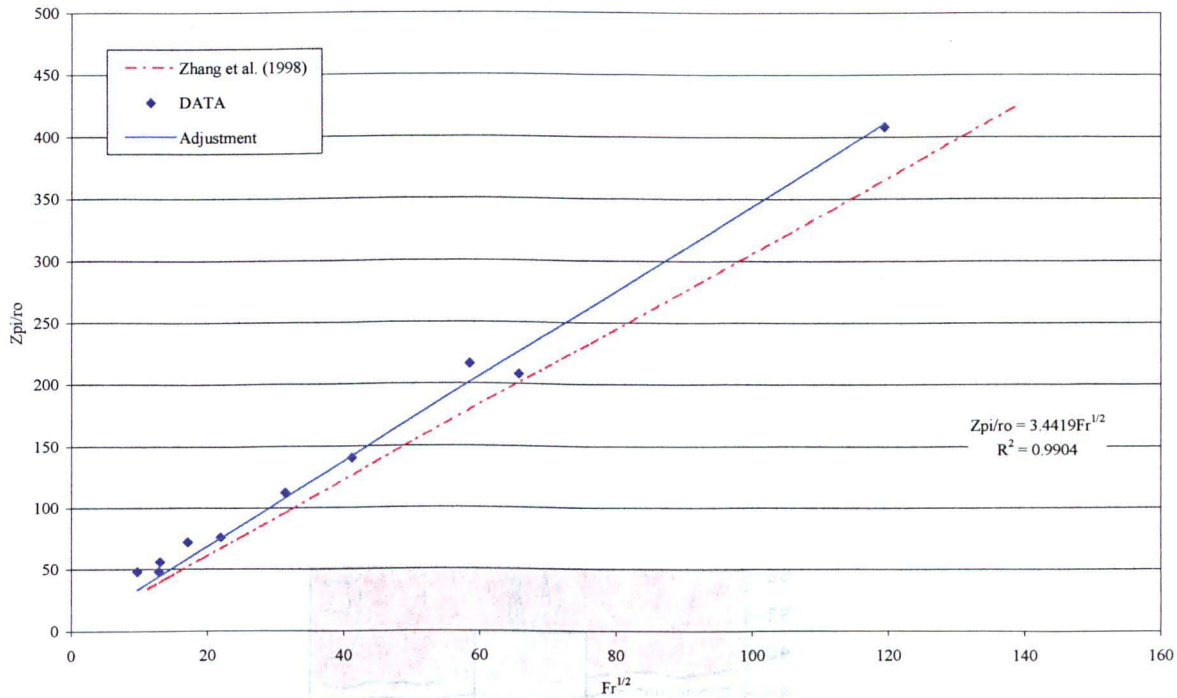

Figure 5.22. Penetration distances as a function of $Fr^{1/2}$.

Table 5.3. Data used to estimate the penetration depth.

BAe conditions	Values
W_o, m/s	13.00
d_o, m	0.30
T_{amb}, °C	20.00
T_j, °C	60.00
β, K^{-1}	3.19E-03
$\Delta T/\Delta z$[1], °C/m	0.25

Table 5.4. Penetration depht in BAe hangar using different correlations.

Source	Zpi, m
Seban *et al.*, 1978	11.15
Day[2], 1990	11.98
Zhang and Baddour, 1998	13.76
This work	15.47

[1] Based in measurements done in February 6th. $\Delta T = T_T - T_B$; $\Delta z = 23$m.

[2] $Zpi = 2.664 r_o Fr^{1/2}$, similar to Turner (1966), Equation 2.1

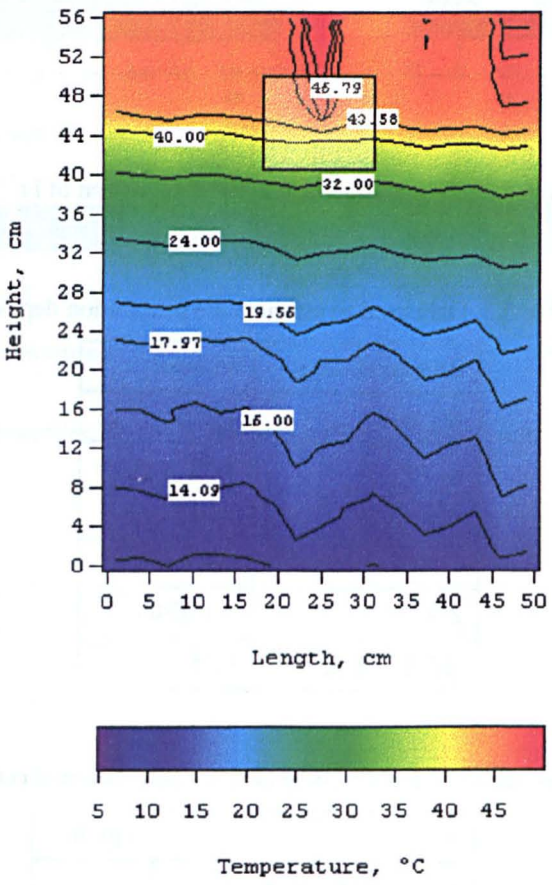

Figure 5.23. Temperature field in experiment 9.

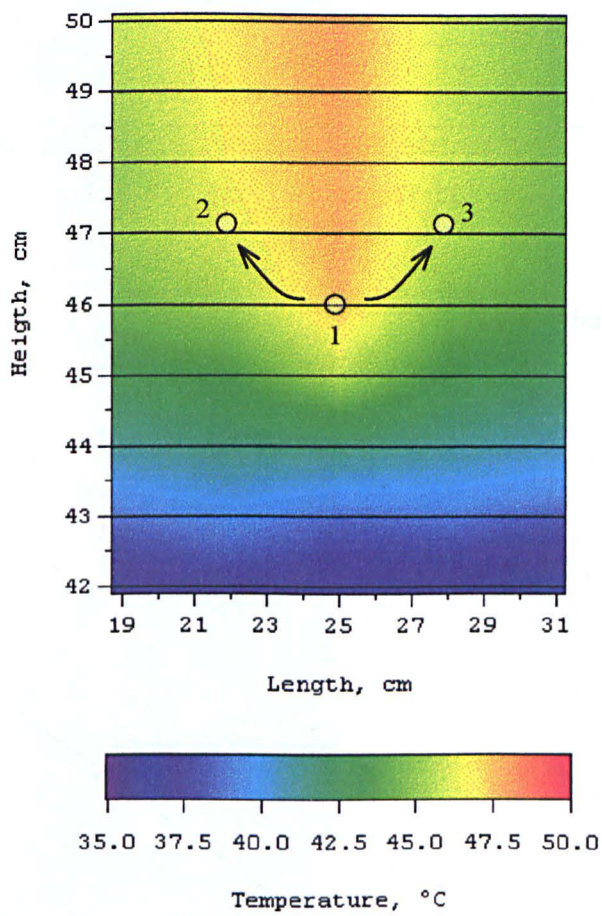

Figure 5.24. Magnification of the experiment 9. Point 1 (L = 25cm, H = 46); Point 2 (L = 22cm, H = 47cm); Point 3 (L = 28cm, H = 47cm).

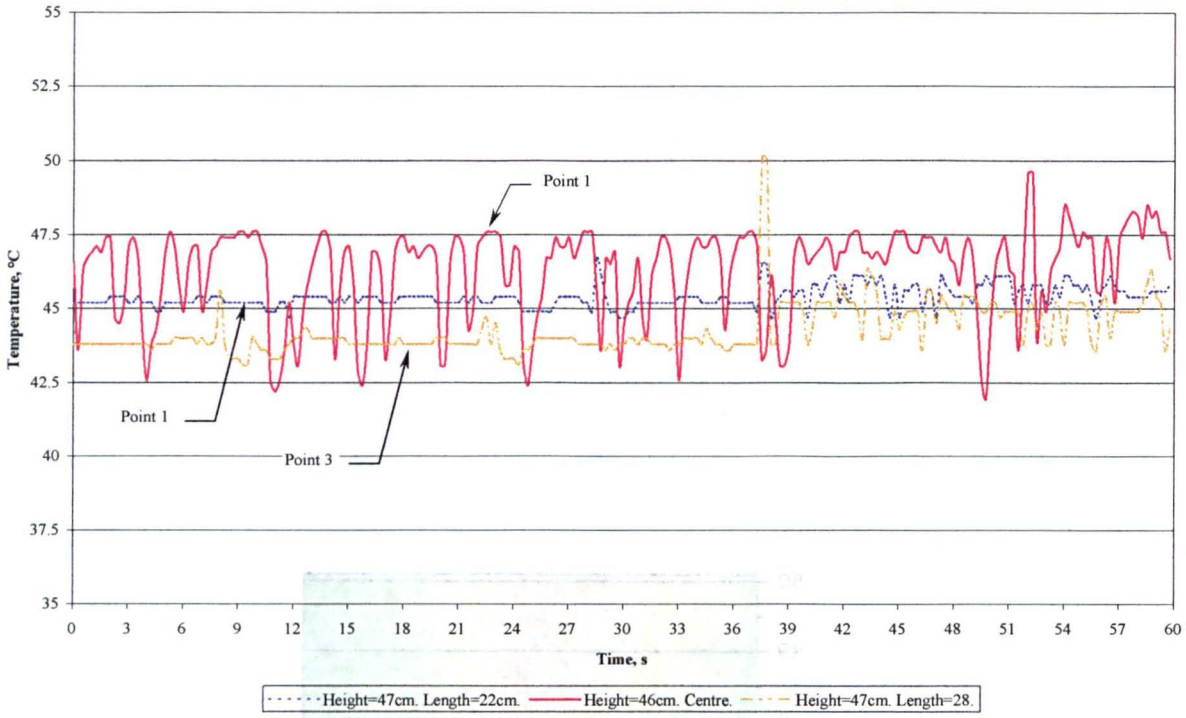

Figure 5.25. Temperature record. $\Delta T = 0.25$s.

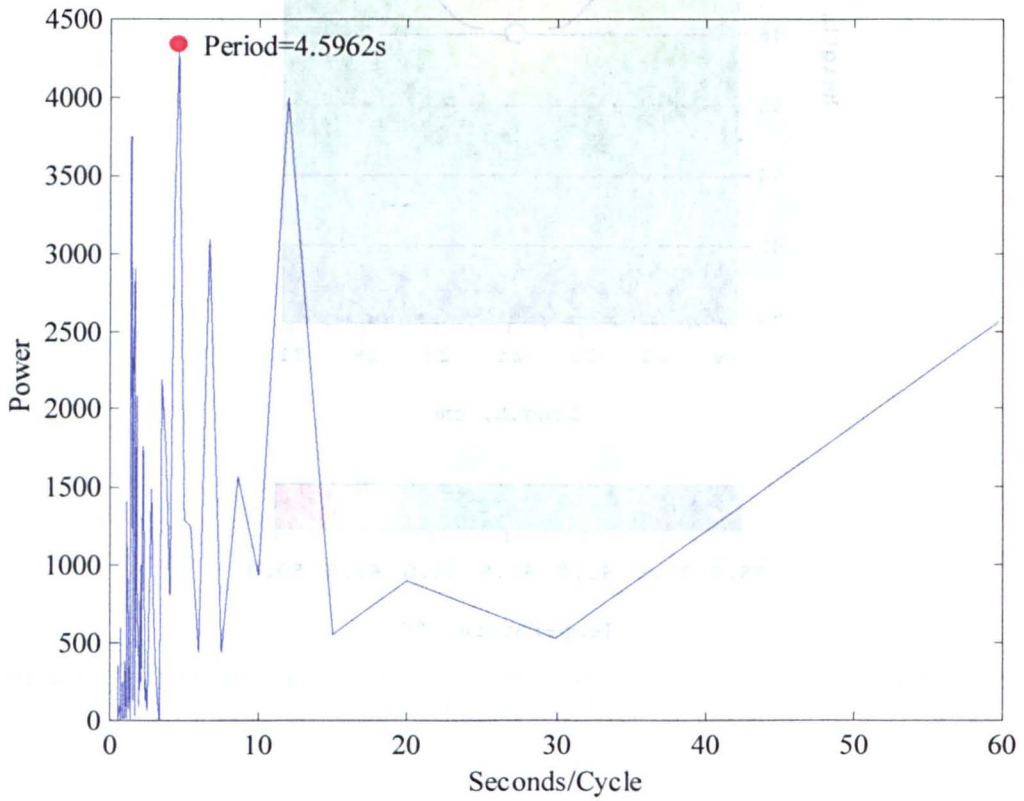

Figure 5.26. Fast Fourier transformation for temperature at the centre in experiment 9 at heigth =46cm.

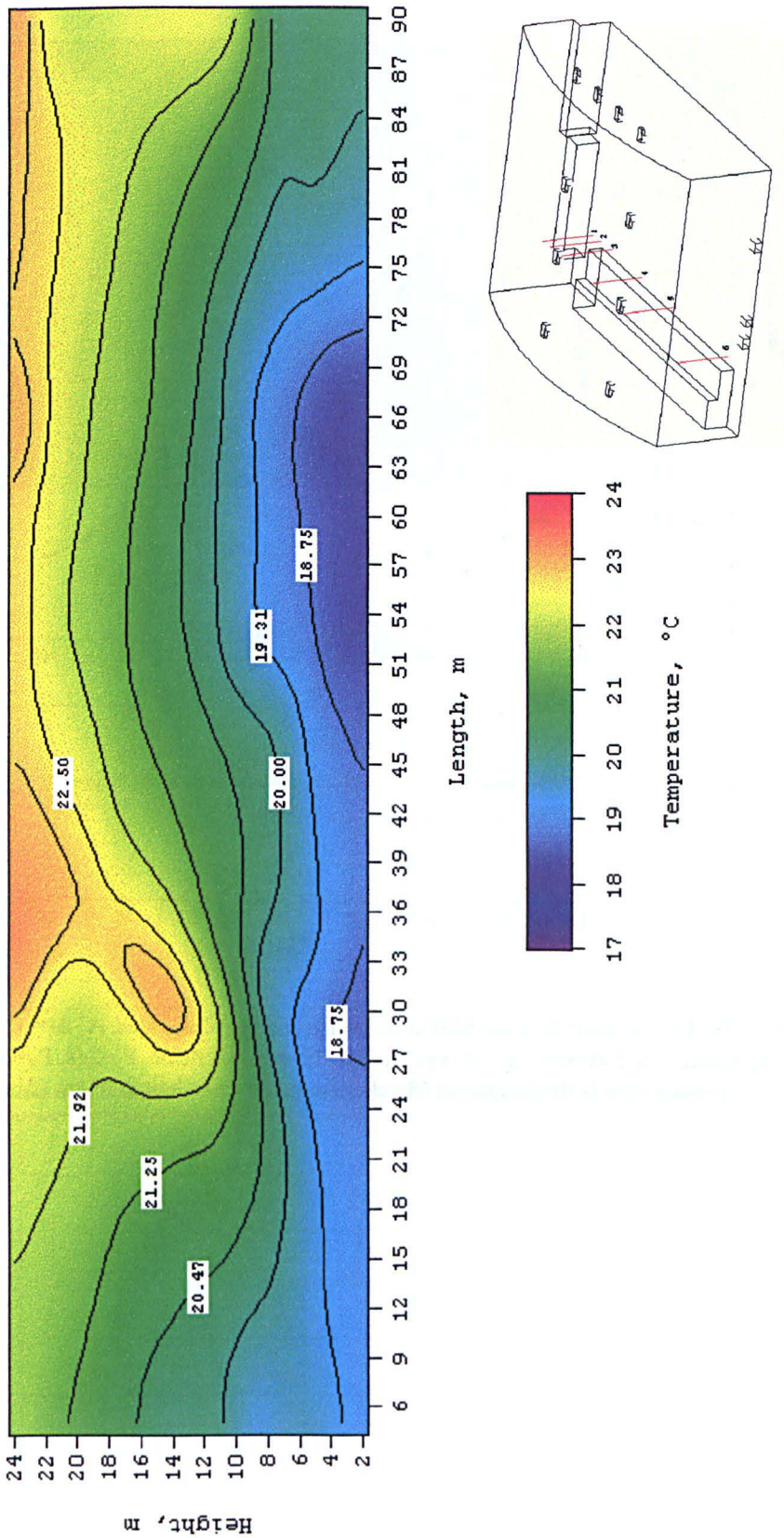

Figure 5.27. Temperature field in the hangar on March 19. The hangar drawing shoes points from 1 to 6. Interpolated data.

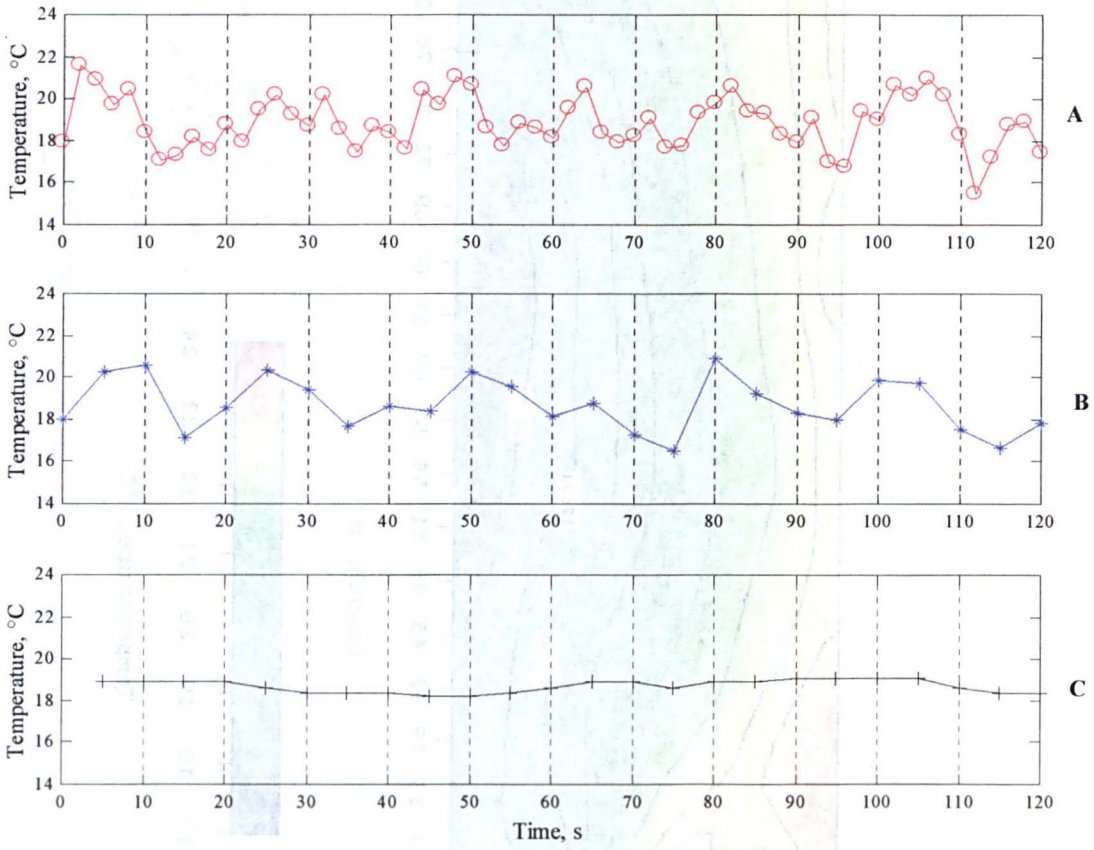

Figure 5.28. Temperature data sampled at two different sampling rates. A) Δt=2s; B)Δt=5s. The generating function is $T(t)=\sin(2\Delta t/P_1)+\sin(2\Delta t/P_2)+19+$random noise. P_1=24s; P_2=20s. C) Measured temperature in the hangar on March 19 at point 4 at a heigth of 8m (Δt=5s).

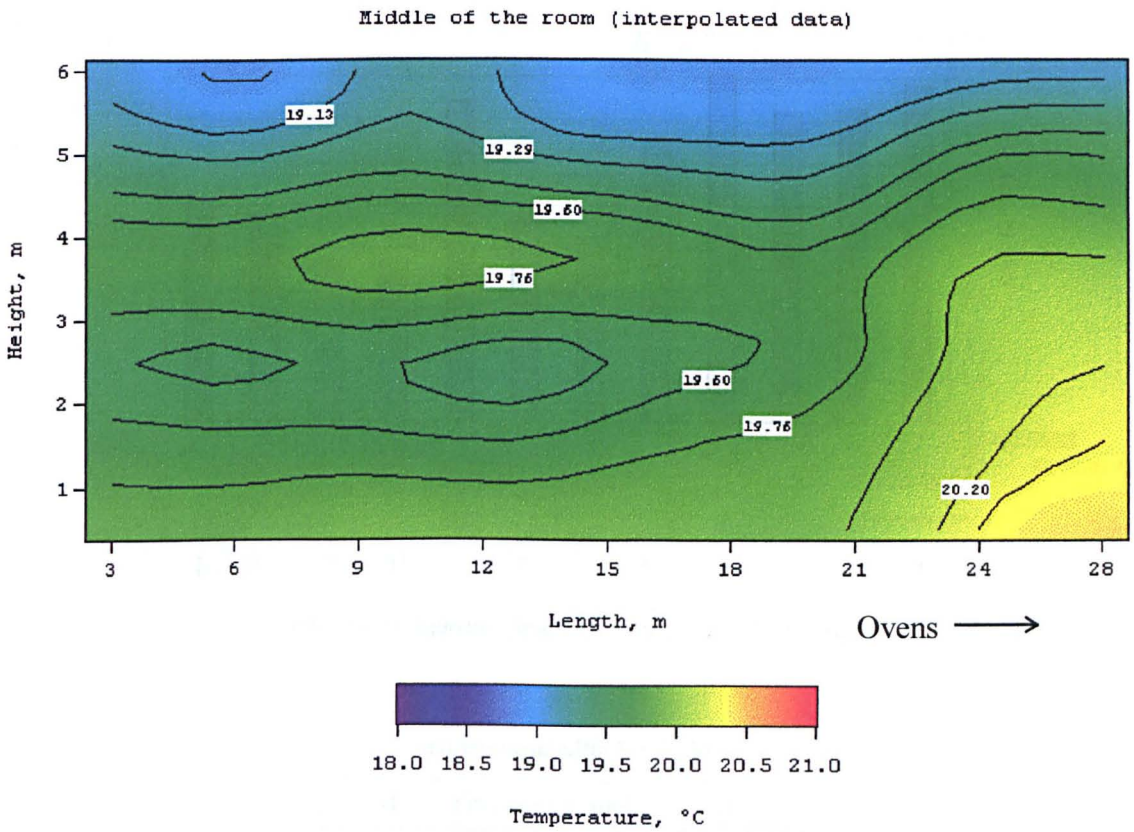

Figure 5.29. Temperature profiles at the middle of the room.

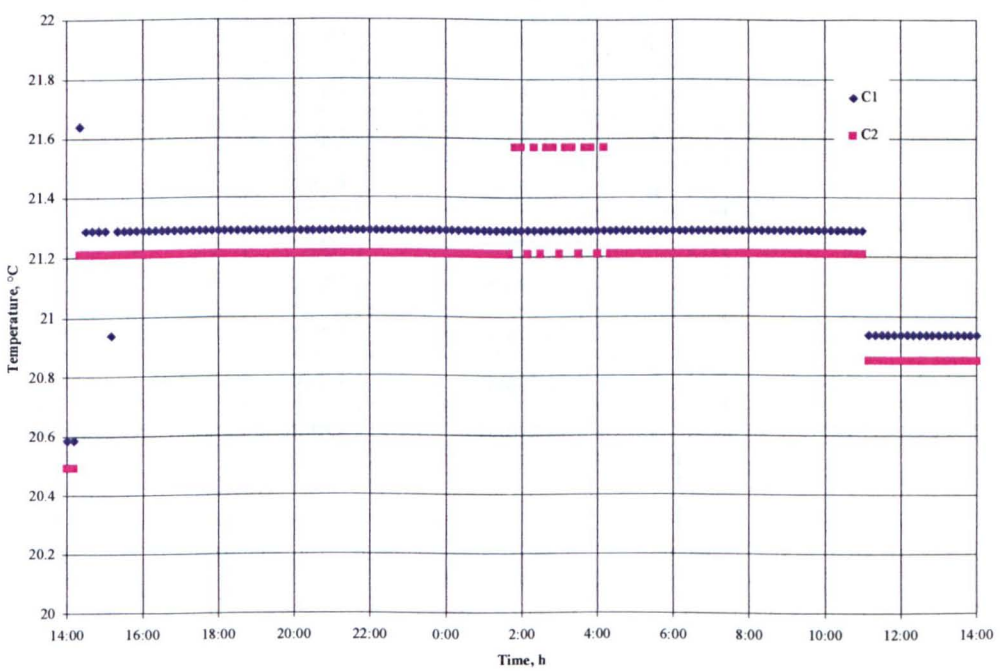

Figure 5.30. Temperature variation inside the maturing room.

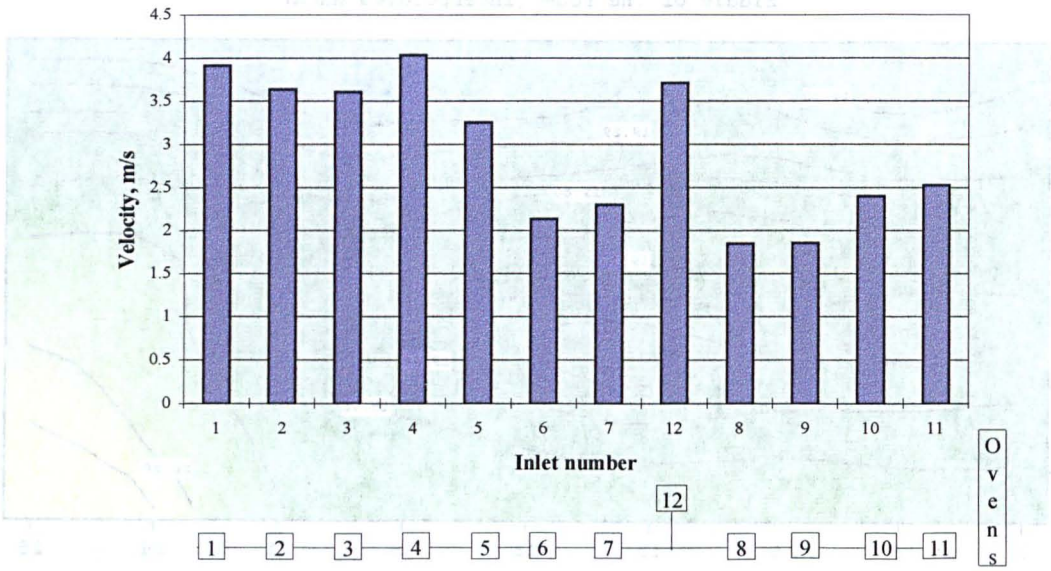

Figure 5.31. Measured air velocity through room inlets.

Table 5.5. Outlet arrangement.

Outlet	Bottom (damper)	Top
a	Close	Open
b	¾ Open	Open
c	Open	Open
d	Close	Open
e	¼ Open	Open
f	Close	Open
g	½ Open	Open
h	½ Open	Open
i	¼ Open	Open
j	¼ Open	Open
k	½ Open	Open
l	½ Open	Open

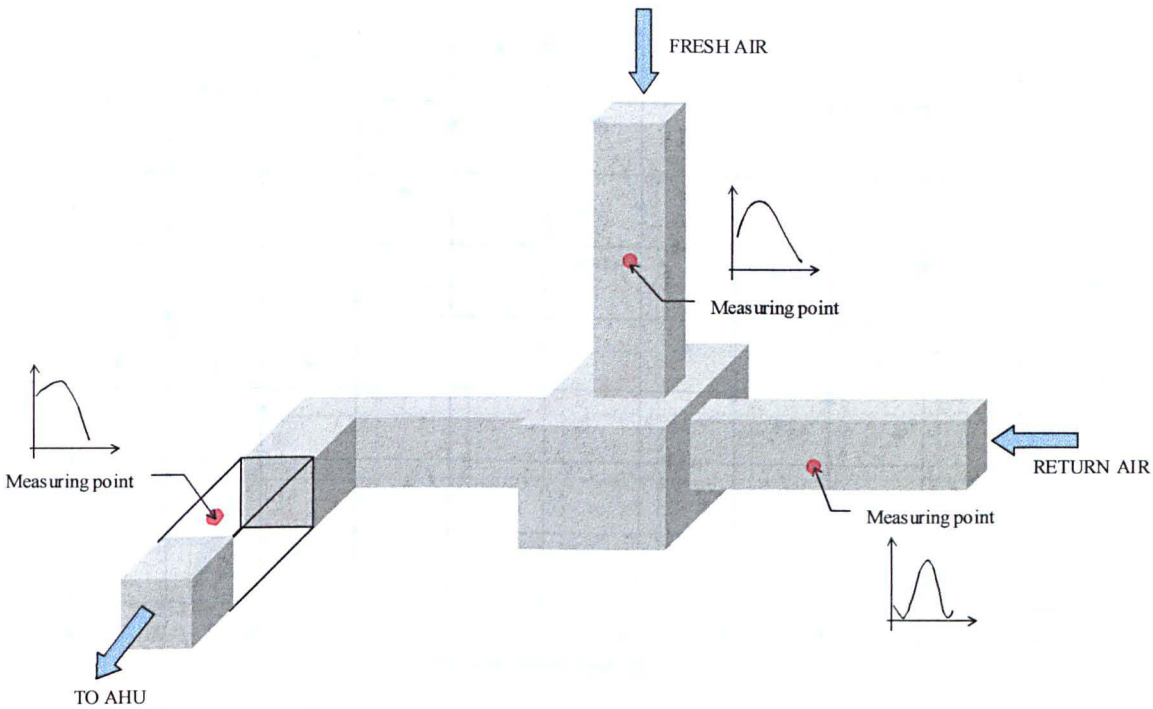

Figure 5.32. Sketch of the ancillary ductwork with the location of the measuring points.

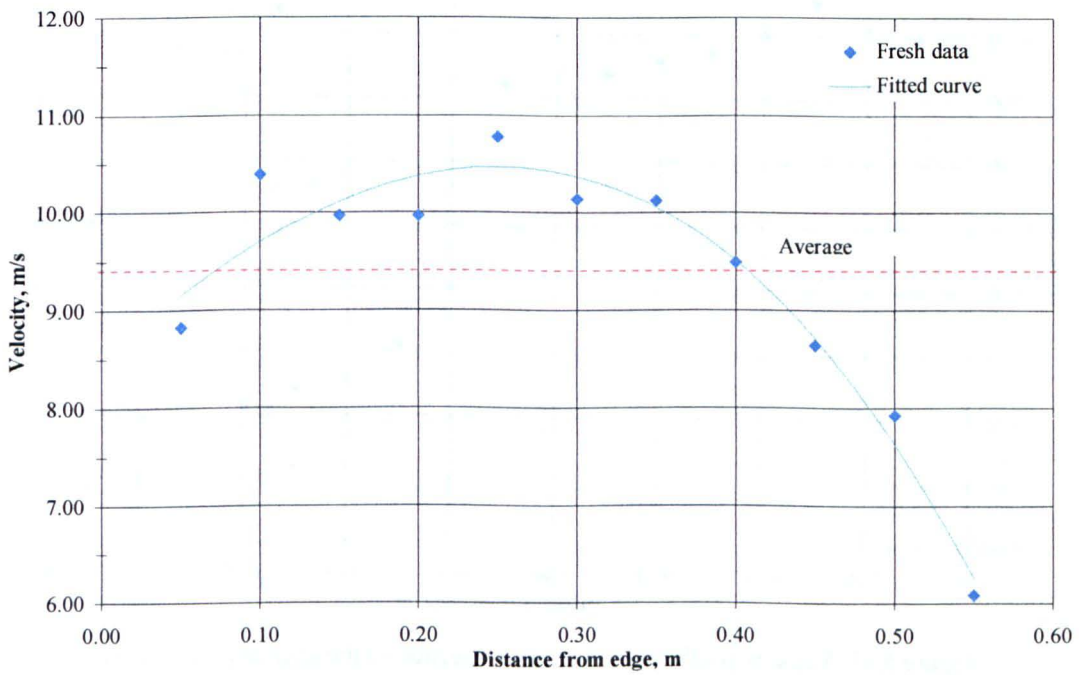

Figure 5.33. Velocity profile in the fresh air section of the ancillary duct work.

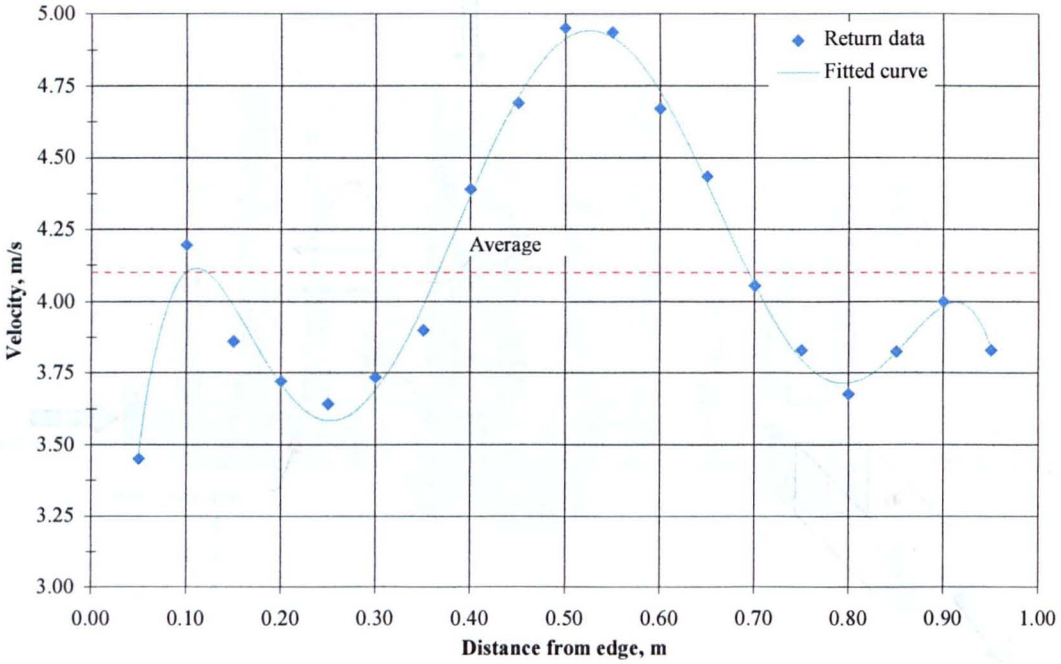

Figure 5.34. Velocity profile in the return air section of the ancillary duct work.

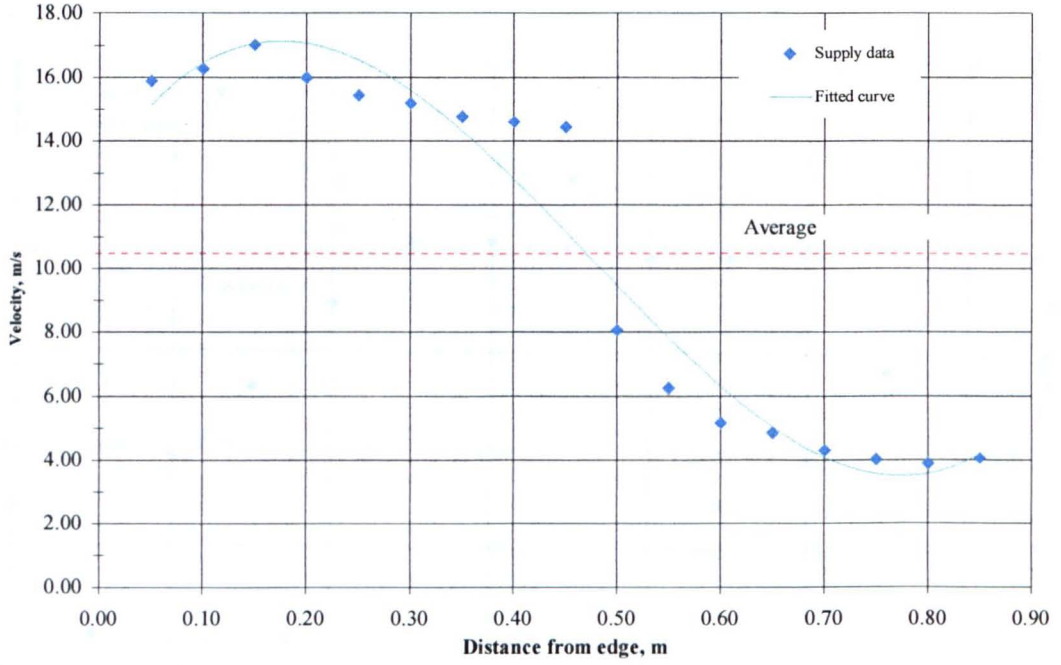

Figure 5.35. Velocity profile in the supply air section of the ancillary duct work.

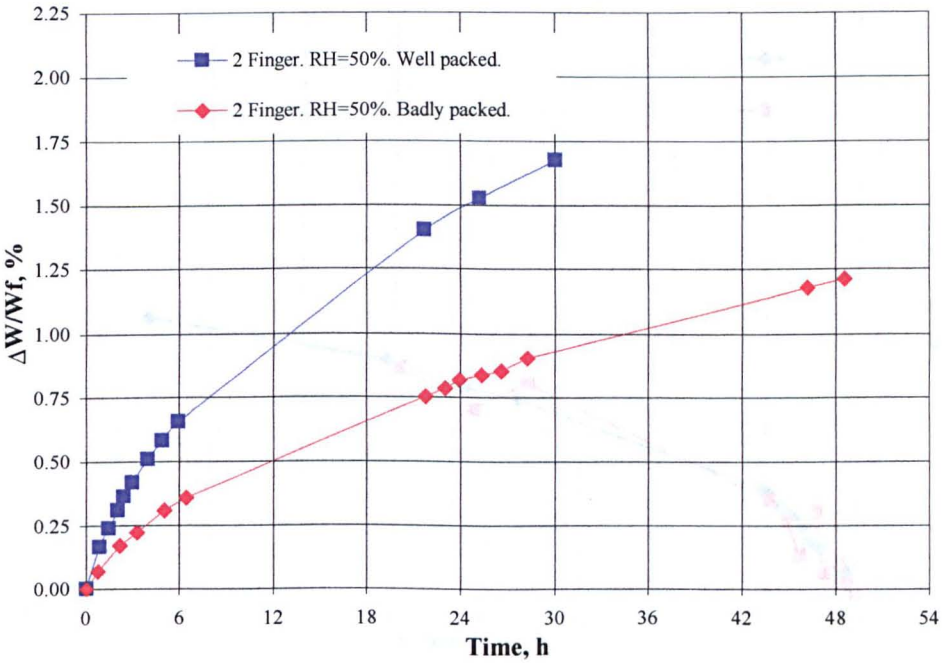

Figure 5.36. Moisture uptake 2 Finger (RH=50%).

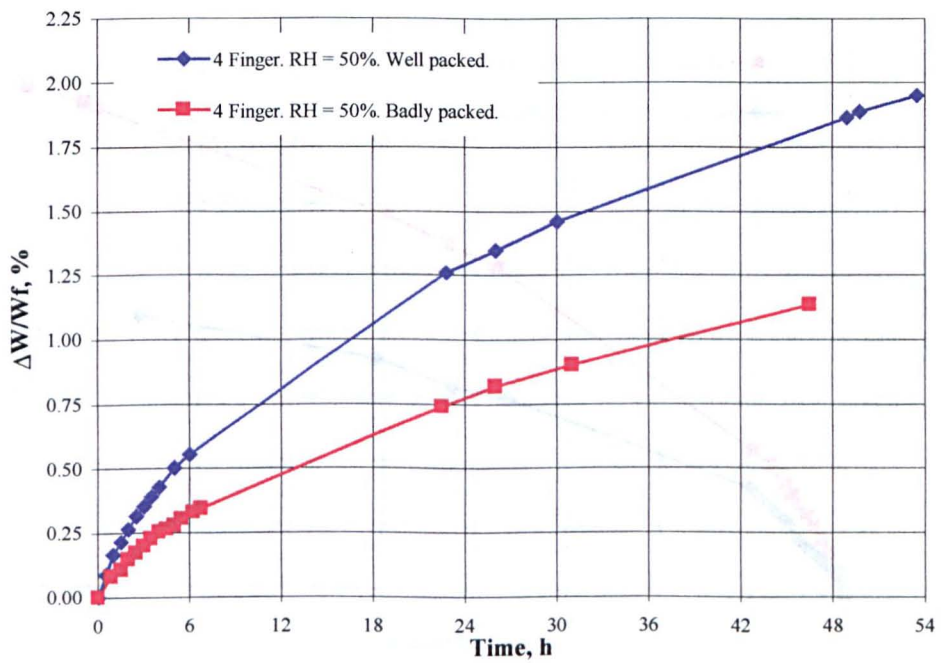

Figure 5.37. Moisture uptake 4 Finger (RH=50%).

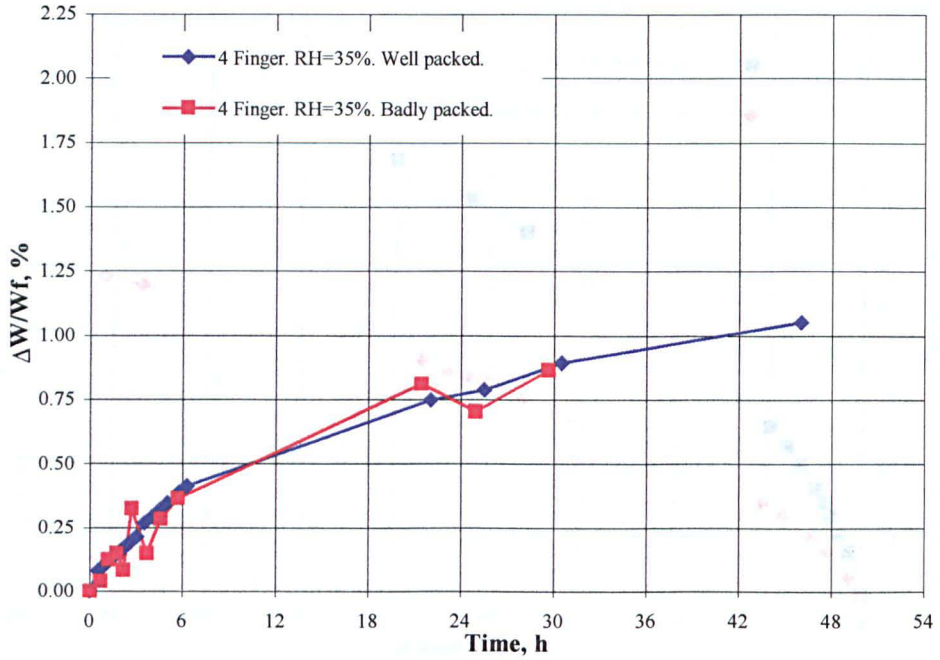

Figure 5.38. Moisture uptake 4 Finger (RH=35%).

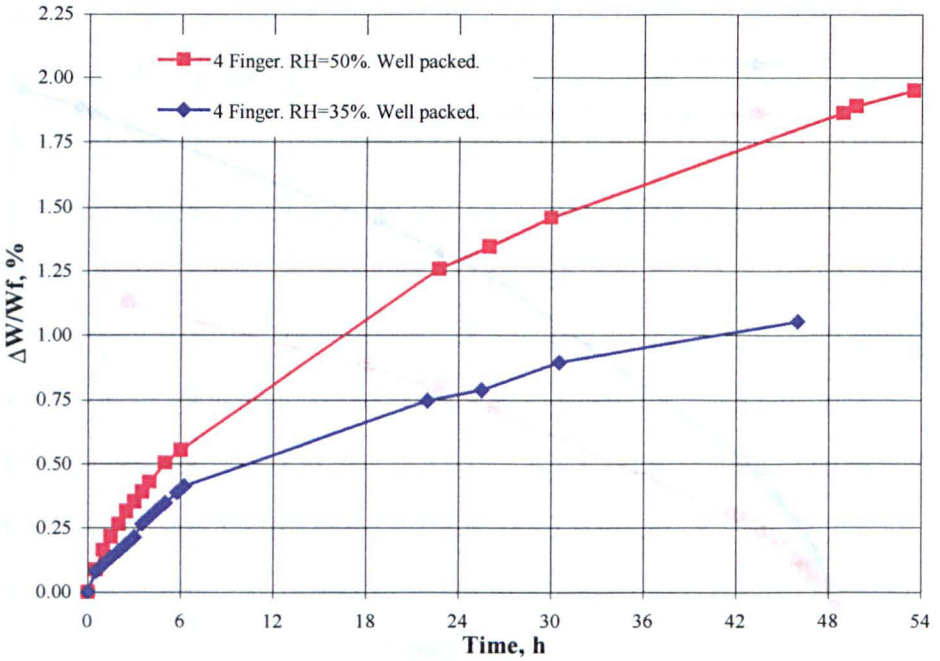

Figure 5.39. Comparison of moisture uptake of 4 Finger at two different relative humidities.

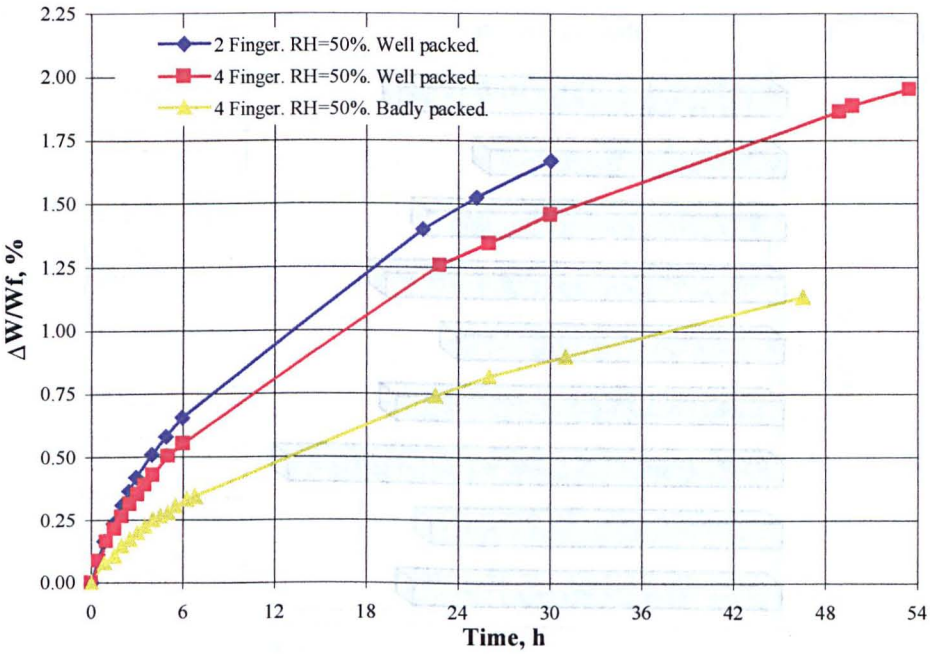

Figure 5.40. Moisture absorption for different wafer arrangements and packing techniques.

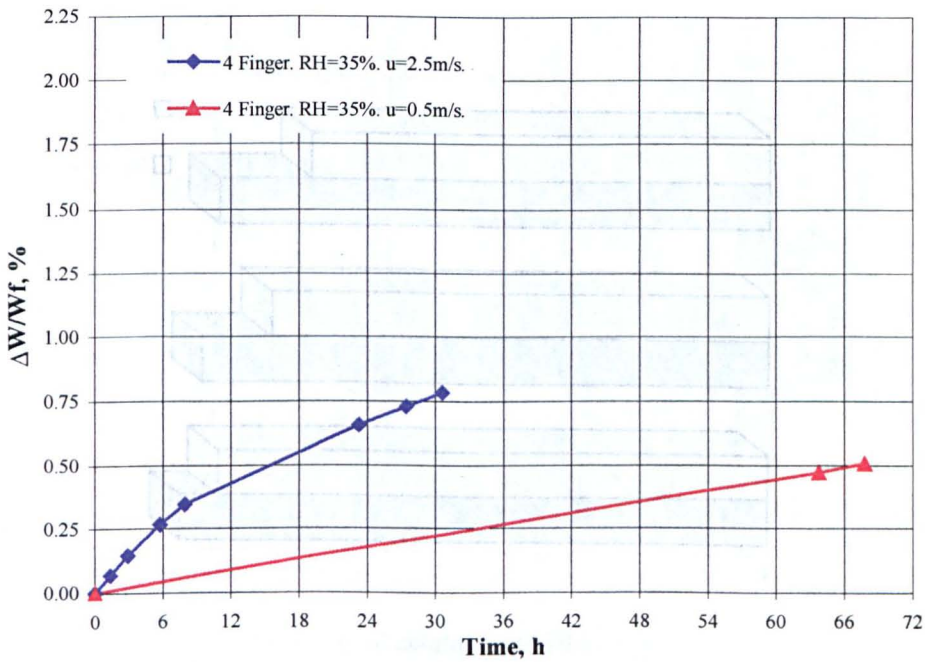

Figure 5.41. Moisture uptake at different ambient velocities.

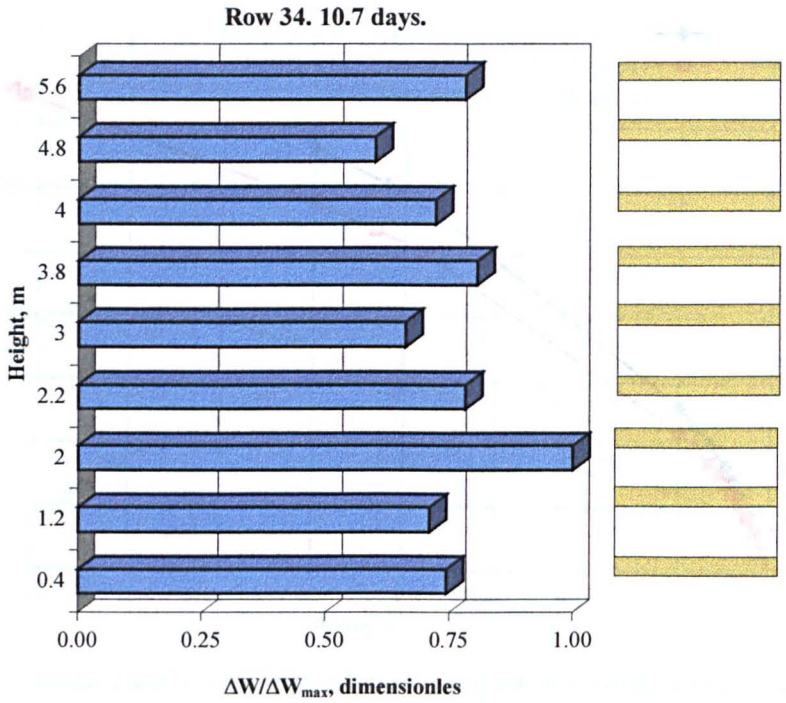

Figure 5.42. Vertical moisture uptake by silicagel in the room.

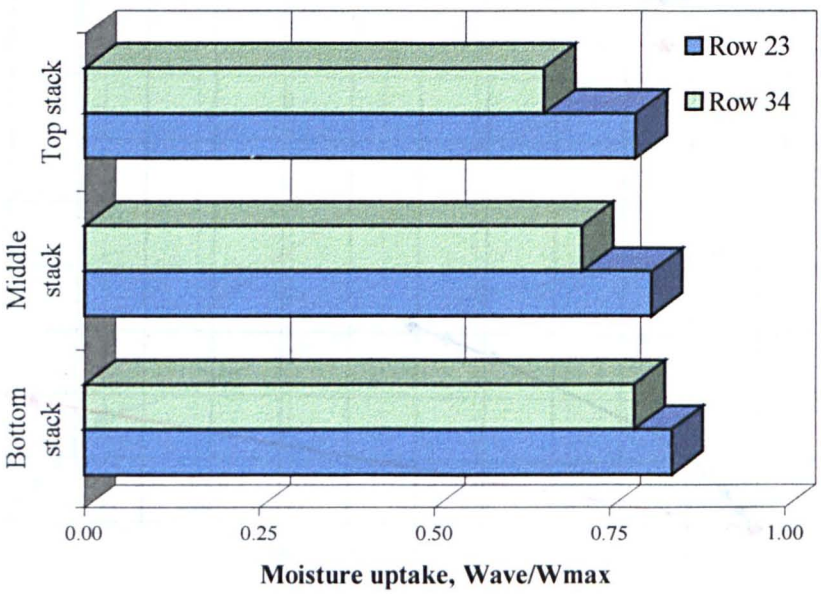

Figure 5.43. Average moisture uptake in the vertical direction for two positions in the room (1 day).

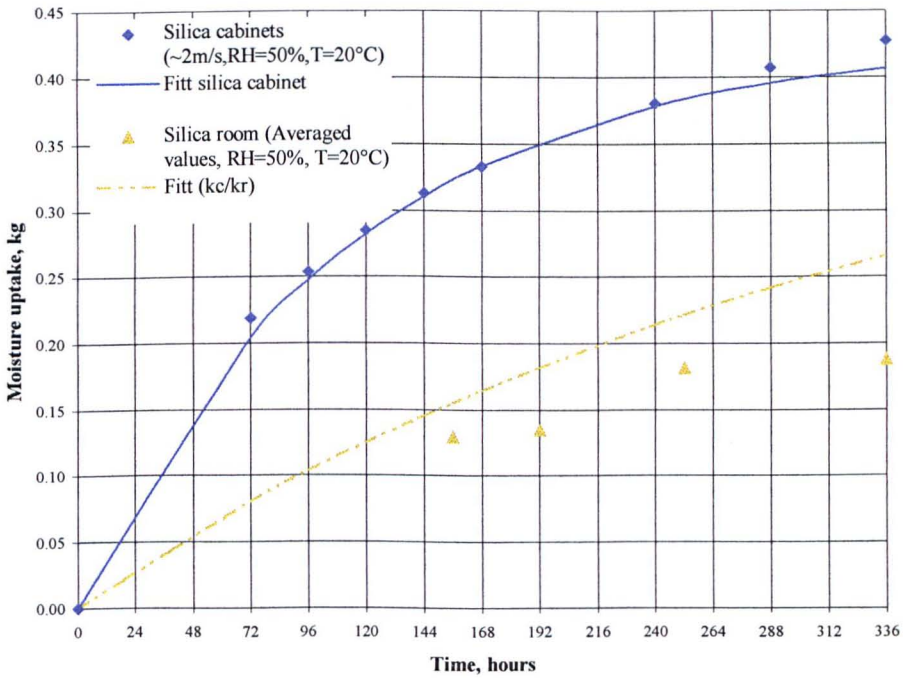

Figure 5.44. Normalisation of silicagel data.

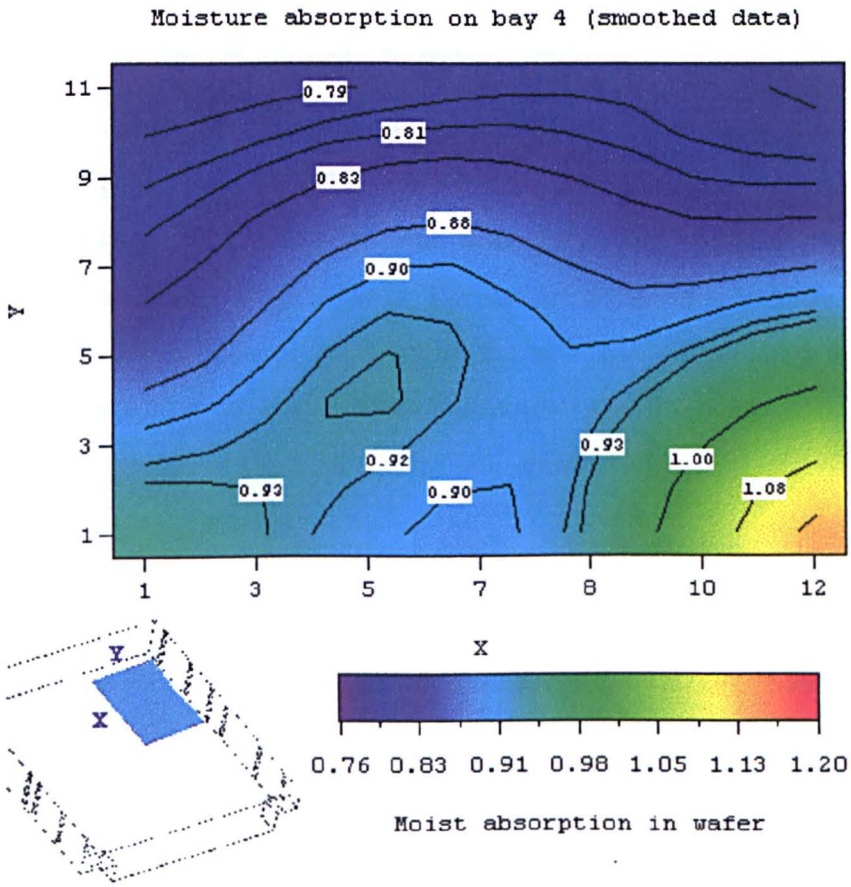

Figure 5.45. Moisture absorption.

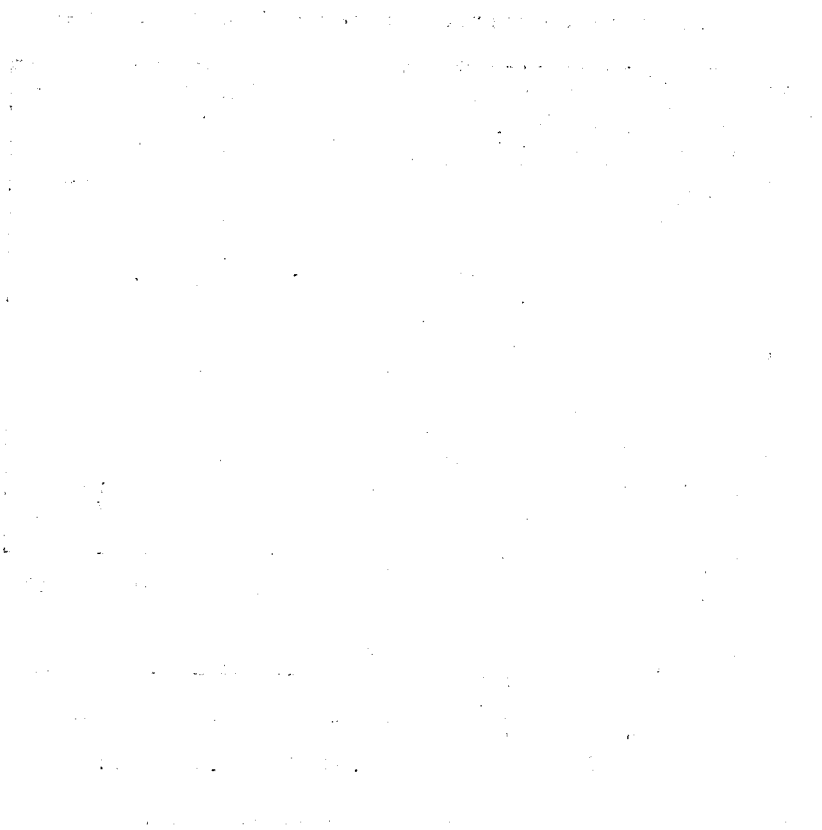

6 MODEL IMPLEMENTATION

6.1 Introduction.

The mathematical modelling used for moisture; moisture absorption and fluid age is described, as well as the assumptions made to simulate porous flow and anisotropic resistance to the flow. Also, this chapter presents a description of the computational grid and the different scenarios that have been tested.

6.2 Buoyancy affected flows.

The complex behaviour of the velocity and temperature field within the hangar was modelled by assuming that the imposed boundary conditions stay constant.

A body fitted grid divided in 36 blocks was used to create the computational geometry of the hangar, Figure 6.1. The first set of 12 blocks have a non-uniform mesh distribution to obtain a finer grid in the zone were the thermal inversion was observed. The second set has a rectangular geometry. The last set has a curve to simulate the dome of the hangar. The geometry was divided with the objective of reducing the number of distorted volume cells near the dome. The total number of cells is 384,384. Finally, The buildings inside the hangar were simulated as non-conducting solids.

6.2.1 Boundary conditions.

In order to model different scenarios inside the hangar, four cases with different boundary conditions were considered. The first scenario attempt to model the conditions monitored on March 19 where all the heaters were in operation, the doors closed and the rest of the hangar was sealed except for the top gap between the hangar. The gap was set as a pressure boundary.

To simulate the open doors scenarios a pressure boundary has been set at the front of the hangar; otherwise the boundary condition at the front of the hangar were set as a walls. Table 6.1 and Table 6.2 summarise these cases.

Heaters H1 to H4 and H9 to H10 are considered as inlets with temperature values of 45°C. Heaters H5 to H8 are considered as momentum sources with a heat source. The heat output for H5 and H7 is 100kW, whilst for H6 and H8 is 300kW (Dane, G.E. 1991). The tall boys are considered as momentum sources.

6.3 Porosity affected flows.

The storeroom was modelled assuming that we can fill it instantly with fresh product. The space with product was considered as porous with an extra resistance to the flow in the vertical direction. These porous regions absorb water vapour from the air and are represent as sink terms. The mass transfer between the air and the product is calculated by way of the heat and mass transfer analogy and coefficients estimated by experiments. The modifications made to the code will be explained next.

The computational grid developed for the storeroom geometry consists of 7 blocks and a total of 295200 control volumes. A non-uniform mesh distribution has been used to generate the grid with finer resolution in the inlet and outlet regions. As result we obtained a refined grid at the walls and at the centre of the computational domain, as shown in Figure 6.2. In this figure, the void spaces at the front correspond to office rooms, and have been treated as solids.

Four scenarios have been modelled, as described in Table 6.3. In scenario 2, experimental distribution on outlets refers to the data presented in Table 6.4. For scenario 3 the effect of installing 20 recirculation units is explored whilst in scenario 6 the added effect of a good packaging technique is considered. The number of air changes per hour for all scenarios is 4. Figure 6.3 presents a sketch of the flow in the storeroom for scenario 2.

In scenarios 3 and 4 a momentum source has been set for each of the recirculation units, Figure 6.4. The value of the momentum source, *Ms*, in the code was calculated as follows:

$$Ms = \frac{u^2 \rho A_c}{V_c}.$$

Here u is the mean velocity expected in the recirculation unit, A_c is the cross sectional area of the recirculation unit and V_c is the volume of the cell where the momentum source is going to be placed within the computational grid. Since the desired volumetric

flow that each of those units handle is $1m^3/s$, the approximated cross sectional area is $0.12m^2$ and the approximated volume of the cell is $0.024m^2$. The value of the momentum source is $405.83N/m^3$.

6.3.1 Fluid age

A ventilation system can be described as the way inlets and outlets are located in a space in order to distribute a fluid. The manner and efficiency with which the fluid is replaced at each point in a space is called 'ventilation effectiveness' (Murakami S. 1992).

One way of analysing the effectiveness of a ventilation system is by using the concept of 'fluid age'. This is set to zero as a fluid particle enters a ventilated enclosure but increases as the particle is advected through the enclosure towards the outlet. Fluid age may be computed in CFD by modifying the differential form of the generic conservation equation presented in Chapter 3. For a steady state problem, assuming zero diffusion, and if the passive scalar is taken to be the age of the fluid denoted t_a, that equation can be written as:

$$\rho\left(u_i \frac{\partial t_a}{\partial x_i}\right) = S. \qquad 6.1$$

At the inlet register $t_a = 0$.

In order to maintain dimensional consistency, the source term is set equal to the density ρ to give:

$$\rho\left(u_i \frac{\partial t_a}{\partial x_i}\right) = \rho. \qquad 6.2$$

In principle, the age of the fluid within a recirculation zone where the fluid is completely 'trapped' should be infinity. However, due to the existence of numerical diffusion this limiting condition will never be predicted correctly despite the fact that the diffusivity terms have been set to zero.

6.3.1.1 Figure of merit for fluid age

In a perfect 'piston' flow system the elements entering the enclosure at the same instant in time move through it with constant and equal velocity on parallel paths. For this type of flow it is possible to show that in a steady state, the mean fluid age at the outlet

position (mean residence time of the air), t_o, is always equal to the nominal time constant of the ventilating system (mean turnover time), $\bar{t}$, defined as:

$$\bar{t} = \frac{V}{\dot{V}} = t_o, \qquad 6.3$$

where V, is the total volume of the space, and $\dot{V}$ is the volume flow rate (Levenspiel O. 1972). Also, it can be demonstrated that the mean fluid age within the system, t_m, is equal to one half of the mean fluid age at the outlet (Sandberg and Sjöberg 1983). In practise, however, this ideal ventilating system is never achieved. Outside the principal flow stream, there are stagnant or recirculation zones where the air volume is not being efficiently advected through the system. In such zones, the fluid residence time will increase. Hence, in 'real' ventilation systems, the mean fluid age is always greater than half the outlet fluid age:

$$t_m \geq \tfrac{1}{2} t_o . \qquad 6.4$$

The figure of merit presented in this work, and named Index of Ventilation Performance (IOVP), relates the average 'age' to the 'age' at the outlet:

$$\text{IOVP} = \frac{1}{2}\left(\frac{t_o}{t_m}\right). \qquad 6.5$$

If the elements of fluid that enter the vessel move through it with constant and equal velocity on parallel paths and leave at the same moment, this type of behaviour is called plug flow situation. For perfect plug flow IOVP = 1. If, on the other hand, the fluid is completely mixed, its properties are uniform and identical with those of the outgoing stream. For perfect mixing IOVP = 0.5. Both behaviours are illustrated in Figure 6.5.

6.3.2 Flow in porous media

The Darcy law is the mathematical expression of numerous experimental observations. This empirical law states that the volume-averaged fluid velocity through a column of porous material is proportional to the pressure gradient established along the column. Further experiments proved that the volume-averaged velocities are, in addition, inversely proportional to the viscosity, μ, of the fluid seeping through the porous material. To apply the averaging process the porous volume must be large enough to contain a number of solids distributed at random. In other words, if we were talking of a bed of rocks, we must have a large flow pattern flowing through relatively small pebbles.

The Darcy observations can be written as:

$$u_i = \frac{K_i}{\mu}\left(\frac{-\partial p}{\partial x_i}\right), \qquad 6.6$$

where K_i is an empirical constant called permeability and is function of the available volume to flow and the solid size.

In the code, it is assumed that 'infinitesimal' control volumes and surfaces are large relative to the interstitial spacing of the porous medium, though small relative to the scales that we wish to resolve. Thus, given control cells and control surfaces are assumed to contain both solid and fluid regions. The current version of the code allows isotropic media and the user should in fact only set the volume porosity.

The volume porosity, γ, at a point is the ratio of the volume, V', available to flow in an infinitesimal control cell surrounding the point, and the physical volume, V, of the cell. Hence

$$V' = \gamma V. \qquad 6.7$$

The values used in this work for volume porosity for the 2 and 4 finger arrangements are 0.22 and 0.04 respectively. For the case of 2 and 4 well packed finger trays the volume porosity is 0.32 and 0.16, respectively. Figure 6.6 shows the zones with different porosity within the CFD model.

In particular, the equations for conservation of mass and momentum are:

$$\rho\gamma\frac{\partial u_j}{\partial x_j} = 0; \qquad 6.8$$

$$\rho\gamma u_j\frac{\partial u_i}{\partial x_j} = \frac{\partial}{\partial x_j}\left[2\gamma D_{ij}(\mu+\mu_t)\right] - \gamma R_{ij}u_j - \gamma\frac{\partial p}{\partial x_j} + \gamma S. \qquad 6.9$$

Here R_{ij} is a diagonal matrix and represents a resistance to flow in the porous medium and accounts for possible anisotropies in the resistance. In the limit of large resistance, a large adverse pressure gradient must be set up to balance the resistance. In that limit, the two terms on the R.H.S. of Equation 6.9 are both large and have opposite sign, and the convective and diffusive terms on the L.H.S. are negligible. Hence Equation 6.9 reduces to:

$$u_j = -R_{ij}^{-1}\frac{\partial p}{\partial x_j}. \qquad 6.10$$

Hence, in the limit of large resistance, we obtain an anisotropic version Darcy's law, with permeability proportional to the inverse of the resistance tensor. However, unlike Darcy's law, we are working with the actual fluid velocity components u_j, which are discontinuous at discontinuities in porosity.

In order to simulate anisotropy in the horizontal direction a resistance value was estimated using the Ergun equation (Middleman S. 1998):

$$\frac{\partial p}{\partial x_j} = -\left[\frac{150(1-\gamma)^2\mu}{D_p^2\gamma^3} + \frac{1.75\rho(1-\gamma)}{D_p\gamma^3}|u_j|\right]u_j, \qquad 6.11$$

In Equation 6.11, the term in square brackets accounts for the resistance tensor, which can set within the code for the three directions of the flow. The largest resistance is set in the vertical direction.

The pressure drop-flow rate relationship for flow through a packed bed is similar to that for a fully developed flow through a straight tube. The equivalent diameter of the tube will be based on the 'hydraulic radius' concept. The 'hydraulic radius' is the ratio of the cross sectional area of the tubes to the wetted perimeter, we can write it as:

$$r_h = \frac{\text{cross section open to flow}}{\text{wetted perimeter}} = \frac{\text{void volume / bed volume}}{\text{wetted perimeter / bed volume}}$$

If we define the 'hydraulic diameter' as $D_p = 2r_h$ we obtain:

$$D_p = \frac{2\gamma V_B}{A_w}, \qquad 6.12$$

where A_w is the wetted surface of the tray and V_B is the volume of the bed, Figure 6.7. The values of these parameters for the wafer arrangements are shown in Table 6.5.

6.3.3 Moisture.

The distribution of moisture in the air within the maturing room was calculated by applying the steady state concentration equation plus a sink term:

$$u_i\frac{\partial C_a}{\partial x_i} = D\frac{\partial^2 C_a}{\partial x_i^2} - S_c, \qquad 6.13$$

where C_a is the air mass concentration of water vapour, kg/m^3, D is the diffusivity of water vapour in air, m^2/s, and S_c is the sink term deduced from the usual heat and mass transfer analogy:

$$S_c = k(C_a - C_w) = \frac{\bar{h}_m A_T}{V(1-\gamma)}(C_a - C_w) = \frac{\bar{h}_m A_T}{V_T}(C_a - C_w). \qquad 6.14$$

The sketch in Figure 6.8 shows the driving forces in the process of moisture absorption. In Equation 6.14, A_T and V_T (Figure 4.16) are the area and volume of the tray respectively; C_a is the air moisture concentration; C_w is the moisture concentration at the surface of the wafer and $\bar{h}_m$ is the average mass transfer coefficient due to convection in a duct (Bejan A. 1993):

$$\bar{h}_m = 0.023 Sc^{1/3} \mathrm{Re}^{4/5} \frac{D}{L_T}, \qquad \text{Turbulent flow,} \qquad 6.15$$

where Sc is the Schmidt number (ν/D); Re is the Reynolds number ($u\,L_T$ / ν); D is the mass diffusivity, and L_T is the hydraulic diameter, as shown in Figure 6.9.

The sink term is the rate of water absorption of the product in a given time. If the product is in a zone of high flow the mass transfer due to convection is high and the product absorbs water fast. Because of the latter, the 'capacity' of the product to absorb water decrease, as shown in Figure 6.10. At t_1 the product in the high flow (HF) zone has a bigger sink value than that of the product in the low flow (LF) zone. Also, the product in the HF zone has absorbed more water than that in the LF zone. At t_2 the product in the LF zone has more 'capacity' to absorb water than that in the HF zone because the product in this zone has reached a state near saturation. Thus, the moisture sink depends on the flow characteristics and the amount of water absorbed in a given time.

We do not have any information about the concentration of water vapour over the surface of the wafer, C_w. However, we have information about the moisture uptake of the wafer, C_B, under ambient conditions similar to that found in the room. Also, it is expected that the absorption process will finish when the air moisture concentrations and that over the surface of the wafer are equal. With that in mind, we can set a scale factor that normalises the experimental information in such a way that when the wafer has reached saturation the concentration of water vapour on the surface of the wafer will be the same as the concentration of water vapour in the air. Thus, in Equation 6.14, C_w is calculated from the experimental moisture absorption of the wafer multiplied by a scale factor:

$$C_w = \kappa C_B, \qquad \kappa = \frac{C_a}{C_{B\infty}}, \qquad 6.16$$

where C_B is the experimental moisture absorption of the wafer, C_a, is the concentration of water vapour in the air; and $C_{B\infty}$ is the experimental saturation value of water uptake of the wafer under similar conditions.

The model assumes that the controlling mechanism for mass transfer is convection. This assumption is based on the experimental data shown in Figure 5.41, where we can appreciate that moisture absorption is clearly augmented when the air velocity is increased. If diffusion were dominant the curves in Figure 5.41 would be very similar. Also, based on the analogy between heat and mass transfer and using Equation 6.15 we can show that the rate of mass transfer is proportional to:

$\dot{m} = Au^{0.8}$

The coefficient A should be the same to calculate mass transfer for the two different velocities displayed in Figure 5.41, if it mass transfer was controlled by convective processes on the outside of the biscuit. As an example, we choose from that experiment the values of 0.2 and 0.75 at 28h approximately. Using the expression given we can estimate for the first case a value for A of 0.348; for an air velocity of 2.4m/s the value of A is 0.36. As expected these values are very similar, validating our assumption of convection controlling mass transfer.

The model also assumes that the heat sink generated by the change of phase of water vapour absorbed by the biscuit is negligible and does not affect the mass transfer. This assumption is also based on the experimental data provided in Figure 5.41. As was shown before the calculation of mass transfer as a function of air velocity was acceptable and did not require a temperature correction.

6.3.3.1 Moisture absorption.

Moisture absorption by the wafer was calculated by integrating Equation 6.14, assuming that C_a, A_T, V_T and $\bar{h}_m$ are not function of time:

$$\int_0^\tau S_c dt = \bar{h}_m \frac{A_T}{V_T}\left[C_a\tau - \kappa\int_0^\tau C_B(t)dt\right] = k\left[C_a\tau - \kappa\int_0^\tau C_B(t)dt\right]. \qquad 6.17$$

The first term on the RHS of Equation 6.17 represents the moisture available to the wafer in the air. The second term represents the moisture absorbed by the wafer at a

given time. This last term limits the absorption capacity of the wafer, as illustrated in Figure 6.11.

The function form of $C_B(t)$ suggested by the experimental information is:

$$C_B(t) = C_{B\infty}\left(1-\exp\left(-k_e t\right)\right) = C_{B\infty}\left(1-\exp\left(-\kappa k t\right)\right) \quad , \qquad 6.18$$

where $C_{B\infty}$ = 5.0 kg/m^3 and k_e is an experimental mass transfer coefficient. The value of k_e for 2 and 4 finger bad packed trays value under controlled conditions is 1.16 x 10^{-5}s^{-1}. Equation 6.18 can also be obtained by integrating Equation 6.14, using the scale factor given in Equation 6.16 and considering that for $t = 0$, $C_B = 0$.

Integration of Equation 6.18 and the substitution of the result in Equation 6.17 results in:

$$\int_0^{\tau} S_c\,dt = k\left\{C_a\tau - \left[\kappa C_{B\infty}\left(\tau + (\exp(-k_e\tau)k_e^{-1}) - k_e^{-1}\right)\right]\right\}. \qquad 6.19$$

In the code we will calculate the wafer moisture absorption as follows:

1. Set in the moisture sink term an initial time, t_1.
2. Solve momentum, moisture, moisture sink and fluid age equations
3. When a satisfactory approximation is obtained the run is terminated.
4. To estimate the moisture distribution for $t > t_1$, we set the time in the sink term (assuming that the velocity field does not change) and run the model until a satisfactory approximation for the moisture and moisture sink equations has been reached.

The zones free of wafer should not absorb moisture at all. To accomplish all the latter we must modify the linear equations inside the code and implement appropriate sources.

As mentioned in Chapter 3, inside the code all the equations are treated as linear equations as follows:

$$a_p\phi_p + \sum_n a_n\phi_n = S = s_\phi + S', \qquad 6.20$$

where S' contains the diffusion coefficients and arise from the cross-derivatives due to the non-orthogonality of the grid, a_n is the standard matrix of coefficients obtained using hybrid-differencing normal to control volume faces and a_p is the net coefficient of the central node P, defined as:

$$a_p = \sum_n a_n - s_P \,. \qquad 6.21$$

In the code we set a_n, ϕ_n, and S' to zero. Now Equation 6.20 can be written as:

$$-s_p \phi_p = s_\phi \,. \qquad 6.22$$

In the implementation of the source term we should ensure that s_p is always negative. The reason for this condition should be explained. It has been shown (Scarborough, 1958) that a sufficient condition for a convergent iterative method is:

$$\frac{\sum |a_n|}{|a_p|} = \begin{cases} \leq 1 \text{ at all nodes} \\ < 1 \text{ at one node at least} \end{cases} \qquad 6.23$$

If the differencing scheme produces coefficients that satisfy the above criterion the resulting matrix of coefficients is diagonally dominant. Diagonal dominance is a desirable feature for satisfying the 'boundedness' criterion (Versteeg and Malalasekera, 1995). Two requirements for boundedness are:

- In the absence of sources, the internal nodal values of the property ϕ should be bounded by its boundary values.
- All coefficients of the discretised equations should have the same sign.

In particular, to achieve diagonal dominance we need to have large values of the a_p coefficient so the linearisation practice of source terms should ensure that s_p is always negative.

For the wafer zones, we want the scalar as:

$$\phi_p = \int_0^\tau S_c dt \qquad 6.24$$

To do that we have set

$$s_\phi = \int_0^\tau S_c dt \times C_c \qquad s_p = -C_c \qquad 6.25$$

Where C_c is a constant. For the zones free of wafer we want $\phi_p = 0$; thus we set $s_\phi = 0$ and $s_p = -1$. Finally, the value of C_w at the inlets is set to zero.

6.3.3.2 Figure of merit for moisture distribution

Nestle is not only interested in the performance of the ventilation system operating in the maturing room, but also in the effectiveness of the ventilation system to distribute

the moisture in the room. In order to compare different systems figures of merit are necessary. These figures of merit should be capable of ranking different systems in terms of their ability to achieve uniformity of product and speed of production.

One possible way to rank different set-ups is to take measurements at different positions with the aid of a hygrometer and apply a statistical analysis to the data. Unfortunately, this is extremely complicated and time consuming to do in situ due to the operation and dimensions of the room. Furthermore, it is very difficult, if not impossible, to obtain approval to change the ventilation system to test different arrangements. However, if the CFD model can predict the moisture distribution with a reasonable degree of confidence we can take as many samples as the number of control volumes inside the model.

The sample standard deviation provides us with a value of the dispersion of the parameter from an average value (Johnson. and Bhattacharyya. 1996). The sample standard deviation is defined as follows,

$$s = \sqrt{\frac{\sum_{i=1}^{n}(x_i - \bar{x})^2}{n-1}}, \qquad 6.26$$

where n is the number of samples, x_i is the value of the scalar. The mean is calculated by integration over the whole computational space, V_T, as follows:

$$\bar{x} = \frac{1}{V_T}\int_0^{V_T} x dV . \qquad 6.27$$

When we use the standard deviation to assess the dispersion of the data about the mean, we are assuming that the distribution of the data is close to a normal distribution; i.e. if we group the data they will be symmetrical around the mean. Departures from normality often take the form of asymmetry, or skewness. A common test for asymmetry is based on the coefficient of skewness of the sample,

$$a_3 = \frac{\frac{1}{n}\sum_{i=1}^{n}(x_i - \bar{x})^3}{s^3}. \qquad 6.28$$

A value of zero for a_3 means perfectly symmetrical curves, positive values means asymmetry to the right, and conversely for negative values.

Symmetric distributions can depart from normality by being too peak or too flat, as shown in Figure 6.12. These forms of departures may be detected by the coefficient of kurtosis,

$$a_4 = \frac{\frac{1}{n}\sum_{i=1}^{n}(x_i - \bar{x})^4}{s^4}, \qquad 6.29$$

For a normal distribution $a_4 = 3$ (Spiegel M., 1992).

Finally, to compare the relative dispersion of the data it is useful to describe the variability by expressing the standard deviation as a proportion of the mean (Bajpai A.C. *et al*, 1978). This measure is called the coefficient of variation and is defined by:

$$CoV = \frac{s}{\bar{x}} \times 100 \ . \qquad 6.30$$

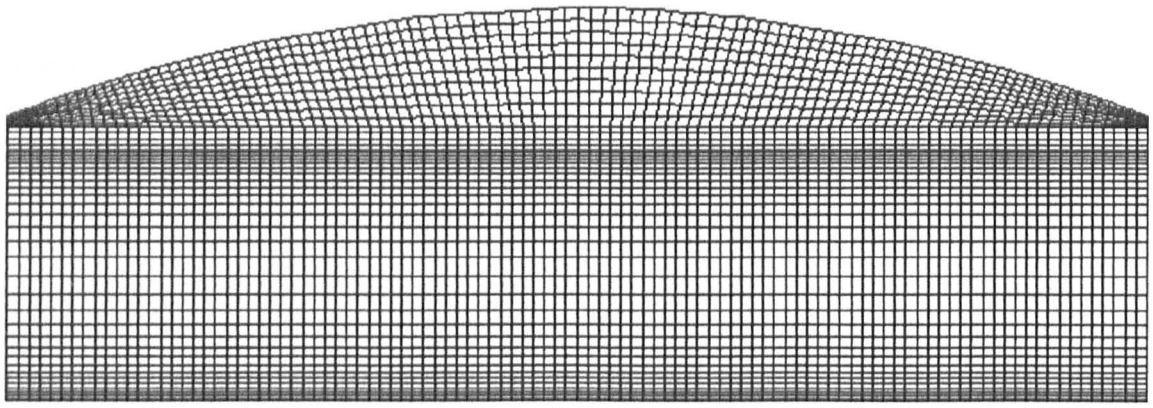

Figure 6.1. Geometry grid for the hangar. Front view.

Table 6.1. Temperatures in the walls.

Condition	T wall E	T wall W	T wall N	T wall S	T roof	T floor
Measured	15°C	16°C	16°C	14°C	18°C	17°C
Extreme	10°C	11°C	11°C	8°C	12°C	11°C

Table 6.2. Scenarios simulated.

Scenario	Heaters	Door (Area = 1833 m^2)	
		T, °C	m_{out}, kg/s
1	All	14	0.00
2	All	14	38.37
3	All. Recirculators.	14	0.00
4	2, 5, 7, 9, 10 Recirculators.	14	45.57
5	2, 5, 7, 9, 10. Recirculators.	14	0.00

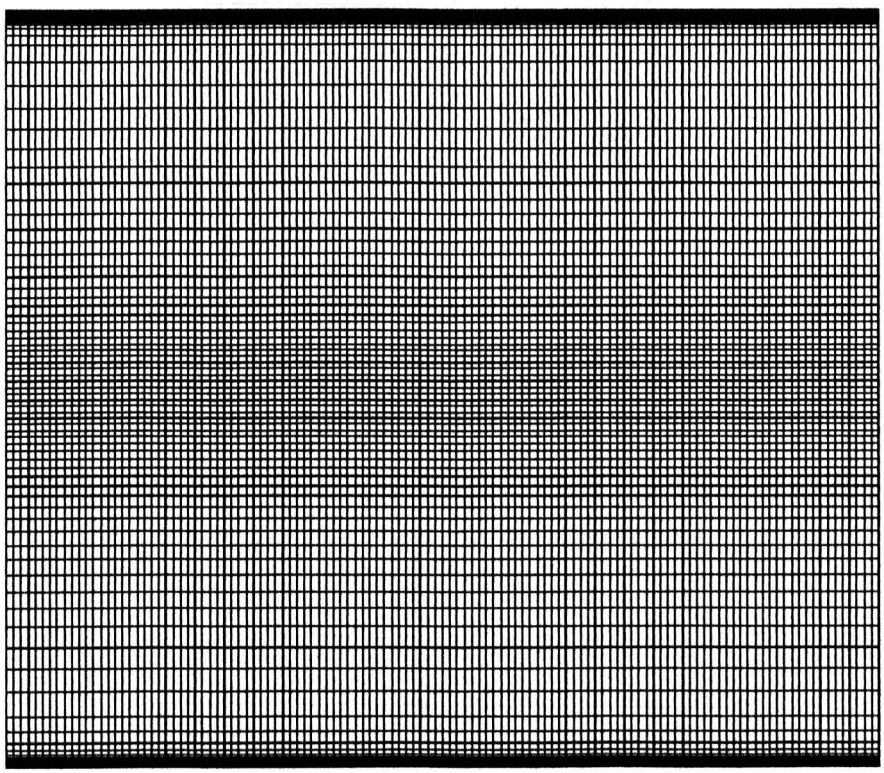

Figure 6.2. The grid for the repository room. Top view.

Table 6.3. Storeroom modelled scenarios.

Scenario	Description
1	Empty room. Experimental distribution on inlets and outlets.
2	Experimental distribution on inlets and outlets. Room full.
3	The same as 2 plus 20 recirculation units.
4	The same as 3 but using a good packing technique of the trays.

Table 6.4. Outlet arrangement in CFD model.

OUTLET	BOTTOM
A	CLOSE
B	½
C	OPEN
D	CLOSE
E	½
F	CLOSE
G	½
H	½
I	½
J	½
K	½
L	OPEN
The top of all outlets was open.	

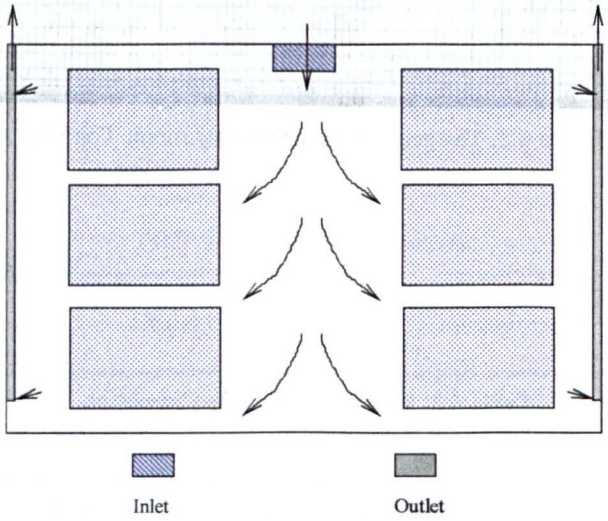

Figure 6.3. Sketch of flow distribution in scenario 2.

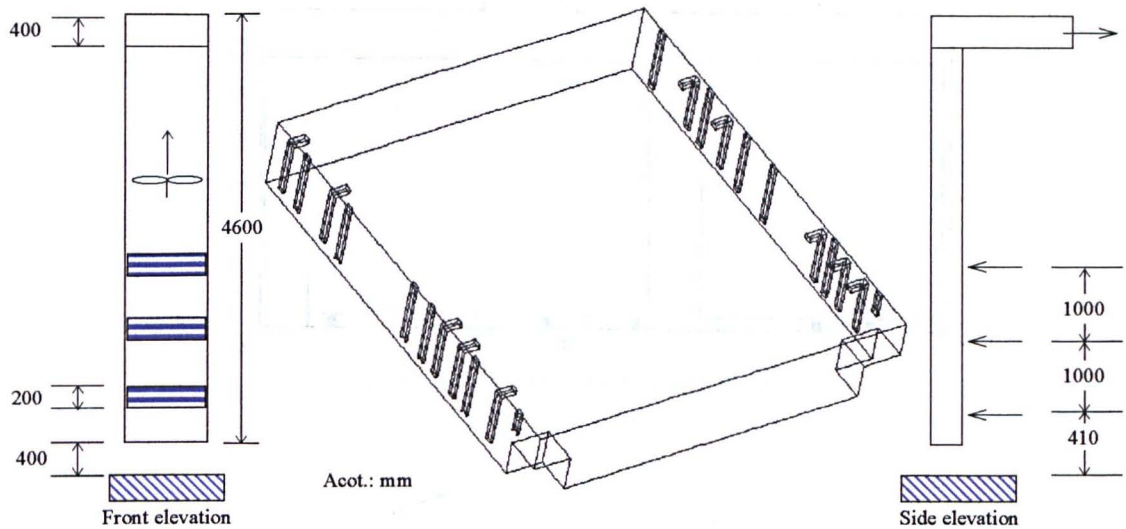

Figure 6.4. Maturing room with 10 recirculation units and sketch of a recirculation unit.

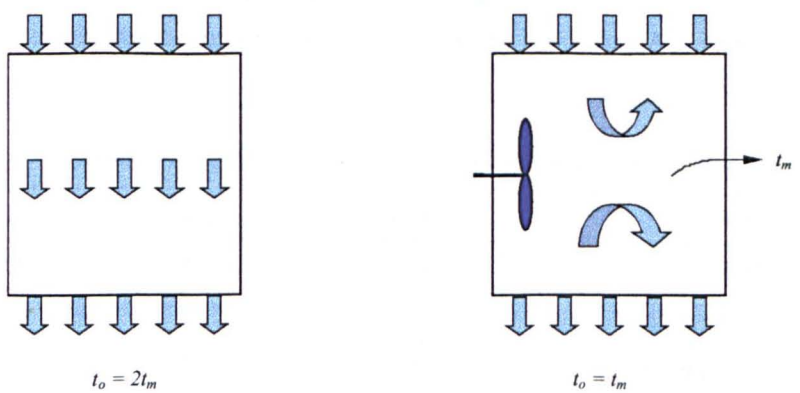

Figure 6.5. Types of ventilation behaviour.

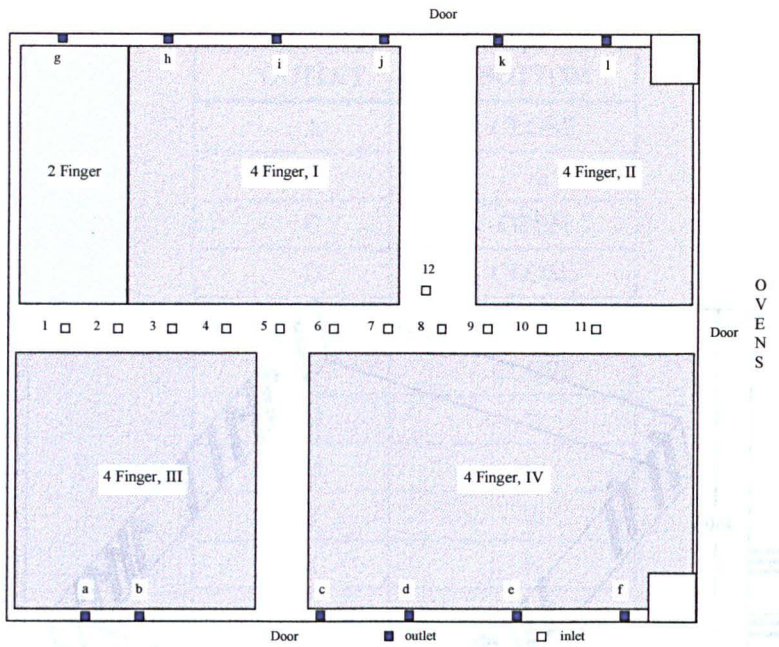

Figure 6.6. Porous zones in CFD model.

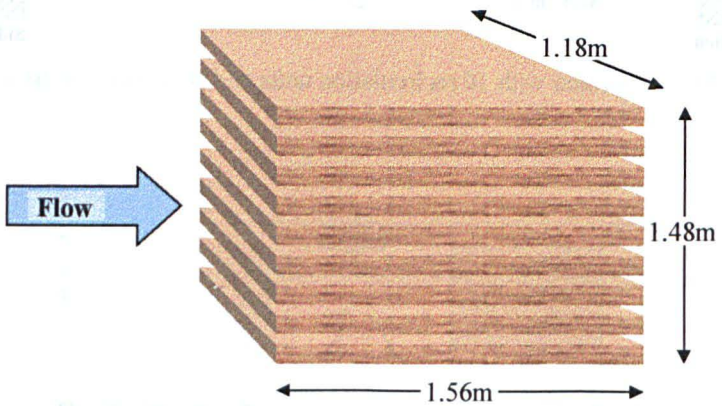

Figure 6.7. Approximate dimensions used to calculate the bed volume.

Table 6.5. Data used to calculate resistance in the porous model.

Arrangement	A_w, m^2	V_B, m^3	D_p, m
2 finger badly packed	0.30	2.75	4.07
4 finger badly packed	0.33	2.75	0.66
2 finger well packed	0.35	2.75	4.92
4 finger well packed	0.40	2.75	2.17

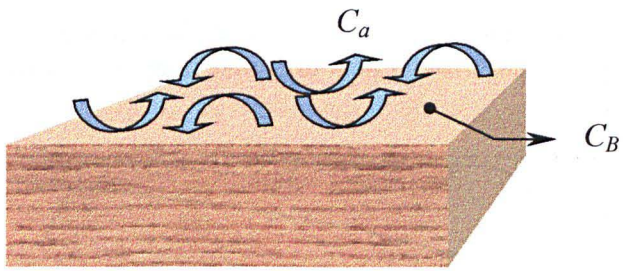

Figure 6.8. Sketch of the driving forces in the moisture absorption model.

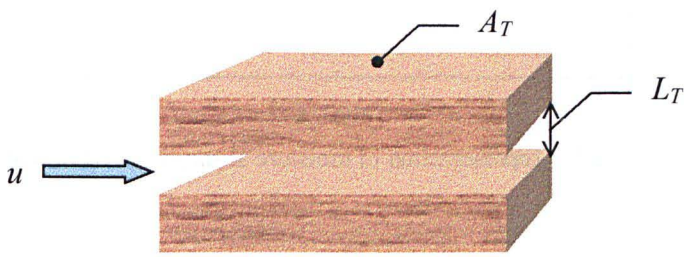

Figure 6.9. Sketch of the dimension for the mass transfer coefficient.

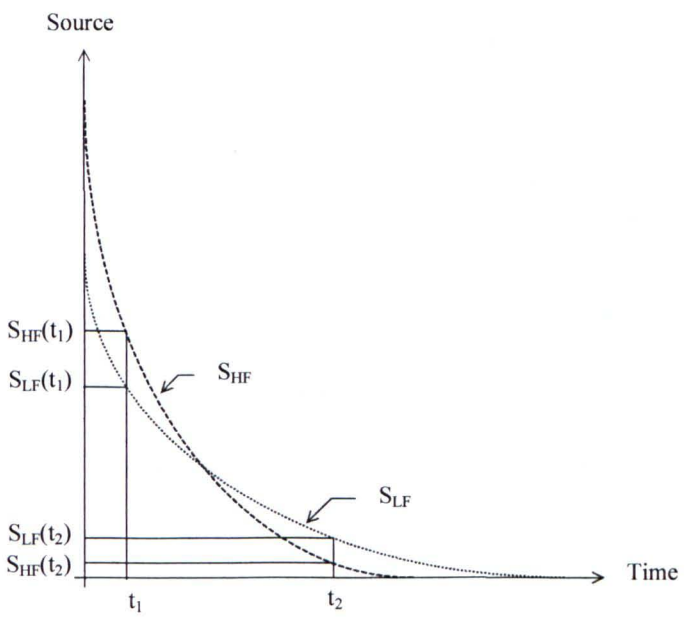

Figure 6.10. Sink term at different zones (HF: High flow; LF: Low flow).

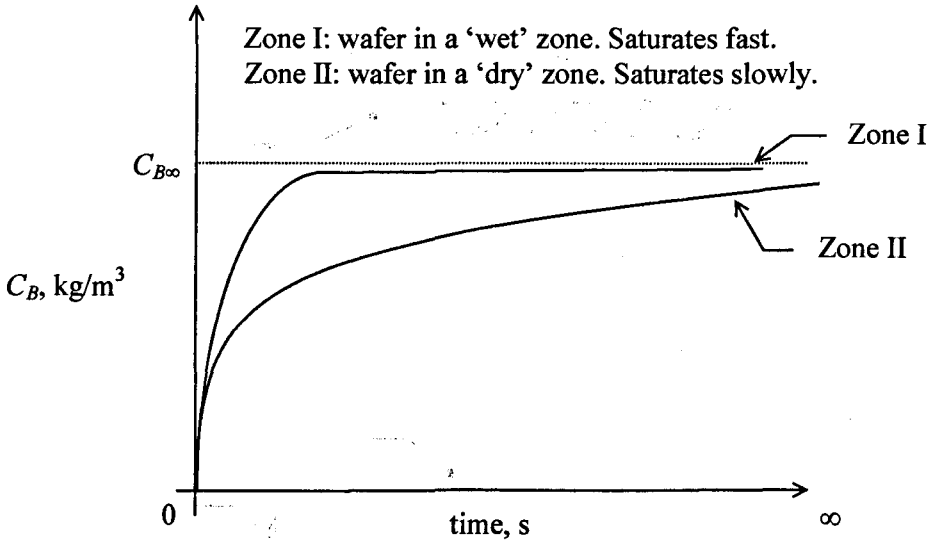

Figure 6.11. Graphic representation of moisture absorption in different zones.

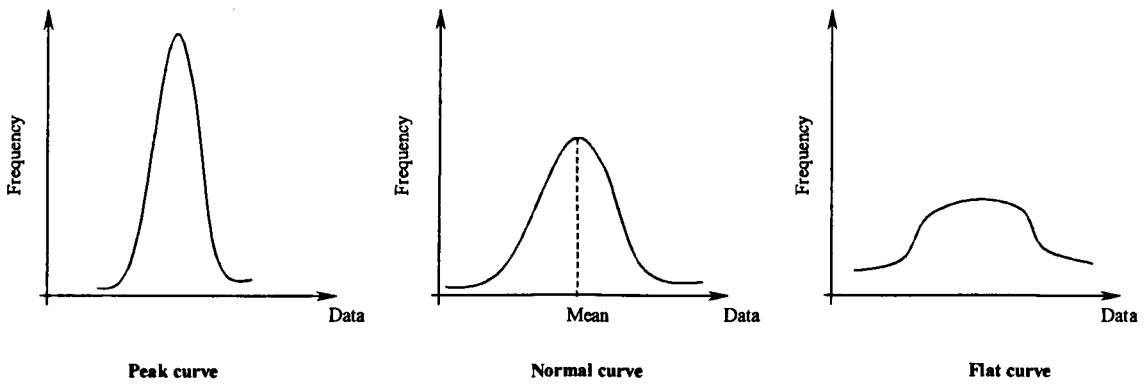

Figure 6.12. Distribution of statistical data.

7 NUMERICAL RESULTS

7.1 Introduction.

This chapter presents the numerical results for the industrial cases analysed. These results are compared against the appropriate experimental or measured data. As in the rest of the work, the presentation of this chapter divides it naturally in bouyancy affected flow and porosity affected flows.

7.2 Bouyancy affected flows.

The measured and calculated dimensionless profile of the stratification at the approximate position of point 4 is shown in Figure 7.1. The stratification is more accentuated in the CFD result, though the pattern of the calculated profile is similar to the measured one. The results show a clear stable stratification along the height of the hangar. However, the unstable condition found in the experimental data is not produced in the CFD calculations. This is probably due to phenomenon being transient and the CFD calculations were solved for steady state solution.

As expected, the CFD simulations for scenario 1 have shown that the effect of bouyancy causes that most of the hot air from the heaters to be 'trap' at the top of the hangar, as can be seen in Figure 7.2 and Figure 7.3. This situation seems to be further accentuated by the flow of hot air through the gap at the top of the hangar, Figure 7.4, suggesting that the hangar coupling is an aspect that could affect the thermal behaviour in the hangar. The flow structure created by the combined effect of buoyancy and hangar coupling leads to the formation of stagnant zones. Figure 7.5 shows that the west side of the hangar is isolated by an extensive zone of stagnant fluid, highlighted by a large value of the fluid age. Furthermore, the stagnant zone is much accentuated at the middle height of the hangar, suggesting that the hot air blown from the heater reaches its maximum penetration and spreads horizontally, as in the tank experiments, and spends some time at that level before ascending to its equilibrium level.

In general, the hot air flows out of the east hangar through the top whilst cold air enters through the lower section. This hot air flows from the top of the dome of the hangar and through the gap. It should be mentioned that the air that enters the hangar through the lower part of the gap it has a temperature of 17°C, which is colder than the temperature that is at the top of the hangar. Also, some the hot air flows from the top following the walls causing an uneven distribution of the temperature field. As can be seen in Figure 7.6 the temperature field estimated from the measured temperature in the hangar is very similar to that calculated, even the cold zone at the centre of the hangar is replicated by the simulation. At working level the CFD calculation shows and uneven distribution of temperature with the hangar in divided in two zones, as shown in Figure 7.7.

Leaving the doors open creates a high rate of exfiltration, as can be seen in Figure 7.8. Although exfiltration promotes horizontal air movement in the working zone, it seems that its contribution to air mixing in the vertical direction is not enough to avoid the trapping of hot air at the top of the hangar, Figure 7.9. Compared to scenario 1, in scenario 2 exfiltration causes an increase of 7.7% of the heat leakage to the surroundings. It should be noted that the horizontal air movement does not homogenise the temperature distribution at working level, as show in Figure 7.10.

The use of recirculation devices or 'tall boys' helps to homogenise the flow and temperature distribution in the hangar in working area, Figure 7.11 and Figure 7.12. Finally, by using only 5 heaters and the 'tall boys' it is possible to obtain acceptable working conditions and temperature distribution (Figure 7.13 and Figure 7.14). However, leaving the doors open reduces the effect of the 'tall boys' in the homogenisation of the temperature field, as can be seen in Figure 7.15and Figure 7.16.

7.3 Porous affected flow

The value of IOVP for scenario 1 (the empty room case) was 0.84, which is the maximum value of IOVP obtained for all scenarios, as expected. Figure 7.17 shows a well-balanced fluid age distribution, with the highest fluid age values near the bottom and toward the corners. The uneven distribution of the flow is due to the imbalance of the inlet air. It is possible that the damper arrangement of the outlets has been set with the objective of reduce the expected maldistribution.

The introduction porous zones promote short-circuiting and areas of poor airflow. These areas are highlighted by high fluid age values in the interior of the storeroom, as can be seen in Figure 7.18. From the IOVP values obtained for the rest of the scenarios, it became apparent that using recirculation units could enhance the ventilation performance. Figure 7.19 compares IOVP values for scenarios 2, and 3. Comparing with scenario 2 (existing filled room case) with scenario 3 (as for scenario plus the 20 recirculators) the ventilation performance improves almost 30%, this is illustrated by Figure 7.20 where the areas with high fluid age value had been reduced. Furthermore, the combined effect of recirculation units and well packaging technique, scenario 4, increases more than 87 times the performance of the ventilation system, as can be seen in Figure 7.21 where the maximum value of fluid age scales reflects this condition. This large increment is could be due to the non-linearity of the Ergun equation, where the value of the volume porosity has a considerable effect on the calculation of the airflow resistance, as showed in Figure 7.22. Furthermore, the resistance not only reduces the velocity, but also promotes short-circuiting, as sketched in Figure 7.23. These factors contribute to the presence of areas of high fluid age values, which increase the mean fluid age substantially reducing IOVP.

The model developed to simulate moisture absorption was able to reproduce the trends measured using silicagel bags in the room. Figure 7.24 depicts a comparison of CFD and experimental results for approximately the same location in the room. The profile obtained by CFD is much more accentuated than that obtained in the room. On average the calculated moisture uptake is approximately 28% lower than the obtained in the room. The highest differences are at the centres of the stacks. It is possible that we are overestimating the airflow resistance or that the arrangement selected to model the room differs from the testing conditions, or a combination of both. These two factors affect the flow distribution, which have an effect in the moisture uptake. In the CFD

calculations we are assuming that the room is completely full and that the initial arrangement does not change through the testing period. Under real work conditions the arrangement of the wafers within the room changes from time to time, thus affecting the flow distribution.

The absorption of moisture increases when recirculation units are used. For example, the mean moisture uptake for scenario 2 was 1.25 kg/m^3 whilst for scenario 3 was 1.48 kg/m^3 during 10 days of operation, i.e. an increment of 18.5%. When the effect of using well packed trays is added to that of the inclusion of recirculation units as in scenario 4, the mean moisture uptake increases 2 times with respect to scenario 2 for the same operation period, as can be seen Figure 7.25.

Figure 7.26 to Figure 7.28 show graphically the improvement of moisture absorption when recirculation units are used. Also, we can notice that the worst areas in terms of moisture absorption correspond to areas of high fluid age. In areas of low fluid age fresh air laden with moisture flows saturating rapidly the product; whereas, in areas with high age the air has previously ceded most of its moisture causing the appearance of low moisture uptake zones, as illustrated in Figure 7.29.

At the beginning of the maturation process the wafers zones located near well-ventilated areas will absorb more moisture than those located in poor ventilated areas. This will cause that in the earlier stages of the maturation process the distribution of moisture uptake measured as the standard deviation will increase. In later stages, as more and more wafer zones reach saturation the value of the standard deviation will decay and, given enough time, will be zero. By introducing changes in the storeroom we wish to increase the moisture uptake as homogeneously as possible. Under the current operating conditions of the storeroom, scenario 2, after 10 days the maturation process is slow, leaving areas with low moisture uptake as show in Figure 7.26. The introduction of recirculation devices increases the moisture uptake and improves its distribution. Further improvement is achieved when good packing techniques are used, as can be seen in Figure 7.28. The analysis of statistical data for the different scenarios simulated indicate that the distribution of moisture uptake is scenario 2 is more skewed to the right than scenarios 3 and 4, as show in Table 7.1. Also, the three scenarios are more peaked than the normal distribution. Insofar as 'peakedness' is concerned, the distribution of moisture uptake in scenario 4 approximates the normal distribution much better than scenario 3 and yet more than scenario 2.

Finally, Table 7.1 shows an increment of the standard deviation of moisture uptake when recirculation devices are introduced in the room, with further increase when good packing techniques are simulated. However, as has been shown, the mean moisture uptake also increases when we apply modification to the storeroom. Under this circumstances the coefficient of variation, defined in Equation 6.29, helps us to compare the relative dispersion of the data. The scenario with the lower value for the coefficient of variation will show a lower variation with respect to its mean, and thus a better distribution of the moisture uptake. Figure 7.30 shows that under the conditions imposed for scenario 4 the coefficient of variation is lower than in scenario 2, a reduction of approximately 17%.

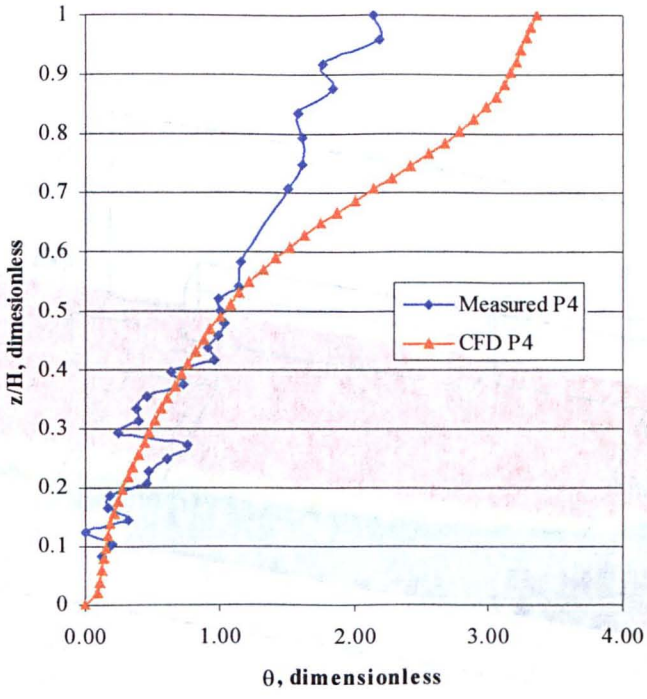

Figure 7.1. Comparison of measured and calculated relative stratification profile at point 4. Scenario 1.

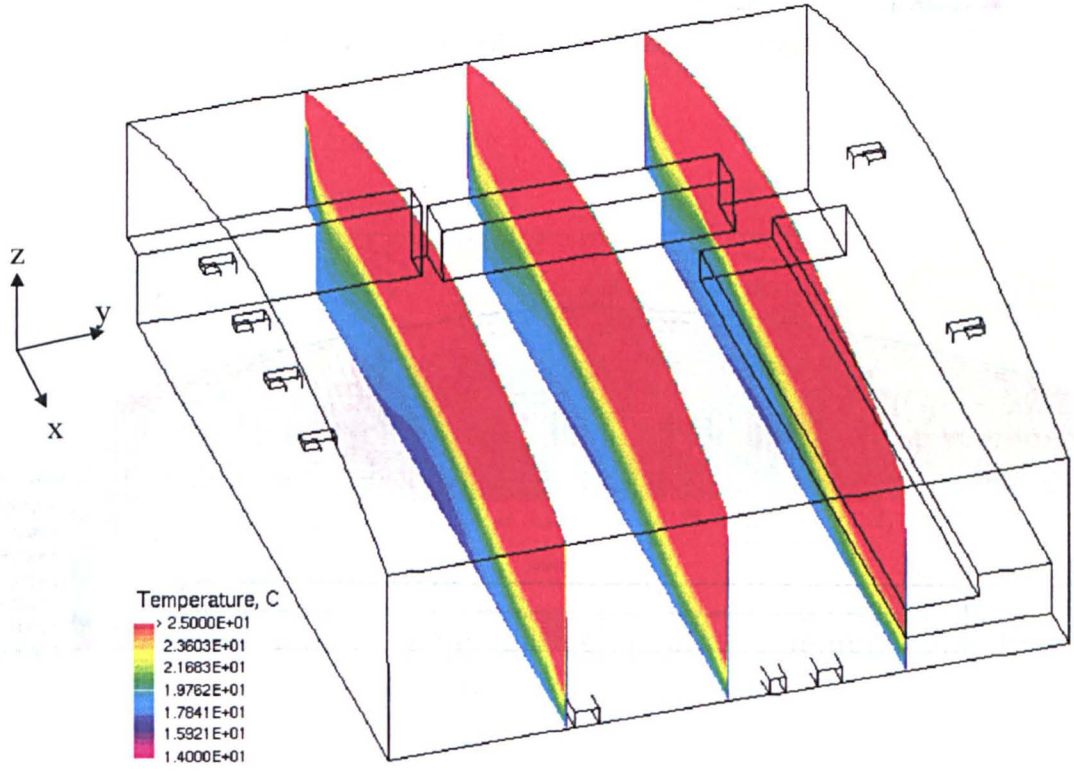

Figure 7.2. Scenario 1, y = 22, 42, 64m. Temperature field.

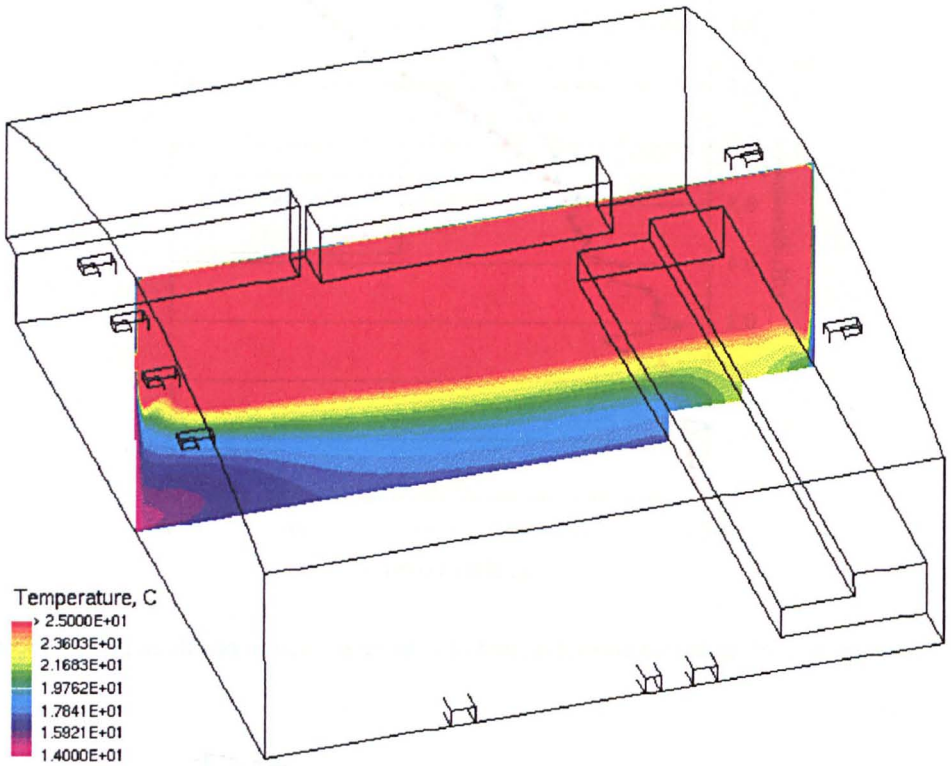

Figure 7.3. Scenario 1, x = 54m. Temperature field.

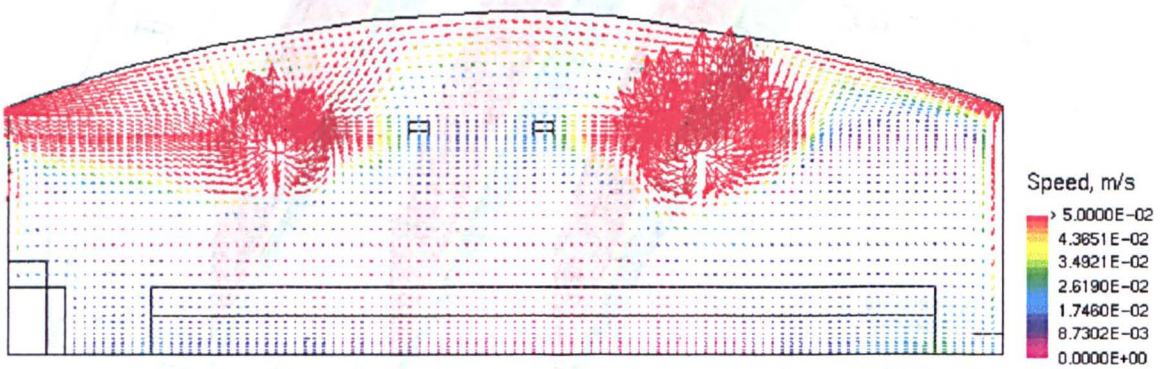

Figure 7.4. Scenario 1, y = 64. Velocity field.

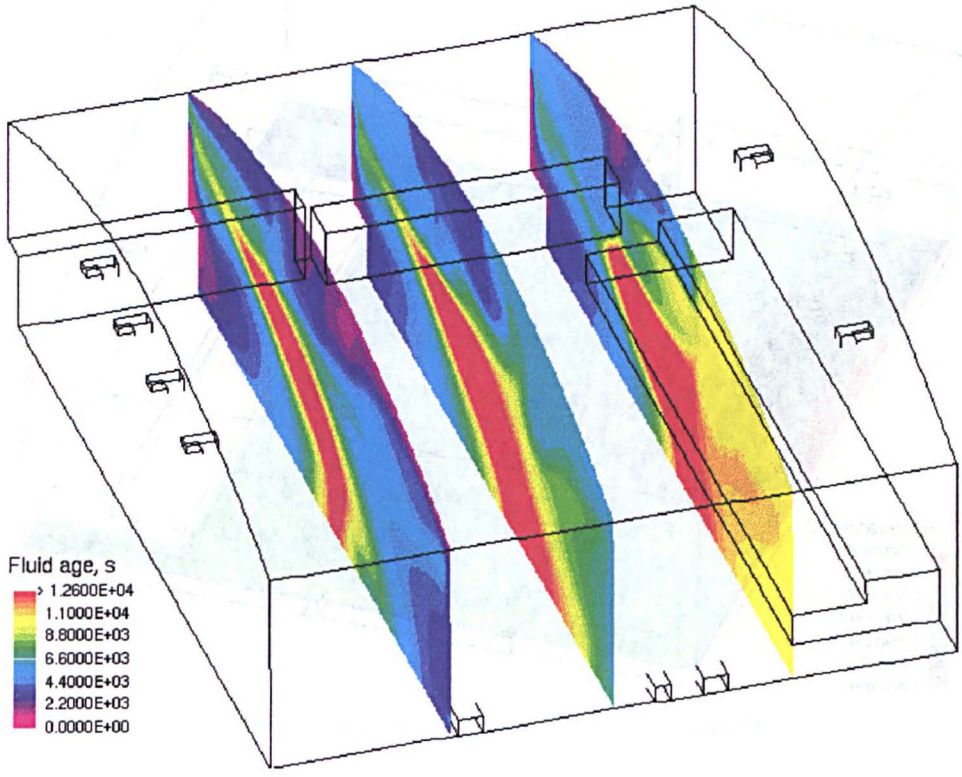

Figure 7.5. Scenario 1, y = 22, 42, 64m. Fluid age field.

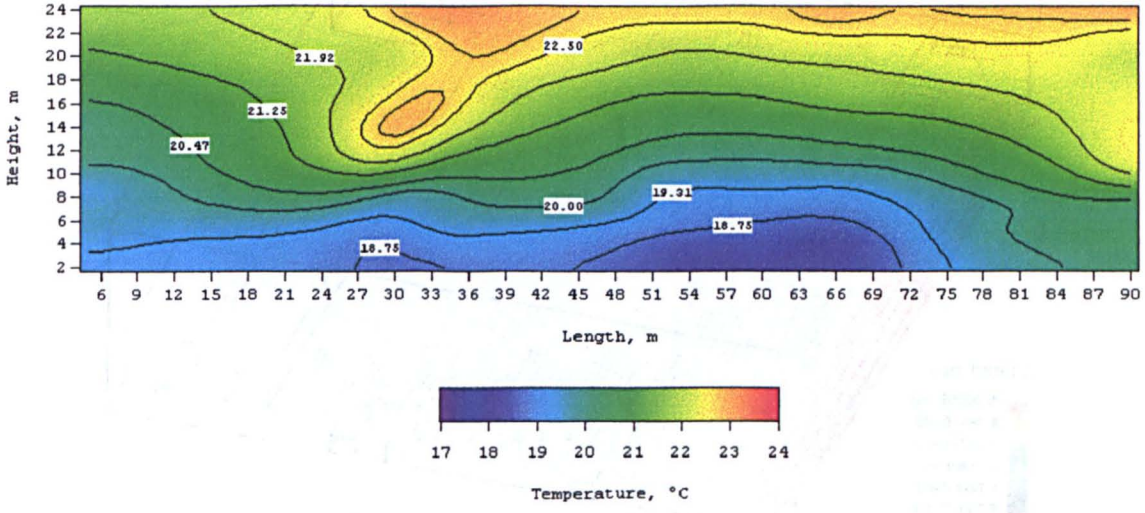

Figure 7.6. Temperature field in the hangar on March 19.

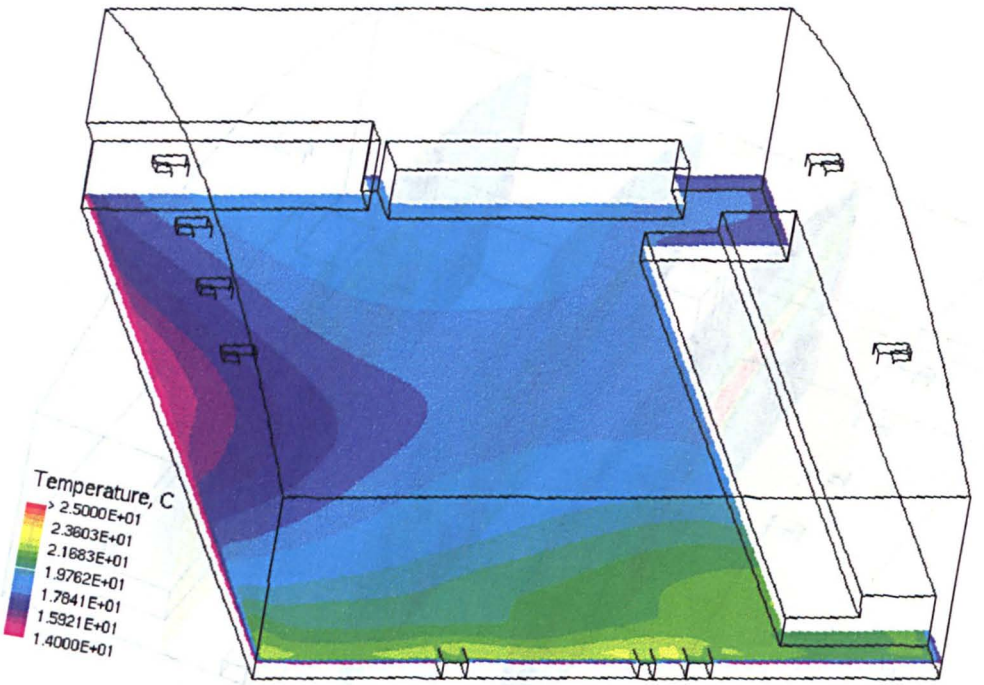

Figure 7.7. Scenario 1, z = 2m. Temperature field.

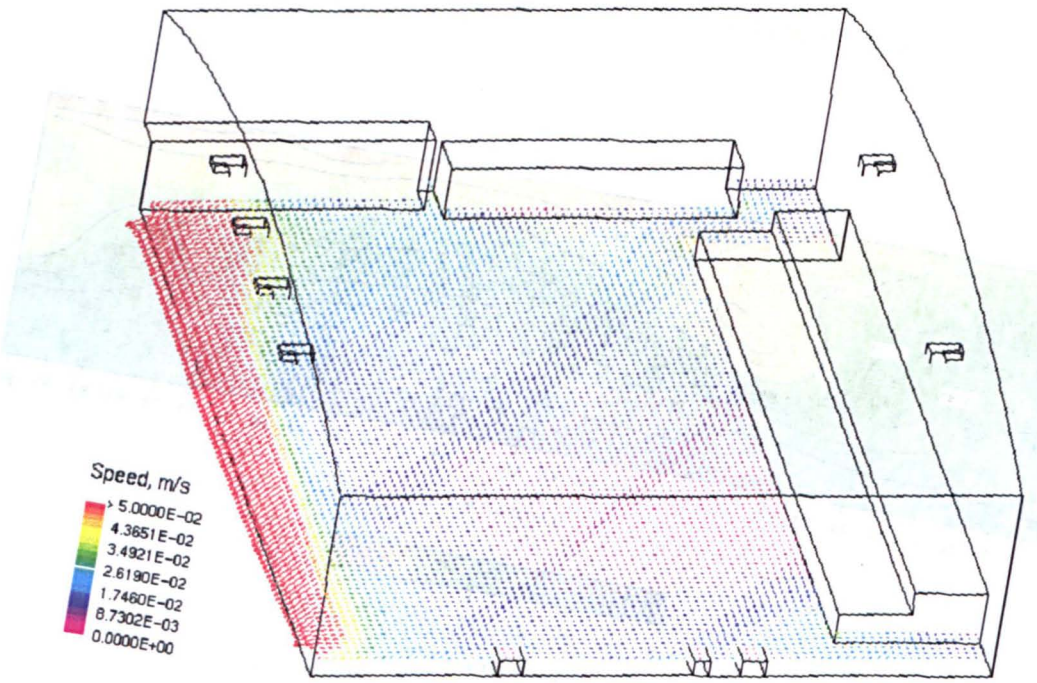

Figure 7.8. Scenario 2, z = 2m. Velocity field.

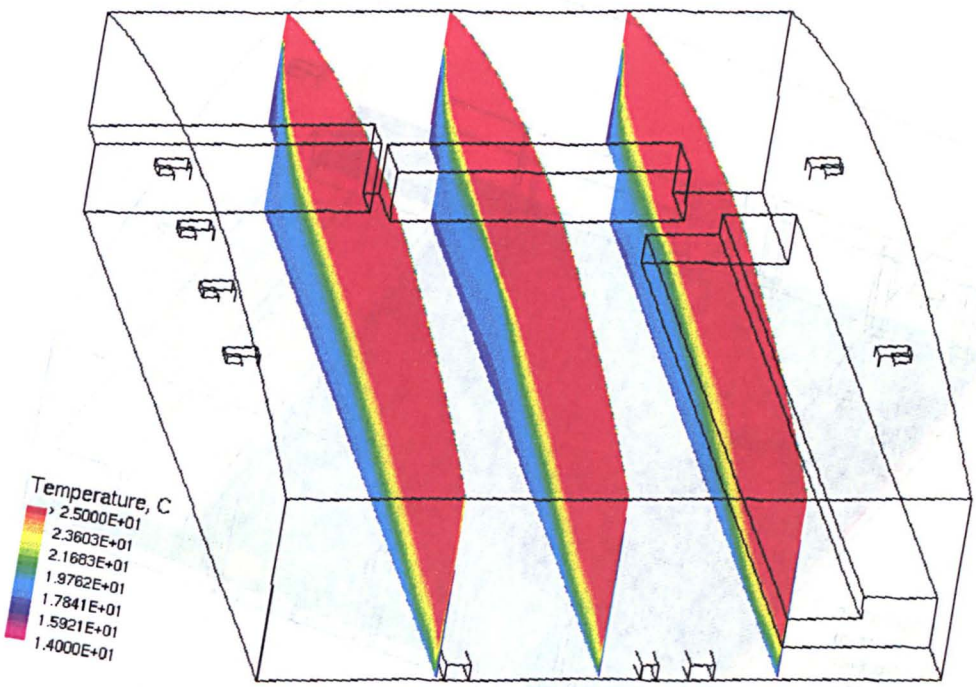

Figure 7.9. Scenario 2, y = 22, 42, 64m. Temperature field.

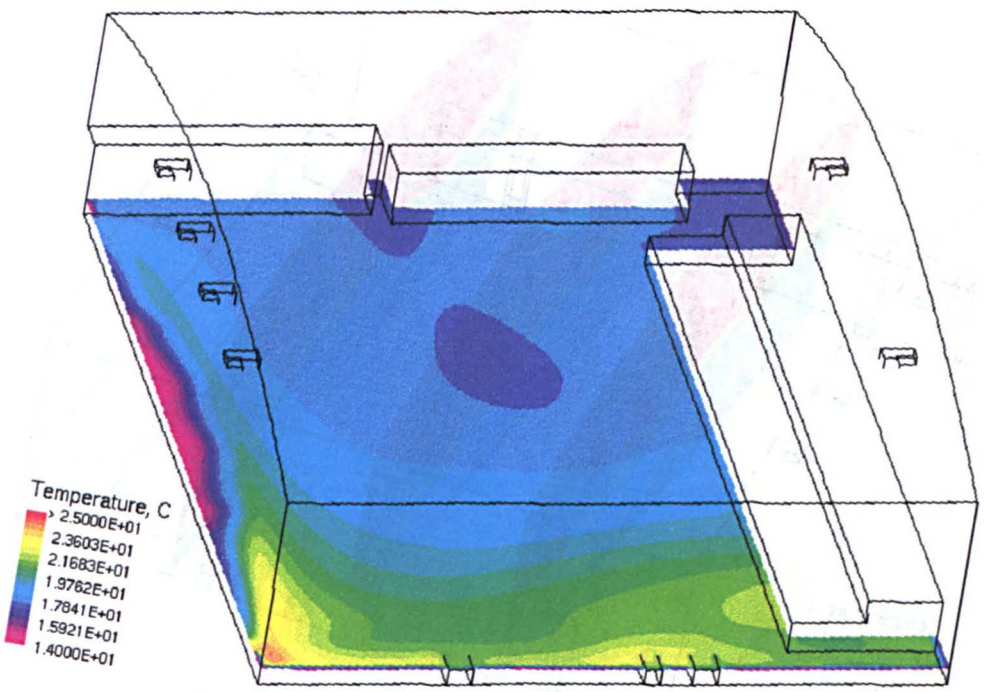

Figure 7.10. Scenario 2, z = 2m. Temperature field.

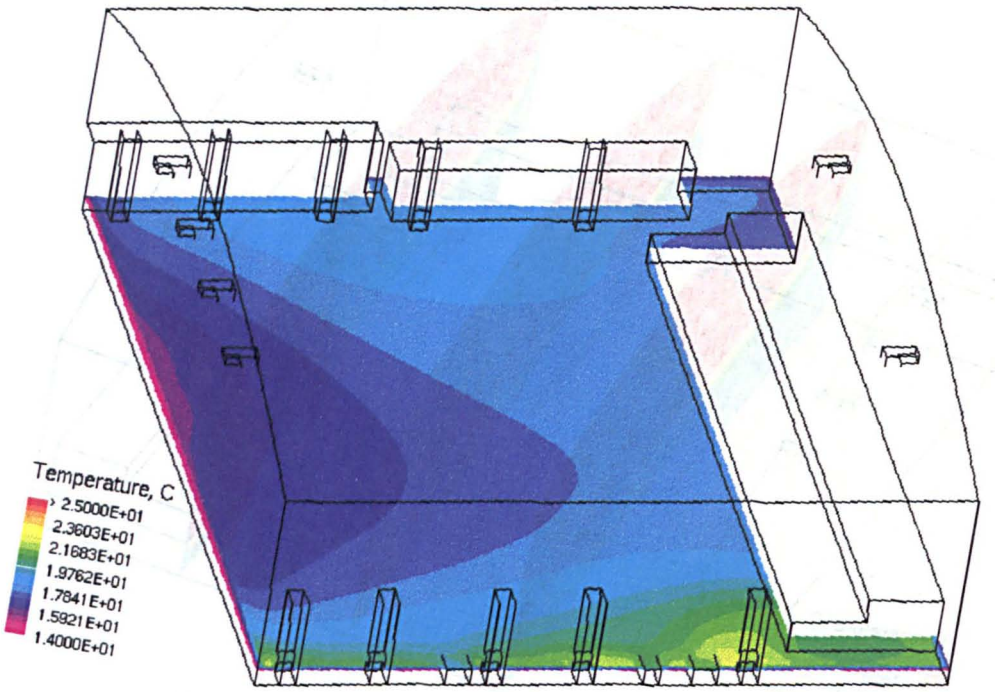

Figure 7.11. Scenario 3, z = 2m. Temperature field.

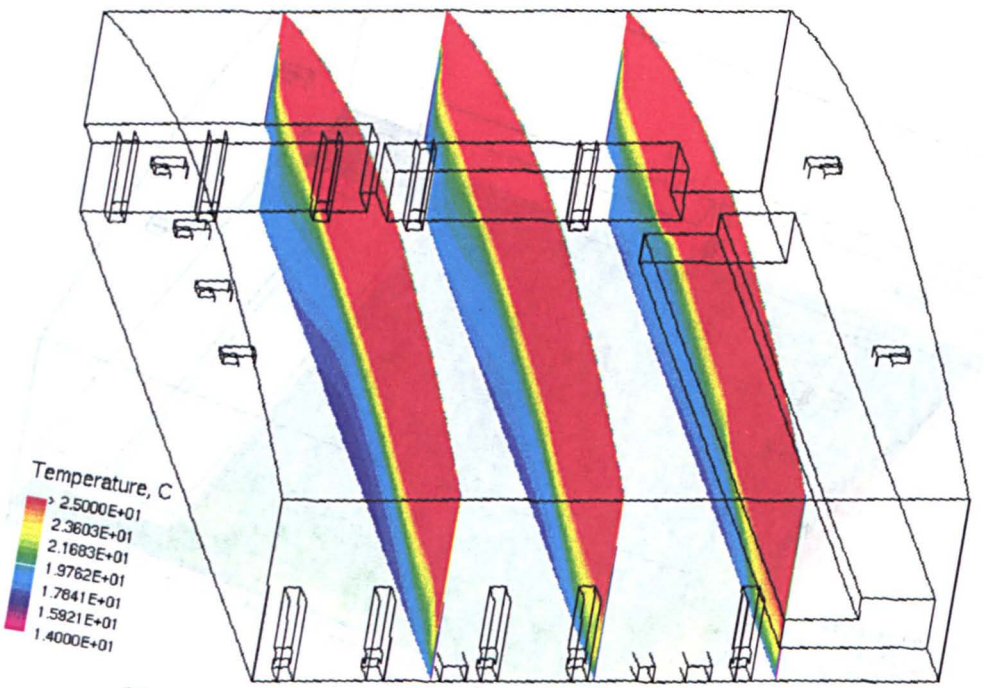

Figure 7.12. Scenario 3, y = 22, 42, 64m. Temperature field.

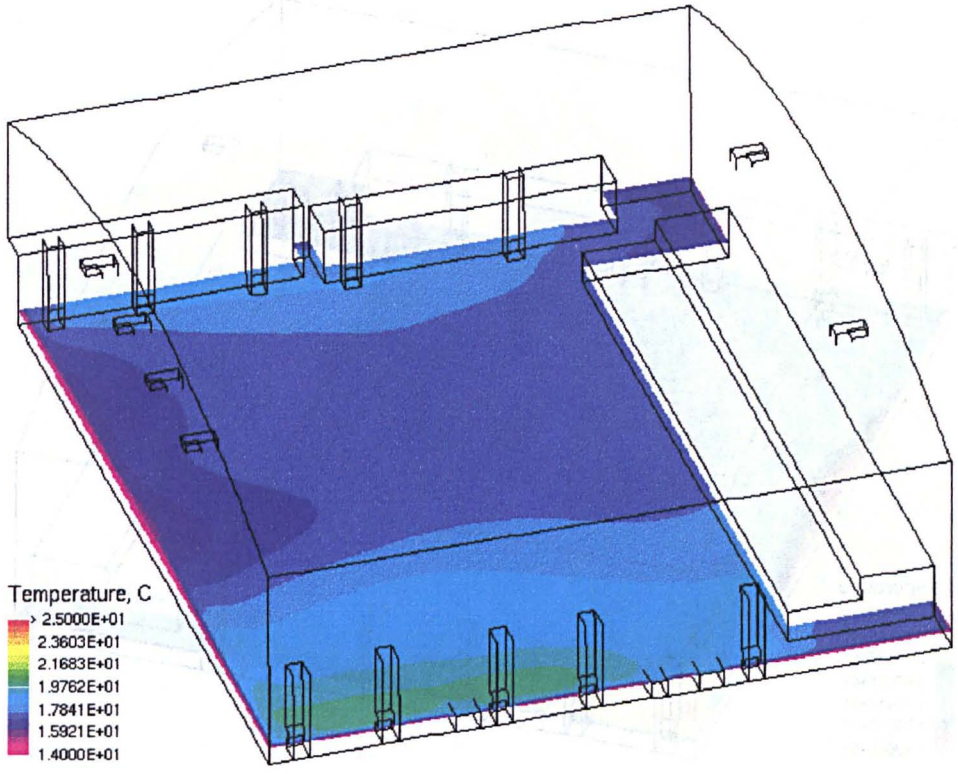

Figure 7.13. Scenario 4, z = 2m. Temperature field.

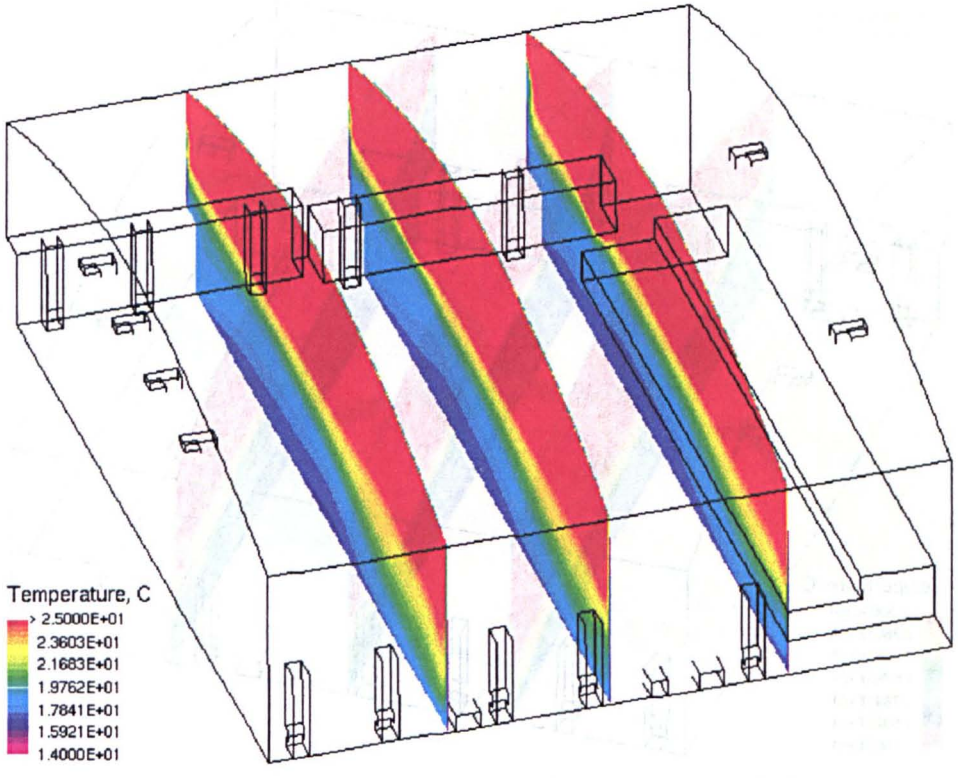

Figure 7.14. Scenario 4, y = 22, 42, 64m. Temperature field.

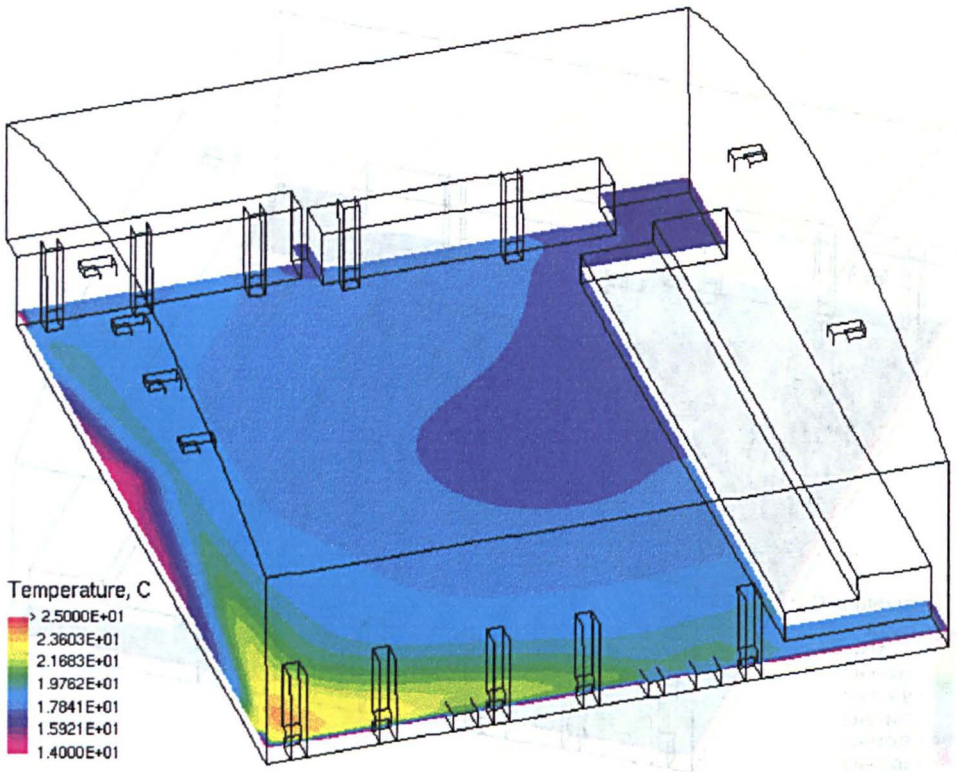

Figure 7.15. Scenario 5, z = 2m. Temperature field.

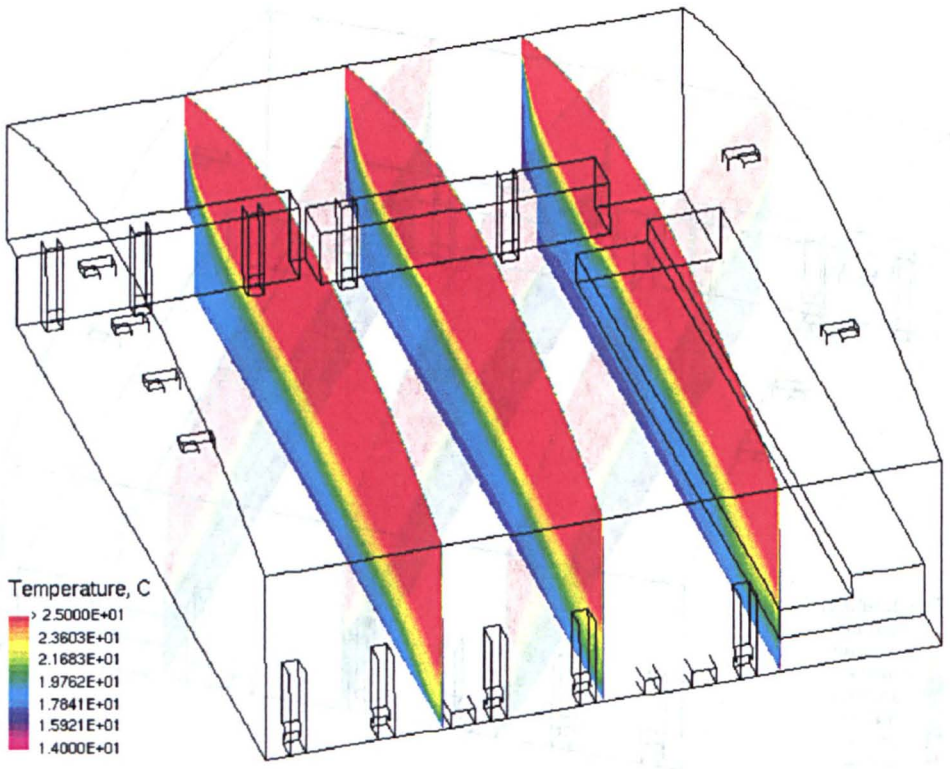

Figure 7.16. Scenario 5, y = 22, 42, 64m. Temperature field.

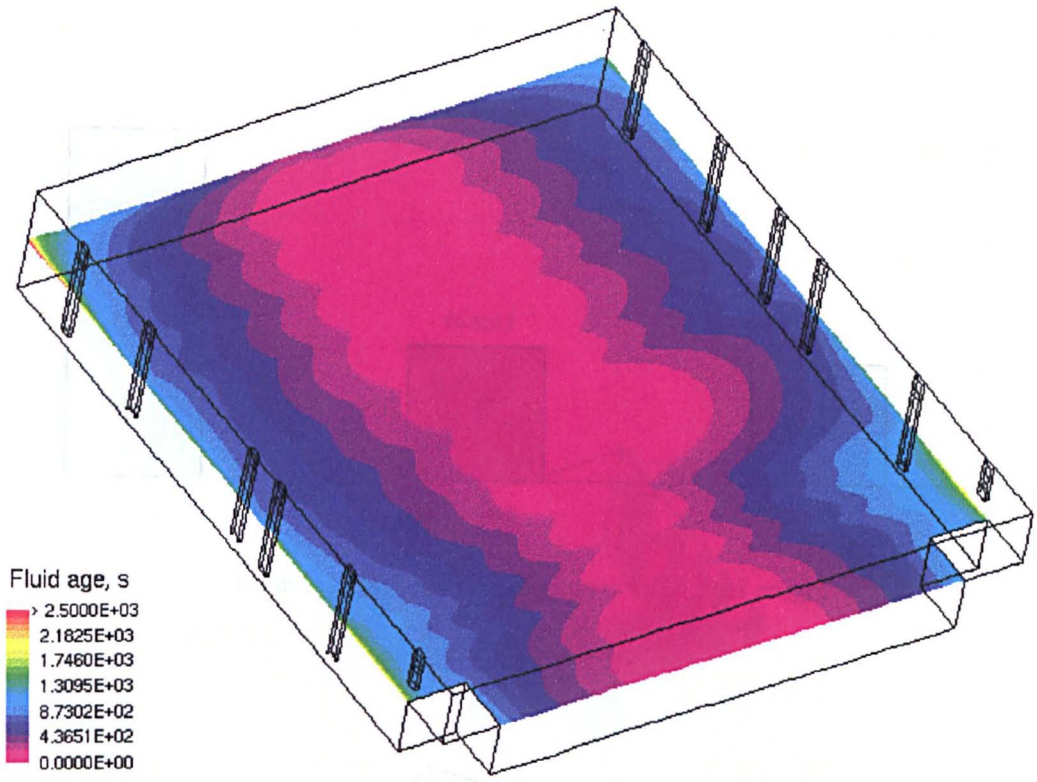

Figure 7.17. Scenario 1. Z = 3m.

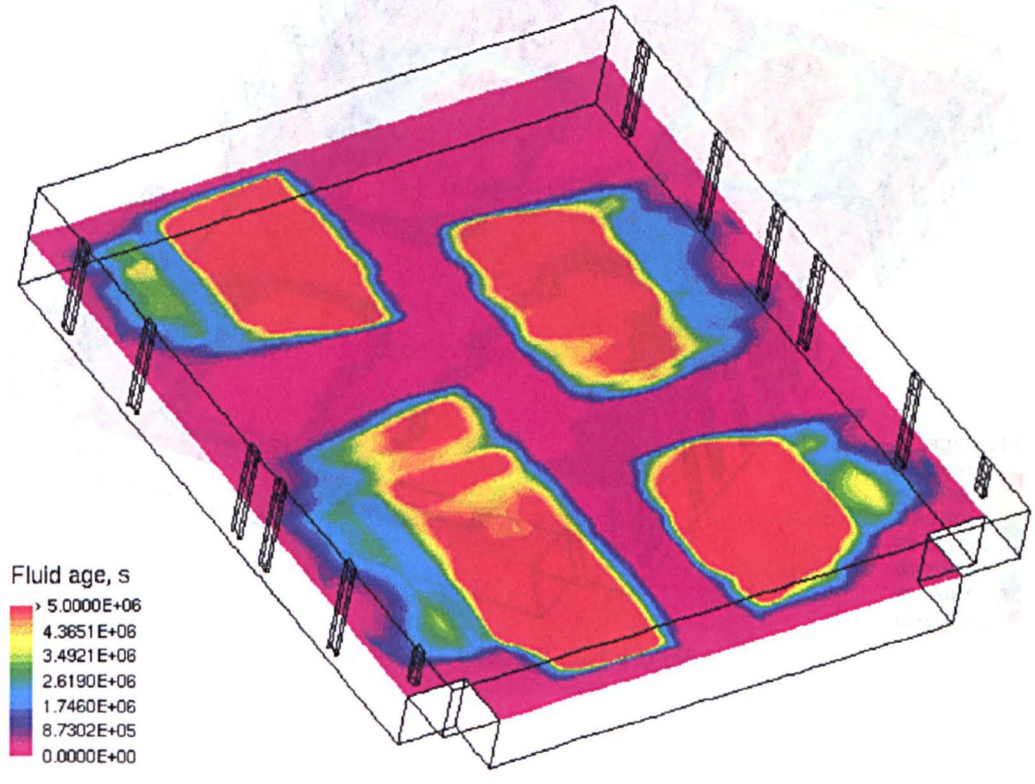

Figure 7.18. Scenario 2. Z =3m.

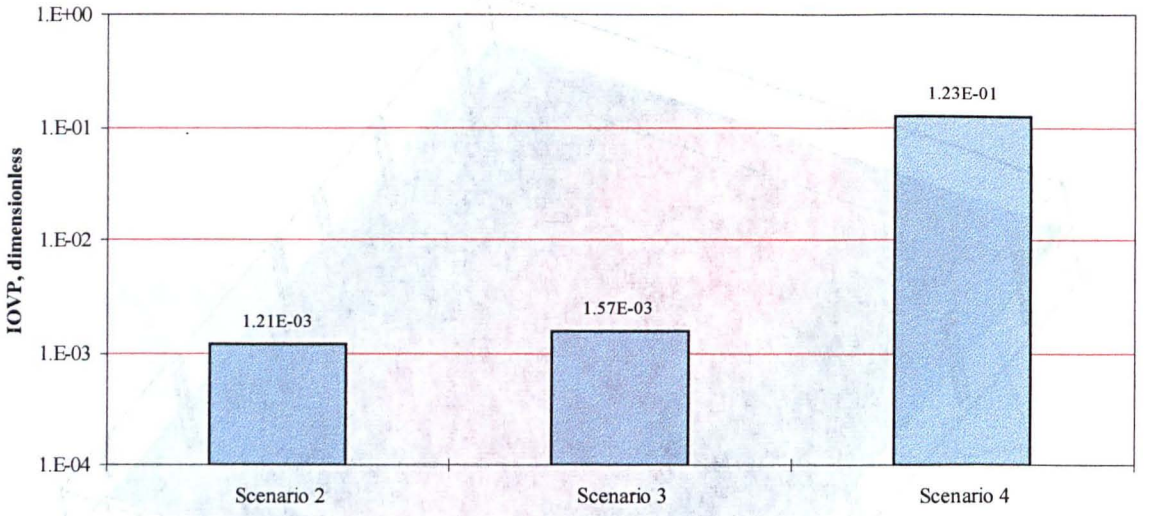

Figure 7.19. IOVP comparison for scenarios 2, 3 and 4.

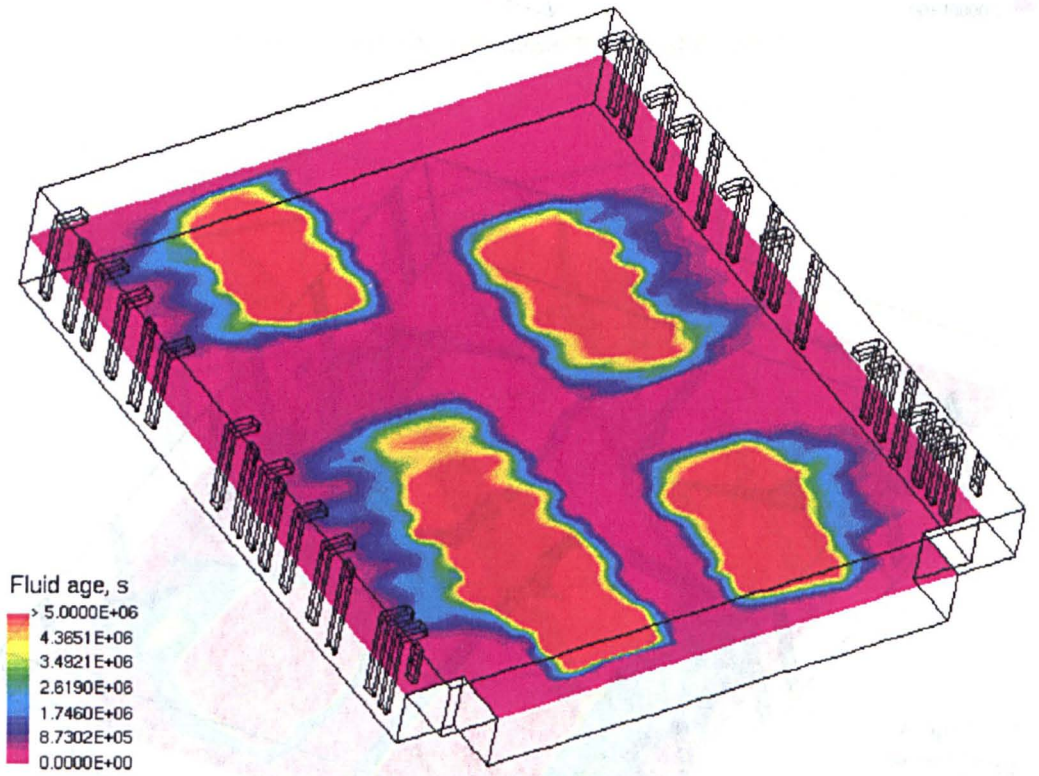

Figure 7.20. Scenario 3. Z = 3m.

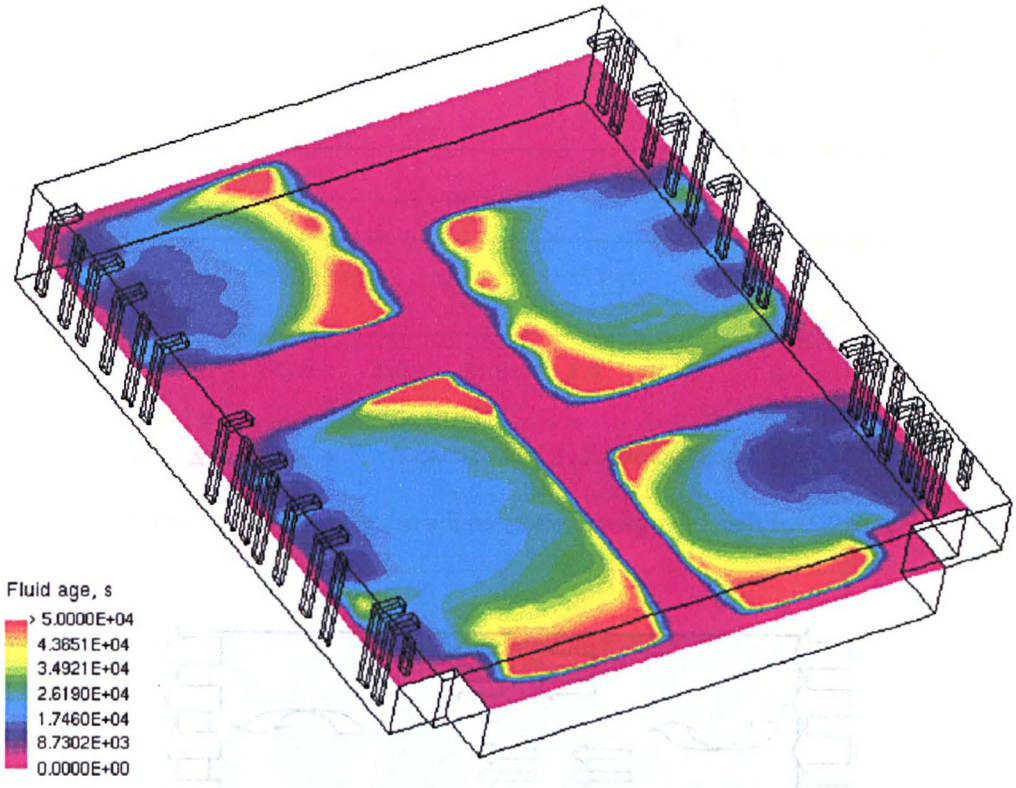

Figure 7.21. Scenario 4. Z = 3m.

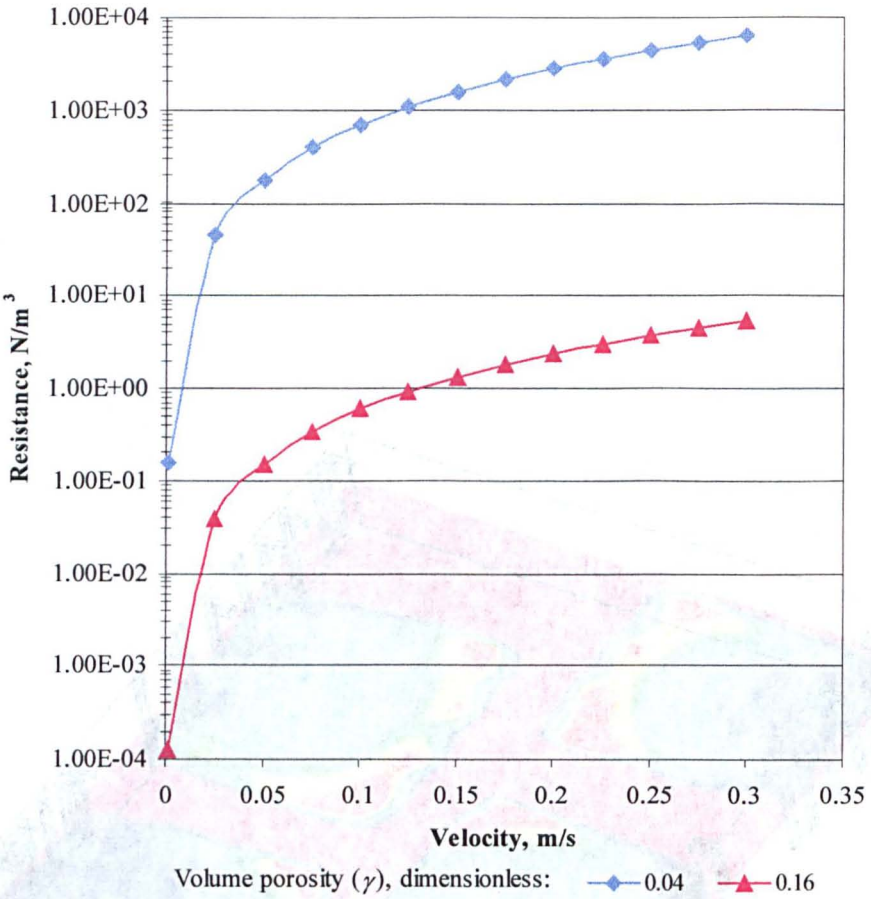

Figure 7.22. Effect of volume porosity on the calculation of flow resistance.

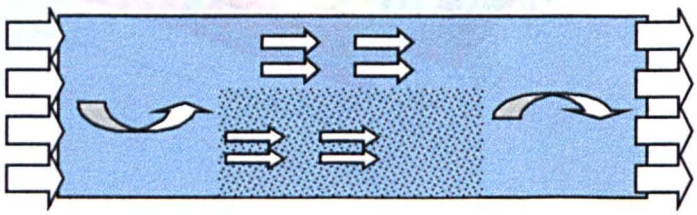

HIGH POROSITY FLOW

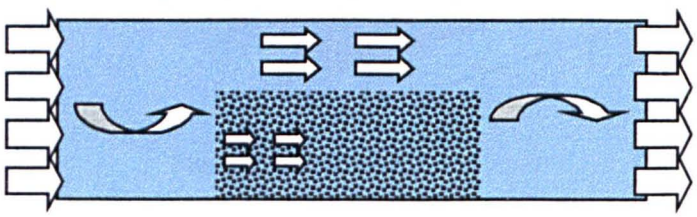

LOW POROSITY FLOW

Figure 7.23. Sketch to illustrate the effect the resistance on the flow.

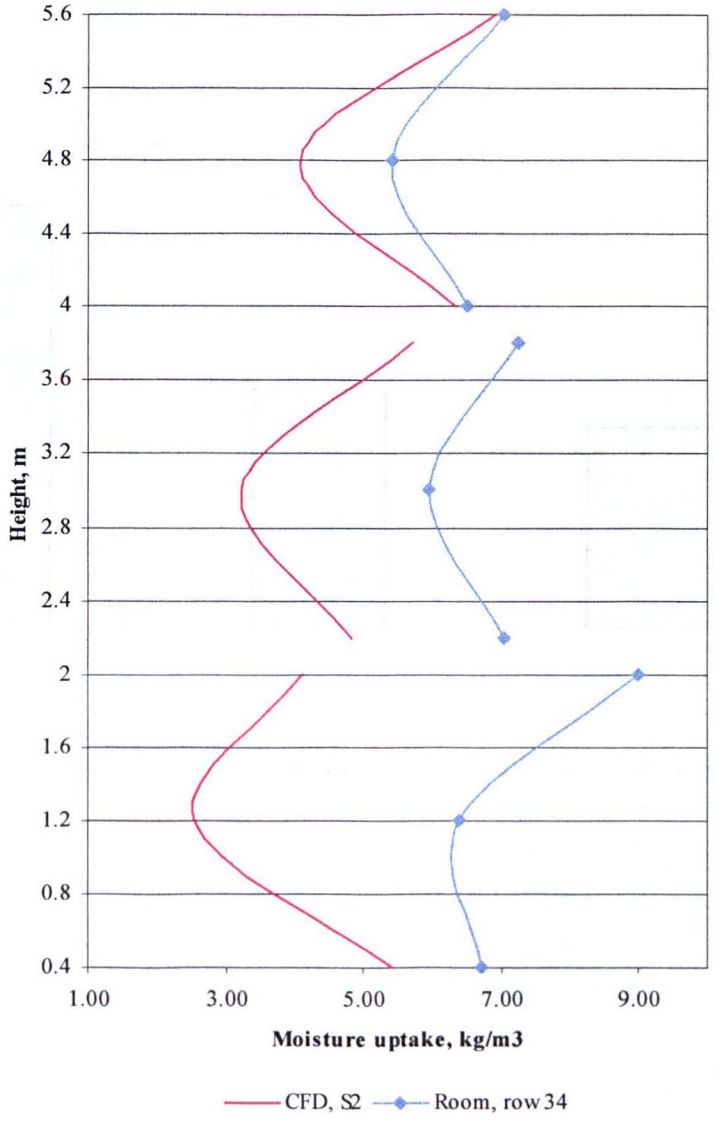

Figure 7.24. Comparison of moisture uptake profiles. Silicagel after 10 days. Approximate location: x = 28m, y = 20m.

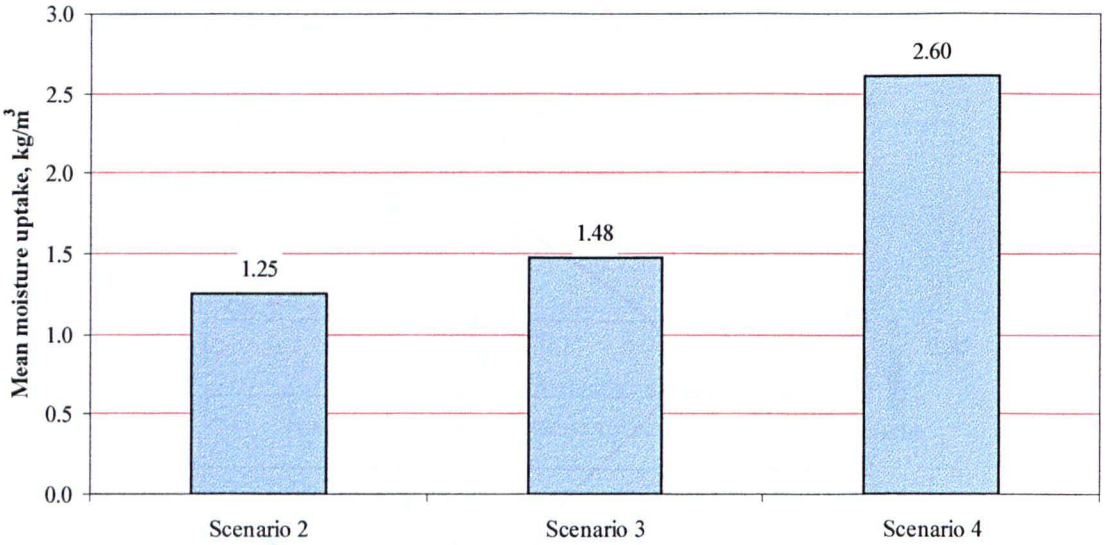

Figure 7.25. Comparison of bisquet mean moisture uptake after 10 days.

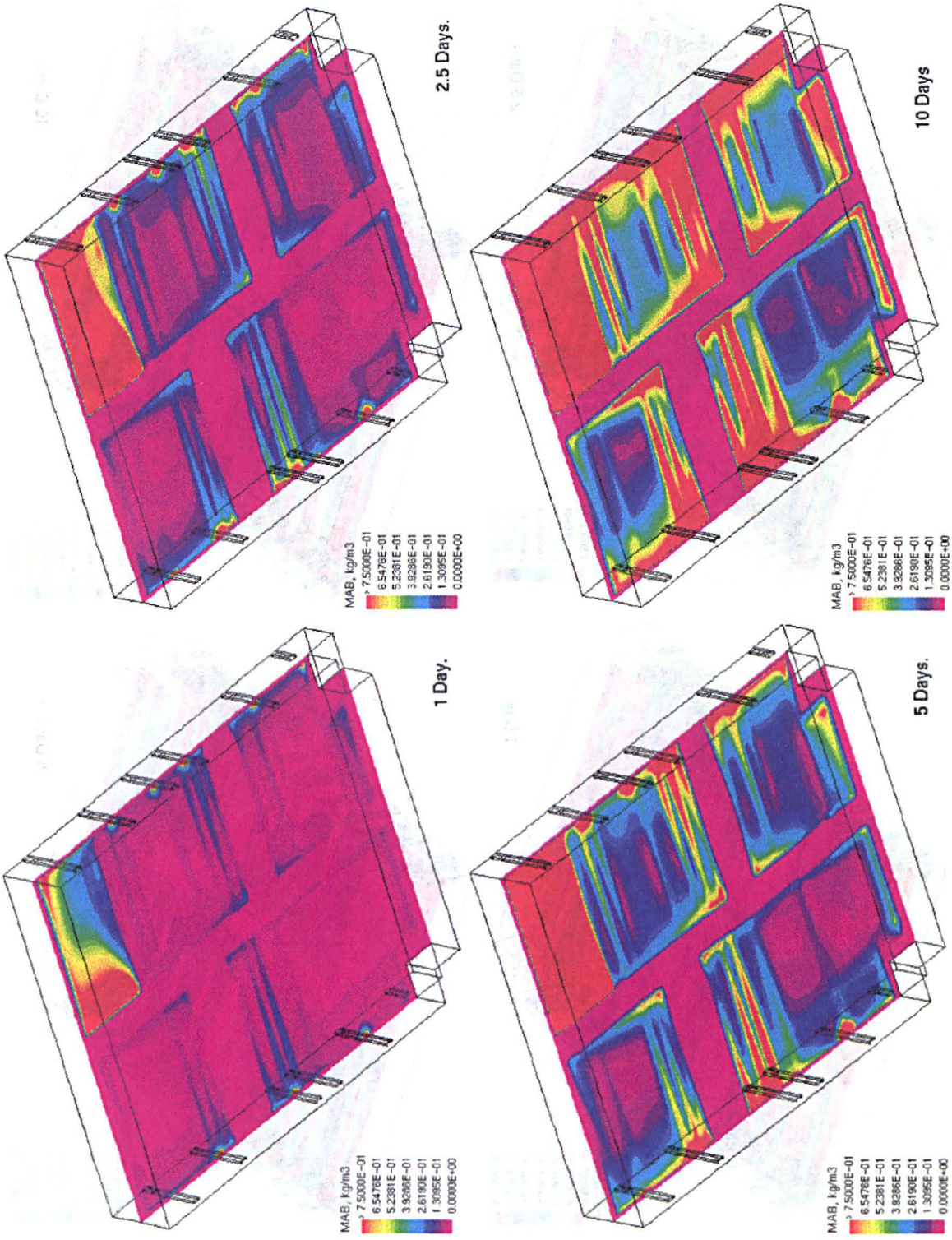

Figure 7.26. Scenario 2. Z = 3m.

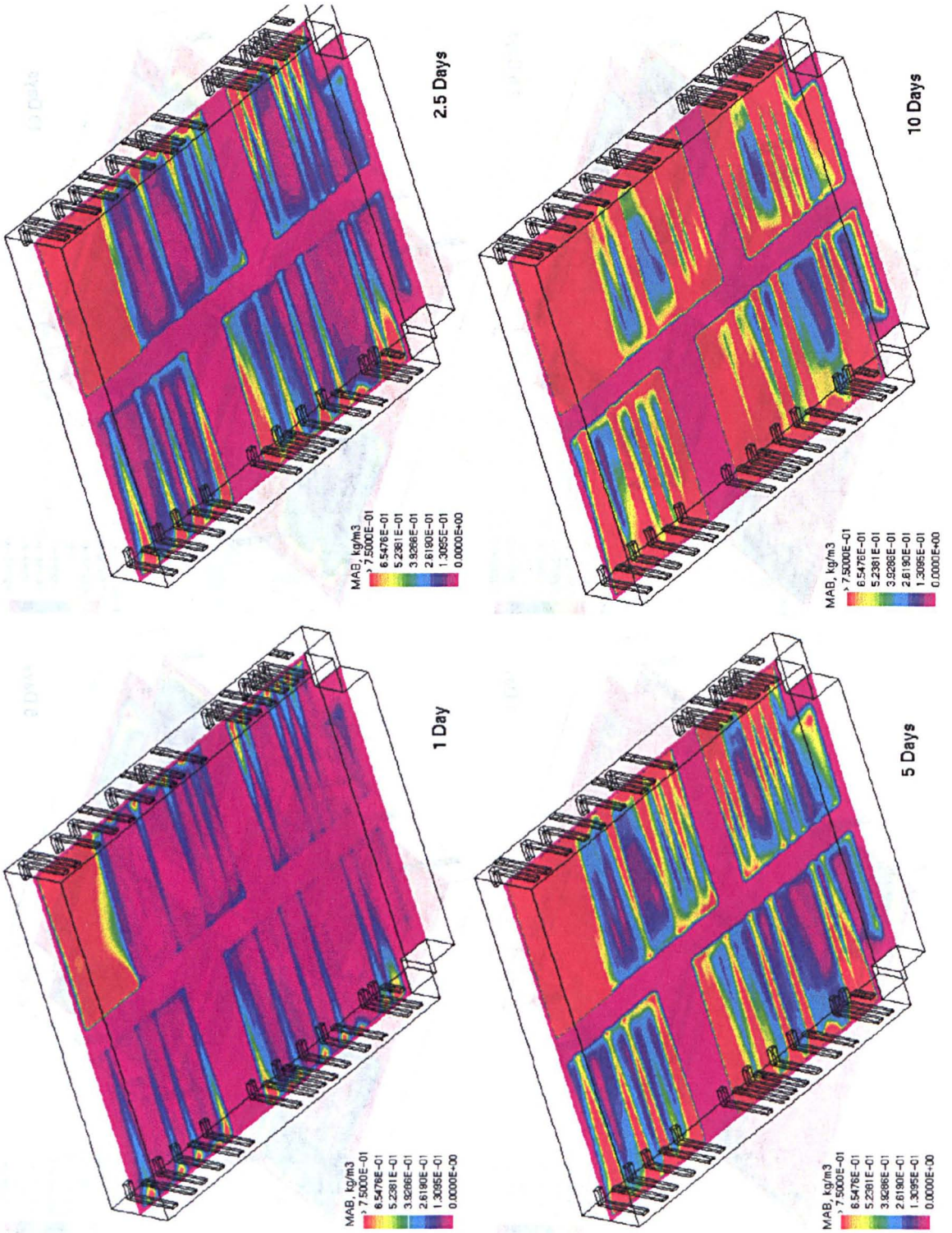

Figure 7.27. Scenario 3. Z = 3m.

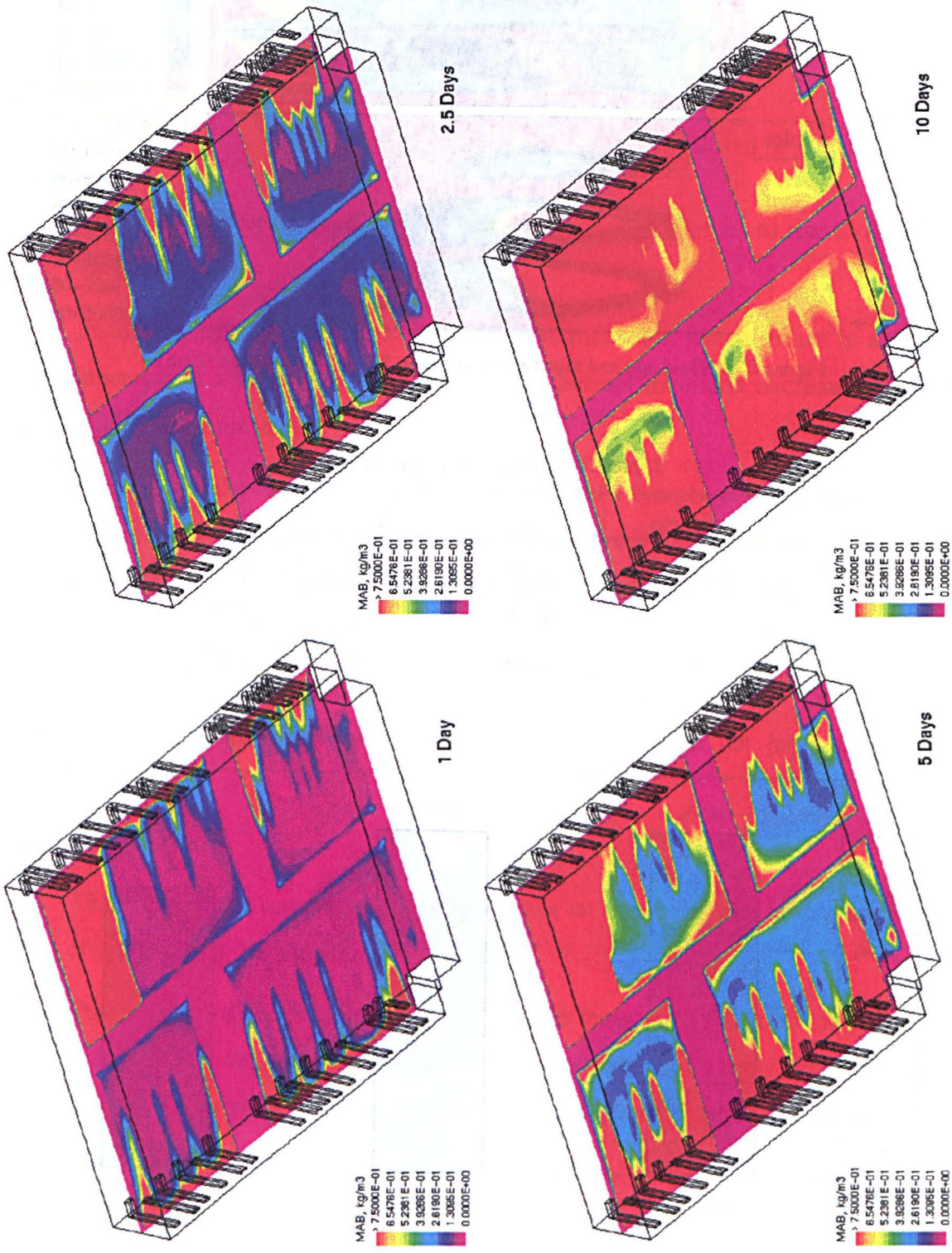

Figure 7.28. Scenario 4. Z = 3m.

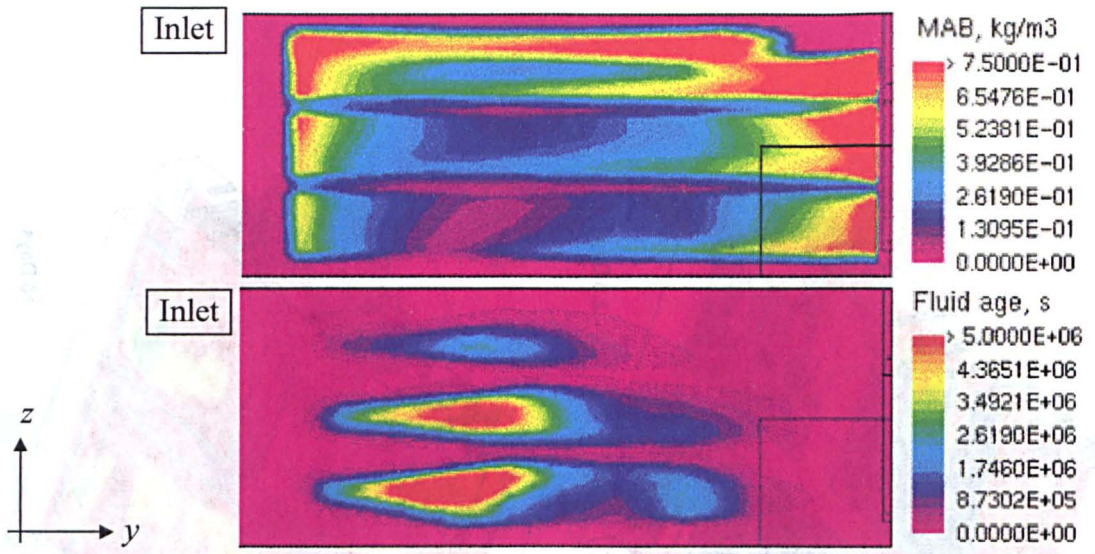

Figure 7.29. Fluid age and moisture absorption. Scenario 1 (plane x=24m).

Table 7.1. Statistical data after 10 days.

Scenario	*s*	a_3	a_4 -3
2	1.50	2.63	8.15
3	1.78	2.50	6.90
4	2.58	1.49	1.22

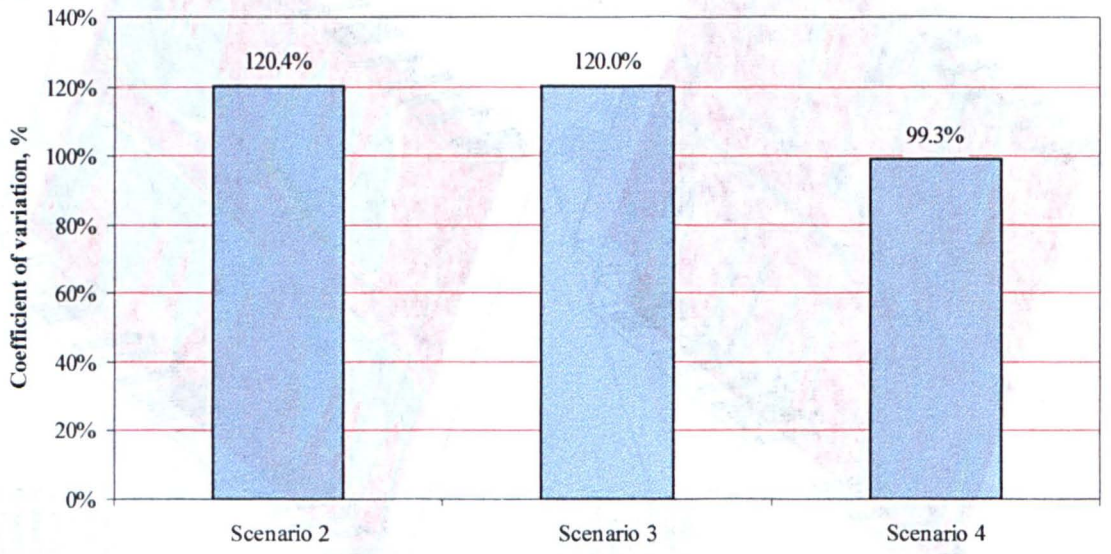

Figure 7.30. Comparison of wafer coefficient of variation after 10 days.

8 CONCLUSIONS

8.1 Buoyancy affected flow

From measurements in the hangar:

- Buoyancy forces are dominant and cause most of the hot air to rise to the top of the hangar.
- Inside the hangar there exists an unstable stratification which results in a thermal inversion at a height between 6-8m. This thermal inversion decreases when air mixing is increased.
- On average the measured temperature inside the hangar at working levels was within the range recommended by ISO Standard 7730. However, during some periods of time temperature values inside the hangar were below those recommended for thermal comfort.
- The jet penetration, under test conditions, was observed to be 19m when the doors are closed. However, when the doors are open the jet penetration is reduced.

From CFD analysis:

- The effect of the top gap in the hangar plays an important role in the distribution of air inside of the hangar.
- The use the 'tall boys' helps to obtain a better temperature distribution within the hangar. Also, the scenarios modelled with boundary conditions simulating open doors have shown a great level of exfiltration that reduces the performance of the heating system.

From the tank experiments:

The experiments in the tank helped to understand the dynamics of the flow inside of the hangar and helped to build confidence in the CFD results. The penetration of the

incoming light fluid is function of the Froude number. The algebraic relationship obtained in this work is:

$$\frac{Zpi}{r_o} = 3.4419 Fr^{1/2}$$

Also, the experiments showed an oscillating layer in the interface between the trapped light fluid and the stratified layer beneath it. The measured period of the oscillatory movement was similar to that calculated using the Brunt-Vaisala number.

8.2 Porosity affected flow

From measurements in the repository:

- The current distribution of inlet air is uneven.
- The temperature distribution at the centre of the room is uniform.

From cabinet experiments:

- Well-packed trays absorb more water than badly packed trays. The increment could be as much as 50%.
- Bad packaging has a similar effect on moisture absorption than reducing the ambient relative humidity.
- Increasing air velocity increases moisture uptake. Reducing air flow velocity by 80% reduces the moisture uptake approximately 75%.

From silicagel experiments in the repository:

- The distribution of moisture uptake in the vertical is not uniform.
- On average, trays placed in the bottom stack absorbed more moisture than those located in the middle and top of the stack.
- Silicagel bags placed in 2 Finger areas absorb more moisture than those in 4 finger areas.

From CFD analysis:

- Fluid age analysis has highlighted stagnant areas inside of the room.

- The installation of recirculation devices in the storeroom improves the fluid age distribution. The combined effect of recirculation units and well packaging techniques, (scenario 4) increases more than 87 times the performance of the current ventilation system (scenario 2).
- The absorption of moisture increases when recirculation units are used. When the effect of using well packed trays is added to that of the inclusion of recirculation units as in scenario 4, the mean moisture uptake increases 2 times with respect to scenario 2
- The introduction of recirculation devices increases the moisture uptake and improves its distribution. Further improvement is achieved when good packing techniques are used.
- The coefficient of variation of moisture absorption is reduced when the effect of using well packed trays is added to that of the inclusion of recirculation units as in scenario 4.

9 REFERENCES

1. AEA Technology plc. 1997. CFX-4.2: Solver manual.
2. Alamdari F. 1991. 'Thermo-fluid analysis in the built environment: expectations and limitations'. Computational fluid dynamics for the environmental and building services engineer - tool or toy? Mechanical Engineering Publications Limited for The Institution of Mechanical Engineers, 5-12.
3. Awbi H. B. and Gan G. 1991. 'Computational fluid dynamics in ventilation'. Computational fluid dynamics for the environmental and building services engineer - tool or toy? Mechanical Engineering Publications Limited for The Institution of Mechanical Engineers, 67-79.
4. Baines W. D., Turner J. S. and Campbell I. H. 1990. 'Turbulent fountains in an open chamber'. Journal of Fluid Mechanics. 255, 621-646.
5. Baines W. D., Corriveau A. F. and Reedman T. J. 1993. 'Turbulent fountains in an closed chamber'. Journal of Fluid Mechanics. 212, 557-592.
6. Bejan A. 1984. Convection Heat Transfer. John Wiley & Sons. USA.
7. Bergstrom D. J. 1994. 'Numerical prediction of a turbulent fountain in a room'. ASHRAE Transactions. Part 2, 669-672.
8. Chen C. and Jaw S. 1998. 'Fundamentals of turbulence modelling'. Taylor and Francis.
9. Chen Q. and Jiang Z. 1992. 'Significant questions in predicting room air motion'. ASHRAE Transactions 98(1), 929-939.
10. Cotel A. J., Gjestvang J. A., Ramkhelawan N. N. and Breidenthal R. E. 1997. 'Laboratory experiments of a jet impinging on a stratified interface'. Experiments in Fluids. 23, 155-160.
11. Crittenden B. and Thomas W. J. 1998. 'Adsorption technology and design'. Butterwoth-Heineman.
12. Davis J. C. 1973. 'Statistics and data analysis in Geology'. John Wiley & Sons.

13. Ferziger J. H. and Peric M. 1997. 'Computational methods for fluid dynamics'. Springer.

14. Gebhart B. 1973. 'Instability, transition, and turbulence in bouyancy-induced flows'. Annual Review of Fluid Mechanics. 5, 213-246.

15. Gebhart B, Hilder D. S. and Kelleher M. 1984. 'The diffusion of turbulent buoyant jets'. Advances in Heat Transfer. Academic Press Inc. (16) 1-57.

16. Gouvalias G., Markatos N. C., Panagopoulos J., Tierney M.J., Huberson S. and Zhong G. 1993. 'Advanced flow modelling for industrial applications – CFD models of adsorbers'. Energy Efficiency in Process Technology. Ed. Pilavachi P. A. Elsevier Applied Sciences.

17. Goldman D. and Jaluria Y. 1986. 'Effect of opposing buoyancy on the flow in free and wall jets'. Journal of Fluid Mechanics. 166, 41-56.

18. Hagmeijer R. and De Cock K.M.J. 1992. 'Grid adaptation for problems in computational fluid dynamics'. Computational Fluid Dynamics'92. Volume 2. Elsevier Science Publishers B.V.

19. Homan K. O. and Soo S. L. 1997. 'Model of the transient stratified flow into a chilled-water storage tank'. International Journal of Heat and Mass Transfer. 40(18), 4367-4377.

20. Jaluria Y. 1980. 'Natural convection. Heat and mass transfer. Pergamon Press.

21. Labuza T. P. and Hyman C. R. 1998. 'Moisture migration and control in multi-domain foods'. Trends in Food Science and Technology. 9, 47-55.

22. Larson M. and Jönsson L. 1994. 'Mixing in a two-layer stably stratified fluid by a turbulent jet'. Journal of Hydraulic Engineering. 32(2), 271-289.

23. Larson M. and Jönsson L. 1995. 'Modelling of mixing by turbulent jet in stably stratified fluid'. Journal of Hydraulic Engineering. 121(12), 853-862.

24. Launder B. E. 1984. 'Numerical computation of convective heat transfer in complex turbulent flows: time to abandon wall functions? International Journal of Heat and Mass Transfer. 27(9), 1485-1491.

25. Launder B. E. and Spalding D. B. 1974. 'The numerical computation of turbulent flows'. Computer Methods in Applied Mechanics and Engineering. 3, 269-289.

26. Lee S and Chen C. 1996. 'Finite element solution of laminar and turbulent mixed convection in a driven cavity'. International Journal for Numerical Methods in Fluids. 23, 47-46.

27. Lesier M. 1997. 'Turbulence in fluids'. Kluwer Academic Publisher.

28. Levenspiel O. 1972. 'Chemical reaction engineering'. John Wiley & Sons.

29. Li W. and Huai W. 1995. 'Calculation of the whole field for vertical round buoyant jets in static linearly stratified environment'. Journal of Hydraulic Research. 33(6), 865-876.

30. List E. J. 1982. 'Turbulent jets and plumes'. Annual Review of Fluid Mechanics. 14, 189-212.

31. Machado M. F., Oliveira F. A. R., Gekas V. and Singh R. P. 1998. 'Kinetics of moisture uptake and soluble-solids loss by puffed breakfast cereals immersed in water'. International Journal of Food Science and Technology. 33, 225-237.

32. Masters G. M. 1998. 'Introduction to environmental engineering and science'. Prentice-Hall International Inc.

33. Mensink C. and Deconinck. 1992. 'A 2D parallel multiblock Navier-Stokes solver with applications on shared- and distributed memory machines'. Computational Fluid Dynamics'92. Volume 2. Elsevier Science Publishers B.V.

34. Morton B. R. 1959. 'Forced plumes'. Journal of Fluid Mechanics. 5, 151-163.

35. Murakami S. 1992. 'New scales for ventilation efficiency and their application based on numerical simulation of room airflow'. 1992 International Symposium on room air convection and ventilation effectiveness. Published by ASHRAE. 29-49.

36. Ogino F., Takeuchi H., Kudo I. and Mizushina T. 1980. 'Heated jet discharged vertically into ambients of uniform and linear temperature profiles'. International Journal of Heat and Mass Transfer. 23, 1581-1588.

37. Patankar S.V. and Spalding D.B. 1972. 'A calculation procedure for heat, mass and momentum transfer in three-dimensional parabolic flows'. International Journal of Heat and Mass Transfer. (15), 1787-1806.

38. Péniguel C. 1998. 'Heat transfer simulation for industrial applications: needs, limitations, expectations'. International Journal of Heat and Fluid Flow. 19, 102-114.

39. Popiel C. O. and Wojtkowiak J. 1998. 'Simple formulas for thermophysical properties of liquid water for heat transfer calculations (from 0°C to 150°C)'. Heat Transfer Engineering. 3 (19), 87-101.

40. Sandberg M. and Sjöberg. 1983. 'The use of moments for assessing air quality in ventilated rooms'. Building and Environment. 18 (4), 181-187.

41. Scorer R. S. 1997. 'Dynamics of meteorology and climate'. John Wiley & Sons.

42. Scott G. and Richardson P. 1997. 'The application of computational fluid dynamics in the food industry'. Trends in Food Science and Technology. 18, 119-124.

43. Seban R. A., Behnia M. M. and Abreu K. E. 1978. 'Temperatures in a heated air jet discharged downward'. International Journal of Heat and Mass Transfer. 21, 1453-1458.

44. Somasundaram S., Anand N. K., Suh Y. B. and Aung W. 1989. 'Analysis of moisture migration in two-dimensional unsaturated porous media with impermeable boundaries'. International Journal of Heat and Mass Transfer. 9 (32), 1733-1739.

45. Sommer T. P., So R. M. C. and Zhang J. 1997. 'Modelling nonequilibrium and history effects of homogeneous turbulence in a stably stratified medium'. International Journal of Heat and Fluid Flow. 18(1), 29-37.

46. Spiegel M. R. 1992. 'Schaum's Outline of Theory and Problem of statistics'. McGraw-Hill Book Company.

47. Stefan H. G. and Gu R. 1992. 'Efficiency of jet-mixing of temperature-stratified water'. Journal of Environmental Engineering. 118(3), 363-379.

48. Tennekes H. and Lumley J. L. 1972. 'A first course in turbulence'. The Massachusetts Institute of Technology.

49. Tierney M., Nasr A. and Quarini G. 1998. 'The use of proprietary computational fluid dynamics codes for flows in annular packed beds'. Separation and Purification Technology. 13, 97-107.

50. Turner J.S. 1966. 'Jets and plumes with negative or reversing buoyancy'. Journal of Fluid Mechanics. 26(4), 779-792.

51. Turner J.S. 1973. 'Bouyancy effects in fluids'. Cambridge University Press.

52. Turner J.S. 1986. 'Turbulent entrainment: the development of the entrainment assumption, and its application to geophysical flows'. Journal of Fluid Mechanics. (173), 431-471.

53. Versteeg H. K. and Malalasekera W. 1995. 'An introduction to computational fluid dynamics. The finite volume method'. Longman Scientific and Technical.

54. Vilsmeier R. and Hänel. 1992. 'Adaptative solutions for compresible flows on unstructured, strongly anisotropic grids'. Computational Fluid Dynamics'92. Volume 2. Elsevier Science Publishers B.V.

55. Whitaker S. 1977. 'Simultaneous heat, mass, and momentum transfer in porous media: a theory of drying'. Advances in Heat Transfer. (13), 119-203.

56. Whitaker S. 1998. 'Coupled transport in multiphase systems: a theory of drying'. Advances in Heat Transfer. (31), 1-104.

57. Xu Y. and Burfoot D. 1999a. 'Simulating the bulk storage of foodstuff'. Journal of Food Engineering. 39(1), 23-29.

58. Xu Y. and Burfoot D. 1999b. 'Predicting condensation in bulks of foodstuff'. Journal of Food Engineering. 40(1), 121-127.

59. Yuan X., Moser A., and Suter P. 1993. 'Wall functions for numerical simulation of turbulent natural convection along vertical plates'. International Journal of Heat and Mass Transfer. 36(18), 4477-4485.

60. Zhang H. and Baddour R. E. 1997. 'Maximum vertical penetration of plane turbulent negatively buoyant jets'. Journal of Engineering Mechanics. 123(10), 973-977.

61. Zhang H. and Baddour R. E. 1998. 'Maximum penetration of vertical round dense jets at small and large Froude numbers'. Journal of Engineering Mechanics. 123(10), 973-977.